ABSTRACT

Title of Dissertation: LONGITUDINAL DYE DISPERSION AND SALT FLUX IN ESTUARIES

Wei Liu, Doctor of Philosophy, 2017

Dissertation directed by: Professor Ming Li
Horn Point Laboratory, UMCES
Marine Estuarine Environmental Science

Estuarine dispersion plays an important role in determining the fate of waterborne materials. It is a long-standing question in estuarine dynamics that is still not well understood. This dissertation revisits this problem by utilizing two tracers: dye and salt.

Dye-release experiments and numerical modeling are conducted to investigate horizontal dispersion in a partially mixed estuary. Longitudinal dispersion of a dye patch shows strong flood-ebb asymmetry at early times after a dye release, with most of the dispersion occurring during ebb tides. Tidal straining enhances vertical current shear on ebb tides and promotes longitudinal dispersion. There are also large differences in the dispersion rate between spring and neap tides. Due to strong spring mixing, a dye patch quickly extends from the bottom to the surface, exposing to the full vertical shear in the water column and leading to strong longitudinal dispersion. In contrast most of the dye patch is limited to bottom few meters during neap tides. Although weak vertical mixing facilitates longitudinal dispersion, the vertical shear across the thin dye patch is much

weaker, leading to weak longitudinal dispersion during neap tides. In first four tidal cycles, the second moment of the dye patch in the along-channel direction increases with time at a power of between 2 and 3. The longitudinal dispersion rate varies as the four-third power of the dye patch size, indicating scale-dependent diffusion.

Salt dispersion and transport are examined in a comparative numerical modeling study between the partially-mixed Chesapeake Bay and the well-mixed Delaware Bay. To investigate how different physical mechanisms drive the salt transport into the estuaries, the longitudinal salt fluxes are decomposed using the Eulerian and quasi-Lagrangian methods. Under the Eulerian framework, the salt flux is decomposed into three parts: an advective term associated with the barotropic forcing, a steady shear dispersion term associated with the estuarine exchange flow, and a tidal oscillatory salt flux. In both estuaries, the advective term is dominant over steady shear dispersion and tidal oscillatory salt flux in the temporal variation of total salt flux. In Chesapeake Bay, the steady shear dispersion is the dominant mechanism and the tidal oscillatory salt fluxis small. In Delaware Bay, the steady shear dispersion and tidal dispersion are comparable. The along-channel variation of tidal oscillatory salt flux is mainly due to changes of the phase difference between the tidal current and salinity. Isohaline analysis using the quasi-Lagrangian methodology yields a new interpretation of the estuarine exchange flows and describes the evolution path of salinity classes.

LONGITUDINAL DYE DISPERSION AND SALT FLUX IN ESTUARIES

By

Wei Liu

Dissertation submitted to the Faculty of the Graduate School of the
University of Maryland, College Park, in partial fulfillment
of the requirements for the degree of
Doctor of Philosophy
2017

Advisory Committee:

Professor Ming Li, Chair
Emeritus Professor William Boicourt
Associate Professor Elizabeth North
Assistant Professor James Pierson
Professor Lawrence Sanford

ACKNOWLEDGEMENTS

I would like to thank my advisor, Dr. Ming Li, for all his support through my graduate years. He has provided numerous advice and help when I had difficulties during my study. His excellent knowledge in physics enables me to learn, grow and conduct my present research. He is always guiding me to move forward as best I can, which is a valuable training experience that is beneficial for my future work. In addition, he provided long-term financial support and computational resources which were essential to my graduate research.

I also would like to thank my wonderful committee members, Drs. William Boicourt, Elizabeth North, James Pierson and Lawrence Sanford, for providing insightful advice, and for their encouragement and support through many years. I deeply appreciate Dr. William Boicourt's numerous talks with me and his brilliant suggestions. I am grateful for HPL Education Committee for providing me financial support. I also would like to thank Dr. Kayo Ide for her willingness to serve as Dean's Representative for my defense.

I thank Xiaohui Xie, Fan Zhang, Andrew Ross, and Wenfei Ni in Dr. Ming Li's research group for various helpful discussions. Alexander Fisher, Katherine Liu, Yini Shangguan and Jacqueline Tay have assisted me in many aspects of my life. I am thankful to all the HPLers I have met here, who make my experience very memorable.

Last, but not least, I would like to thank my family and my fiancé Yin Yuan for their love and ful support throughout my time in graduate school. Without their support, I could never have gone so far.

TABLE OF CONTENTS

ACKNOWLEDGEMENTS II
LIST OF TABLES V
LIST OF FIGURES VI
CHAPTER 1. INTRODUCTION 1
§1.1 Estuarine Dispersion Overview 2
§1.2 Tidal and Subtidal Variation of Estuarine Dispersion 4
§1.3 Estuarine Dispersion of Salt 6
§1.4 Objectives 10
CHAPTER 2. TIME AND SCALE DEPENDENCE IN ESTUARINE LONGITUDINAL DISPERSION 11
§2.1 Introduction 12
§2.2 Field observations 16
2.2.1 Field experiments 16
2.2.2 Observed dye dispersion 21
§2.3 Numerical modeling 28
2.3.1 Model configuration and validation 29
2.3.2 Dye dispersion during spring tide 32
2.3.3 Dye dispersion during neap tide 38
§2.4 Discussion 42
2.4.1 Flood-ebb and spring-neap variations in the longitudinal dispersion 42
2.4.2 Scale-dependent dispersion at large times 45
§2.5 Conclusion 48
CHAPTER 3. COMPARATIVE STUDY OF SALT FLUXES IN PARTIALLY MIXED AND WELL MIXED ESTUARIES 50
§3.1 Introduction 52
§3.2 Methods 59
3.2.1 Development of FVCOM model for Chesapeake and Delaware Bays 61
3.2.2 Eulerian Decomposition of Salt Fluxes 67
3.2.3 Isohaline Decomposition of Salt Fluxes 69
§3.3 Results 71
3.3.1 Neap-spring variation of subtidal velocity and salinity field 71
3.3.2 Salt budget and salt balance 77
3.3.3 Temporal variation of Salt Flux Components: F0, Fe and Ft 79
3.3.4 Along-channel Variation of Salt Flux Components: Fe and Ft 84

§3.4 Discussion 86
3.4.1 What is controlling in the fluctuation of F0? 86
3.4.2 What factor is controlling the along-channel variation of Ft? 87
3.4.3 Isohaline Decomposition of Salt Fluxes 93
§3.5 Conclusions 102
CHAPTER 4 CONCLUSIONS 106
§4.1 Research Conclusions 107
§4.2 Research Applications 109
APPENDIX A 112
BIBLIOGRAPHY 123

LIST OF TABLES

Chapter 3

Table 3.1 Comparison of physical properties of Chesapeake Bay and Delaware Bay.

LIST OF FIGURES

Chapter 2

Figure 2.1 (a) Map of Chesapeake Bay and its southernmost tributary – the James River (marked by the red rectangle). Chesapeake Bay Program Station 7.3 is marked with blue rhombus. The yellow rectangle shows the location of weather station at Swells Point, VA (SWPV2). (b) Zoomed-in view of the James River section where dye injection experiments were conducted. The contours show the bathymetry while the red star indicates the approximate observed dye injection location. The red dots specify the location of 10 mooring stations including the central mooring station L2C. The yellow rectangle shows the location of weather station DOMV2.

Figure 2.2 Time series of (a) river discharge at USGS station at Richmond, Virginia, (b) wind speed vector from the National Data Buoy Center station DOMV2, (c) observed tidal sea level at Swells Point, Hampton Roads, and (c) stratification at the central mooring station L2C. N marks the neap tide and S marks the spring tide.

Figure 2.3 Plane view of the vertically integrated dye patch concentration (color, 10^{-5} kg/m^2) at (a) 3.6, (b) 4.6, (c) 7.3, (d) 9.4 hours after the dye release on May 27. The black dashed lines show bathymetry contours in meters. The dotted green and blue lines mark the cross-channel transects taken to sample the dye patch.

Figure 2.4 Along-channel distribution of dye concentration (color, 10^{-8} kg/m^3) and salinity (contour, psu) at (a) 3.9, (b) 4.5, (c) 8.3, (d) 9.7 hours after the May 27 release.

Figure 2.5 Cross channel distribution of dye concentration (color, 10^{-6} kg/m^2) and salinity (contour, psu) at (a) 3.4, (b) 4.6, (c) 7.9 and (d) 9.1 hours after May 27 release. The transect locations are marked as dotted blue lines in Figure 2.3.

Figure 2.6 Gaussian Fitting to along-channel distribution of sectionally averaged dye concentration at (a) 3.9, (b) 4.5, (c) 8.3, (d) 9.7 hours after May 27 release. The blue dots mark the observed dye concentration and red lines are the fitted Gaussian curves.

Figure 2.7 Time series of σ_x^2 calculated from the observed (dots) and the predicted (lines) dye distribution for the four dye experiments: (a) May 5, (b) May 7, (c) May 25 and (d) May 27.

Figure 2.8 ROMS grid and bathymetry of the James River Estuary with the approximate dye injection location marked by red star. Grid points are plotted at every three other points.

Figure 2.9 Plan view of the model-predicted vertically integrated dye concentration at 3, 9, 15, 21, 36 and 48 hours following the dye-release on May 27. Blue dots represent the cross-channel locations in Figure 2.11.

Figure 2.10 Along-channel distributions of along-channel velocity (left column), salinity (contours) and dye concentration (color, 10^{-8} kg/m^2) (middle column) and vertical diffusivity (m^2/s) (right column) at 3, 9, 15, 21, 36 and 48 hours after May 27 release.

Figure 2.11 Cross-channel distributions of lateral velocity (left column), salinity (contours) and dye concentration (color) (middle column) and along-channel velocity (right column) at 3, 9, 15, 21, 36 and 48 hours after May 27 release.

Figure 2.12 Plan view of the model-predicted vertically integrated dye concentration at 6, 12, 18, 24, 36 and 48 hours following the dye release on May 5. Blue dots represent the cross-channel locations in Figure 2.14.

Figure 2.13 Along-channel sections of along-channel velocity, dye patches concentration and vertical diffusivity at 6 (flood), 12 (ebb), 18 (flood), 24 (ebb), 36, and 48 hours after May 5 release. Concentration is in unites of 10^{-8} kg/m^2; vertical diffusivity is plotted using a log-10 scale.

Figure 2.14 Cross-channel sections of cross-channel velocity (a-f), dye patches concentration (g-l) and along-channel velocity (m-f) at 6 (flood), 12 (ebb), 18 (flood), 24 (ebb), 36, and 48 hours after May 5 release.

Figure 2.15 Time series of σ_x^2 in the first 24 hours after the dye release: (a) May 5 and (b) May 27. σ_x^2 increases with time rapidly during ebb tide but shows slow increases or contraction during the flood tide. The numbers are the estimated longitudinal diffusivity for the flood and ebb periods.

Figure 2.16 σ_x^2 versus time during four releases: (a) linear scale; (b) log scale. The grey dashed lines indicate the slope of 1, 2.34 and 3, respectively.

Figure 2.17 Longitudinal diffusivity versus the length scale for four dye experiments. The dashed magenta lines indicate the slope of 4/3.

Chapter 3

Figure 3.1 Bathymetry of Chesapeake Bay, Delaware Bay and their adjacent coastal area. Depths are in meters. Black dots are the locations of CBP stations and Delaware Bay survey sites. DB1 represent the upper bay station, DB2 mid-bay station and DB3 lower bay station.

Figure 3.2 FVCOM Model domain and grids.

Figure 3.3 Time series of observed (red) and modeled (blue) sea level at tidal gauge station Baltimore (a), Soloman Island (b), CBBT (c) in Chesapeake Bay and Lowes (d), and Reedy Point (e) in Delaware Bay.

Figure 3.4 Comparisons of surface and bottom salinity in three Chesapeake Bay Program (CBP) stations CB2.2 , CB5.5 and CB7.4 located at upper (a, b), middle (c, d) and lower (e, f) bay (See Fig. 3.1). Red dots represents observation data and blue line represents the model data.

Figure 3.5 Observation-model comparison of surface salinity in upper (a), middle (b) and lower Delaware Bay. Red dots represent observation data and blue lines represent the model data.

Figure 3.6 Along-channel sections of subtidal along-channel velocity during neap tide (a) and spring tide (b) in Chesapeake Bay in December, 2011. Low-pass filtered velocity is shown.

Figure 3.7 Along-channel sections of averaged salinity field during neap (a) and spring (b) tide in Chesapeake Bay in December, 2011.

Figure 3.8 Cross-channel section of averaged salinity field during neap (a) and spring (b) tide in lower-Chesapeake Bay (Facing into the estuary) in December, 2011.

Figure 3.9 Along-channel sections of the subtidal velocity in Delaware Bay during the neap (a) and spring (b) tides in December, 2011. Low-pass filtered velocity is shown.

Figure 3.10 Along-channel sections of averaged salinity field during neap tide (a) and spring tide (b) in Delaware Bay in December, 2011.

Figure 3.11 Cross-channel sections of salinity field during neap (a) and spring (b) tide in lower Delaware Bay in December, 2011.

Figure 3.12 Time series of Susquehanna River discharge (a), salt content (blue line in b) and integrated salt flux (red line in b), and monthly salt flux (c) in Chesapeake Bay, and Delaware River discharge (d), salt content (blue line in e), and integrated salt flux (red line in e), and monthly salt flux (f) in Delaware Bay.

Figure 3.13 Averaged monthly salt flux decomposition components at 80 cross-sections in Chesapeake Bay (a) and Delaware Bay (b). Shear dispersion due to baroclinic exchange flow Fe is shown with blue bar, tidal oscillatory salt flux is marked by red bar, and the advective salt flux F0 black bar.

Figure 3.14 Times series of salt flux decomposition components at mid-bay section in Chesapeake Bay (a) and Delaware Bay (b): Shear dispersion due to baroclinic exchange flow Fe (blue), tidal pumping Ft (red), and subtidal barotropic transport F0 (black).

Figure 3.15 Along-channel distribution of lateral-integrated steady shear dispersion Fe and tidal oscillatory salt flux Ft and dispersive fraction of upstream salt fluxes

(Ft/(Fe+Ft)), along the Chesapeake Bay (a, b) and Delaware Bay (c, d) estuary. Data plotted has been averaged in 2011.

Figure 3.16 Time series of subtidal sea level difference across the near-mouth section (a) and F0 (b) in Chesapeake Bay.

Figure 3.17 Phase difference between tidal current and tidal salinity variation in Chesapeake Bay (a) and Delaware Bay (b).

Figure 3.18 Three scenarios of phase difference (smaller than, equal to or larger than 90 degrees) and correlated Ft sign (Wang et al., 2015).

Figure 3.19 Along-channel distribution of (a) Ft, (b) amplitude of tidal current Ut, (c) tidal salinity oscillation St and (d) phase difference between Ut and St in Chesapeake Bay.

Figure 3.20 Along-channel distribution of (a) Ft, (b) amplitude of tidal current Ut, (c) tidal salinity oscillation St and (d) phase difference between Ut and St in Delaware Bay.

Figure 3.21 The differential isohaline transport function $\partial Q/\partial s$ vs salinity, at the Chesapeake Bay (a) and Delaware Bay (b) sections closest to the mouth, averaged over a year.

Figure 3.22 Contour plot of the isohaline transport function Q(x, s) in Chesapeake Bay (a) and Delaware Bay (b), averaged over a year.

Figure 3.23 TEF salinity (red) in Chesapeake Bay (a) and Delaware Bay (b) vs along-channel distance, averaged over a year. For comparison, the same properties calculated from the Eulerian-averaged properties are plotted in blue.

Figure 3.24 Along-channel distribution of TEF transport (red) in Chesapeake Bay (a) and Delaware Bay (b) and the TEF salt flux (red) in Chesapeake Bay (c) and Delaware Bay (d), averaged over a year. For comparison, the same properties calculated from the Eulerian-averaged properties are plotted in blue lines.

Appendix A

Figure A1. Plan view of the vertically integrated dye patch concentration (color) at (a) 3.8, (b) 4.5, (c) 7.3, (d) 9.1 hours after the dye release on May 5. The dashed lines show the bathymetry in meters. The dotted green and blue lines mark the cross-channel transects taken to sample the dye patch. The dotted blue lines mark the cross-channel transects plotted later.

Figure A2. Along-channel distributions of dye concentration (color, 10^{-8} kg/m^3) and salinity (contour, psu) at (a) 3.9, (b) 4.5, (c) 8.3, (d) 9.2 hours after May 5 release. X-axis is the along-channel distance from estuarine mouth.

Figure A3. Cross channel distributions of dye concentration (color, 10^{-8} kg/m3) and salinity (contour, psu) at (a) 3.1, (b) 4.6, (c) 7.0 and (d) 8.5 hours after May 5 release. The transect locations are marked as dotted blue lines in plan-view figures.

Figure A4. Plan view of the vertically integrated dye patch concentration (color) at (a) 2.78, (b) 5.15, (c) 8.11, (d) 9.65 hours after the dye release on May 7. The dashed lines show the bathymetry in meters. The dotted green and blue lines

mark the cross-channel transects taken to sample the dye patch. The dotted blue lines mark the cross-channel transects plotted later.

Figure A5. Along-channel distributions of dye concentration (color, 10^{-8} kg/m^3) and salinity (contour, psu) at (a) 2.8, (b) 5.2, (c) 8.1, (d) 9.7 hours after May 7 release. X-axis is the along-channel distance from estuarine mouth.

Figure A6. Cross channel distributions of dye concentration (color, 10^{-8} kg/m^3) and salinity (contour, psu) (a) 2.9, (b) 5.3, (c) 8.2, (d) 9.8 hours after May 7 release. The transect locations are marked as dotted blue lines in plan-view figures.

Figure A7. Plan view of the vertically integrated dye patch concentration (color) at (a) 2.8, (b) 4, (c) 6, (d) 9.6 hours after the dye release on May 25. The dashed lines show the bathymetry in meters; the dotted green and blue lines mark the cross-channel transects taken to sample the dye patch. The dotted blue lines mark the cross-channel transects plotted later.

Figure A8. Along-channel distributions of dye concentration (color, 10^{-8} kg/m^3) and salinity (contour, psu) at (a) 2.83, (b) 3.95, (c) 6.05, (d) 9.61 hours after May 25 release. X-axis is the along-channel distance from estuarine mouth.

Figure A9. Cross channel distributions of dye concentration (color, 10^{-8} kg/m^3) and salinity (contour, psu) (a) 2.7, (b) 3.8, (c) 6, (d) 9.5 hours after May 25 release. The transect locations are marked as dotted blue lines in plan-view figures.

CHAPTER 1. INTRODUCTION

Chapter 1 has four sections. Section 1 introduces the topic of estuarine dispersion and its broad impact; Section 2 discusses the temporal variation of dispersion and associated open questions; Section 3 focuses on the dispersion of salt in different estuaries; Section 4 describes the research objectives of this thesis.

§1.1 Estuarine Dispersion Overview

Estuarine dispersion is the process of distributing scalars over a wider area in the estuaries. It usually spreads masses with their concentration dropping. Estuarine dispersion can be induced by turbulence and differential advection. Molecular movement can induce dispersion as well but is neglectable in estuaries. Estuaries are the transitional area of brackish water that connects the fresh water from its upper reach with the ocean water at the mouth. They lie in a complicated dynamical environment where tides, freshwater inputs and wind are continually influencing the brackish water behavior inside. These processes enable the estuaries to disperse various types of waterborne biogeochemical resources such as nutritional elements, plankton and marine life larvae (Fortier and Leggett, 1982; Cruzado et al., 2002; Roman and Boicourt, 1999). Predicting the dispersal of substances in the estuaries requires a better understanding of the dispersion processes (Fischer et al., 1979). Estuaries are also under the potential contamination by human activities such as the disposal of sewage and industrial waste (Goldberg et al. 1978; Kadirvelu et al. 2001).

A quantitative understanding of the estuarine dispersion has the broad impact and application value for the study of marine biology and chemistry and also the protection of

the coastal environment. For example, estuarine dispersion is important for larval transport. Shen et al. (1999) found that both horizontal and vertical dispersion associated with tidal fronts are important mechanisms for the retention of larval organisms in the James River. A more accurate prediction of the dispersal of fish larvae in esturies may be built on the basis of better estimate of dynamcial environment where dispersion plays a fundamantal role (Fortier and Leggett, 1982). Review article by Levin (2006) also recognizes the importance of physical modeling of dispersion processes on understanding larval dispersal. The dispersion of salt can be quantatively examined by calculating the salt flux across one section. This topic is of particular interst because the distribution of salt not only directly influences the hydrodynamics but also is essential for the fate of salinity-sensitive species.

By conducting the dispersion study in this thesis, we hope to provide a solid physics foundation to address questions such as how the vertical positions of biological or chemical materials will affect their dispersal speed and how their dispersion varies under different tidal conditions.

Estuarine dispersion happens in three dimensions: the along-channel, the vertical and the lateral direction. The longitudinal dispersion is usually most significant not only because of the relatively long geographical range but also because the driving forces such as river discharge and tides are more directly posing their impacts in this direction. Thus we focus on the longitudinal dispersion in this dissertation.

In order to study the dispersion process, we need to find the representative substances in the estuary and trace their movement. There are two kinds of tracers: active and passive. Active tracers dynamically alter the flow of the fluid by changing fluid properties which appear in the equation of motion such as density or salinity, while passive tracers have no influence on flow. Many studies have successfully used the passive tracers such as dye to detect flow patterns in the estuaries (Ledwell et al., 1998; Chen et al. 2008; Geyer et al., 2008). Salt, as an active tracer, is also a most common substance to characterize the dispersion processes for the entire estuary with brackish water. The dispersion of salt itself is a long-standing question in estuarine dynamics that has not been fully answered. In this dissertation, we utilize both dye and salt as the tracking elements in order to gain new insight about the estuarine dispersion.

§1.2 Tidal and Subtidal Variation of Estuarine Dispersion

Dispersion of waterborne materials in estuaries is a long-existing but poorly-understood topic in estuarine physics. The dispersion processes have a major impact on the biological, chemical and physical aspects of the estuarine environment. Better understanding of waterborne material dispersion is also of great importance in practical cases such as predicting contaminant transport and fish larval dispersal (Levin, 2006). The most obvious dispersion happens in the along-channel direction: the river discharge at the upstream end and tides at the downstream end are the major external forcing. Gravitational circulation and tidal shears have direct influence on the longitudinal dispersion.

In natural stream, the molecular dispersion is trivial compared with the dispersion induced by other processes and thus can be neglected. The most effective longitudinal dispersion is mainly driven by shears. These shears could be categorized by their directions: the vertical shear represents the vertical variation of along-channel velocity and the lateral shear results from the lateral variation of along-channel velocity. Taylor (1954) demonstrated that the horizontal spreading of waterborne material is controlled by the combination of vertical shear and vertical mixing. However, Fisher et al. (1979) showed that lateral shear and lateral circulation could make an important contribution to the longitudinal dispersion in estuaries. These shears are affected by a variety of processes such as turbulence, tidal currents, winds, and estuarine topography (Geyer & Signell, 1992). Many studies have focused on the vertical shear's effect and only a few pointed out the role of lateral shear. In a series of pioneering papers, Okubo (1971, 1973) summarized a wide range of dispersion studies and created an oceanic diffusion diagram that shows the eddy diffusivity to nonlinearly increase with the length scale of diffusion. There are studies on turbulent dispersion in the open ocean during recent decades (Garrett 2006), dispersion research was also conducted in estuaries. Wilson and Okubo (1978) provides abundant evidence for the importance of shear effect to longitudinal dispersion. Riddle and Lewis (2000) used dye tracing experiments to estimate horizontal and vertical mixing coefficients in coastal and estuarine sites. Their overall data analysis did not identify certain relationship between mixing coefficients and tidal current. Geyer et al. (2008) performed a dye release study in Hudson River estuary. Based on their limited observational data (first several hours after injection collection in 4 dye release experiments), they concluded that vertical shear dispersion was the principal mechanism

during neap tides but lateral shear dispersion became more important during spring tides. They also found significant differences in the dispersion rate for dye injections at different phases of a flood-ebb tidal cycle. However, other processes may also be considered to understand the details of dispersion, such as oscillatory shear due to tides, vertical or lateral mixing and shears, and tidal variations in vertical mixing due to tidal straining. Because of the limited length of observation data, they did not clearly distinguish the dispersion difference during neap and spring tides. Moreover, due to the very limited width of the Hudson River, it is still a question whether the conclusion by Geyer et al. (2008) will apply to relatively wide estuaries such as James River or Chesapeake Bay.

Fickian diffusion with a constant diffusivity would result in the variance growing linearly with time. Irrespective of the various macroscopic oceanographic conditions, the variance increases with time at a power of between 2 and 3, indicating non-fickian diffusion (Okubo, 1971). The 4/3 law demonstrates that the rate of effective diffusion (i.e., the dispersion coefficient) increases with the length scale of the scalar distribution in an order of 4/3. Many recent dye release studies in the ocean have corroborated the 4/3 law (Okubo 1971;Vasholz and Crawford 1985; Stacey et al. 2000; Fong and Stacey 2003; Jones et al. 2008; Moniz et al. 2014). Will the longitudinal dispersion in other estuaries such as James River follow the previous findings?

§1.3 Estuarine Dispersion of Salt

This thesis investigates both the temporal and spatial variations of salt dispersion in different estuaries. Salinity is a critical factor in understanding physical and biogeochemical processes in the estuaries. Many climatic and oceanic factors, including tidal currents and streamflow, have important influences on the salinity of the estuaries. The flux of salt into the estuaries may be influenced by processes such as steady shear dispersion and tidal oscillation; however, the estuaries response to these factors may be quite different.

Many studies have applied the Eulerian method of subtidal salt transport decomposition for estuaries (Bowen and Geyer 2003; Lerczak et al. 2006; Jia and Li, 2012; Chen et al., 2012; Aristizabal and Chant, 2013 and 2015). The total area-averaged and tidal-averaged salt flux was decomposed in three different contributions: the advective salt flux that represents the flux caused by river input and meteorological-induced flows, the steady shear dispersion that is the salt flux driven by the estuarine exchange flow, and the tidal oscillatory salt flux that is induced by the tidal currents.

The observation study in Hudson River by Lerczak et al. (2006) found that steady shear dispersion is the dominant mechanism in driving the upstream salt flux with the maximum during neap tides and minimum values during spring tides. They also indicate the variation in the advective salt flux has a period of 3-5 days and results from the variation in river discharge. However, their result is limited to a single section. There is not an indication whether the same conclusion could be applied to other sections in the longitudinal direction. The study in a lagoon by Jia and Li (2012) shows the wind's effect

on the advective salt flux. They also find that tidal pumping is active in the narrow outlet while steady shear dispersion is dominant in an inside section. Their finding in different sections indicates the variation of salt fluxes in the along-channel direction and their mechanism varies. Aristizabal and Chant (2013) applied an idealized model with constant river discharge to study the salt fluxes variation in one neap-spring tidal cycle in Delaware Bay. They suggest that the lateral flows bring velocity and salinity out of quadrature, which means salinity does not reach the maximum or minimum when velocity reaches zero, and induce a large tidal oscillatory salt flux. The assumption of constant river discharge in the model simplifies their analysis, but it may not predict the correct magnitude of the advective salt flux or the relative importance among three salt flux components. Again Aristizabal and Chant (2015) studied the salt flux across a mid-bay section in Delaware Bay using the observation data and found that the advective salt flux dominates over the steady shear dispersion and tidal oscillatory salt flux, and its fluctuation is driven mainly by wind. The along-channel variation of salt flux is not explained.

The tidal oscillatory salt flux could also play an important role in driving the upstream salt flux. Many attempts have been made to explain the variable mechanisms behind the tidal oscillatory salt flux. The most common mechanisms include the jet–sink theory (Stommel and Former, 1952; Jia and Li, 2012; Chen et al., 2012), tidal trapping (Okubo, 1973), tidal shear dispersion (Taylor, 1954; Bowden 1965; Fischer, 1973), chaotic stirring (Zimmerman, 1986) and hydraulic response (Wang et al, 2016). A recent study in Hudson River by Wang et al (2016) found that tidal oscillatory salt flux appears

to be a non-dispersive. They concluded that the tidal oscillatory salt transport is mainly due to the hydraulic response of the halocline to the longitudinal variation of topography during neap tide and thus is the advective transport of salt. All these studies reveal the uncertainties of the mechanisms driving the tidal oscillatory salt flux. Since there is not a unified theory to explain the tidal oscillatory salt flux, we consider whether there is an alternative method to explain the along-channel variation.

In different types of estuaries, the salt transport could be dominated by the advective salt flux (Aristizabal and Chant, 2015) or the steady shear dispersion (Lerczak et al., 2006) or various tidal pumping mechanisms (Jia and Li, 2012; Chen et al., 2012). There are limited studies on salt flux for Delaware Bay and seldom for Chesapeake Bay. Which scenarios fit the cases in the partially mixed Chesapeake Bay and the well mixed Delaware Bay? A comparative study of salt flux in two types of estuaries may provide new insights about what are the similarities and differences in the mechanisms controlling salt dispersion. Both temporal and spatial variation in two bays can be comprehensively considered. Is the fluctuation of advective salt flux mainly controlled by the variability of wind or the river discharge? Which salt flux is dominant in Chesapeake Bay and Delaware Bay? What is controlling the along-channel variation of tidal oscillatory salt flux? These questions will be answered by the dissertation.

The above studies apply the Eulerian method to the salt flux decomposition. However, sometimes, the Eulerian method may be limited when applied to short, salt-wedge types of estuaries such as the Merrimack (Ralston et al. 2010a), Columbia (Jay

and Smith 1990b), and Connecticut (Garvine 1975) River. Large tidal variations of the structure of the salinity intrusion and the associated salt flux make the assumption of steady baroclinic pressure gradient in the traditional Eulerian analysis inappropriate for short, tidally variable estuaries (Chen et al. 2012). This inspires estuarine investigators to seek alternative methods of quantifying salt flux that can be consistently used for different types of estuaries. MacCready (2011) used an isohaline coordinate to calculate the subtidal estuarine exchange flow. MacCready's (2011) analysis of the Columbia River salt flux suggested that the exchange flow calculated by the isohaline method was larger than that from Eulerian tidal averaging because the isohaline method incorporates tidal exchange processes. MacCready's analysis indicates that the isohaline method may provide a simpler and more robust mean of quantifying estuarine transport in highly time-dependent regimes. Will this method be applicable for Chesapeake Bay and Delaware Bay?

§1.4 Objectives

To answer these open questions, this dissertation uses a combined observational and numerical approach to study the estuarine dispersion: Specifically, we seek to

(1) Explain the temporal variation: Flood-ebb and spring-neap variation of dye dispersion in a partially mixed estuary;

(2) Clarify temporal and spatial variation of salt flux in two types of estuaries and differentiate the tidal and subtidal processes controlling the salt transport.

CHAPTER 2. TIME AND SCALE DEPENDENCE IN ESTUARINE LONGITUDINAL DISPERSION

Abstract

Dye-release experiments and numerical modeling are conducted to investigate horizontal dispersion in a partially mixed estuary. Longitudinal dispersion of a dye patch shows strong flood-ebb asymmetry at early times after a dye release, with most of the dispersion occurring during ebb tides. Tidal straining enhances vertical current shear on ebb tides and promotes longitudinal dispersion. There are also large differences in the dispersion rate between spring and neap tides. Due to strong spring mixing, a dye patch quickly extends from the bottom to the surface, exposing to the full vertical shear in the water column and leading to strong longitudinal dispersion. In contrast most of the dye patch is limited to bottom few meters during neap tides. Although weak vertical mixing facilitates longitudinal dispersion, the vertical shear across the thin dye patch is much weaker, leading to weak longitudinal dispersion during neap tides. At large times, the second moment of the dye patch in the along-channel direction increases with time at a power of between 2 and 3. The longitudinal dispersion rate varies as the four-third power of the dye patch size, indicating scale-dependent diffusion.

§2.1 Introduction

Dispersion of scalars is a long standing problem in estuarine physics (Fischer, 1976; Chatwin and Allen, 1985; Geyer and MacCready, 2014), and has a wide range of applications such as the disposal of sewage and industrial waste (Goldberg et al. 1978; Kadirvelu et al. 2001) and transport and dispersal of nutrients, plankton and fish larvae (Fortier and Leggett, 1982; Roman and Boicourt, 1999). Estuarine dispersion is

influenced by a myriad of processes, including turbulence, tidal currents, residual circulation, stratification and topography, thus making it difficult to study. However, the practical need for estimating the distribution and concentration of contaminants often demands a simple statistical description of the dispersion process. Typically, the longitudinal dispersion of scalars in an estuary can be described by the growth of the scalar variance

$$\sigma_x^2 = \frac{\iiint (x-\bar{x})^2 C dydzdx}{\iiint C dydzdx} \qquad (2.1)$$

where *x*, *y* and *z* are the along-channel, cross-channel and vertical directions, *C* is the scalar concentration, and $\bar{x}$ is the location of the centroid of the scalar mass in the along-channel direction. Assuming power-law dependence in time, the scalar variance can be written as

$$\sigma_x^2 = \alpha t^m \qquad (2.2)$$

where α is a dimensional constant and *m* defines the power law in time. In Fickian dispersion, *m=1* and the scalar variance grows linearly with time (Taylor, 1921), so that the longitudinal dispersion coefficient is given by

$$K_x = \tfrac{1}{2}\frac{\partial \sigma_x^2}{\partial t} = \tfrac{1}{2}\alpha. \qquad (2.3)$$

Scalar dispersion in the ocean often departs from Fickian diffusion (Young and Jones, 1991; Holleman and Stacey, 2013) with $m \neq 1$. In this case, the dispersion coefficient can be written as

$$K_x = \tfrac{1}{2}\alpha t^{m-1}. \qquad (2.4)$$

Substituting Eq. (2.2) into Eq. (2.4) yields

$$K_x = \frac{m}{2}\alpha^{1/m}\sigma_x^{[(2m-2)/m]} \qquad (2.5)$$

in which σ_x represents the length of the scalar distribution. Defining *n=(2m-2)/m*, Eq. (2.5) shows $K_x \propto \sigma_x^n$, indicating a scale-dependent dispersion. Relative dispersion in turbulent flows follows the famous "four-thirds" law with *n=4/3* (Richardson, 1926; Batchelor, 1952). Dye release studies in the ocean have largely confirmed this law (Obuko, 1971; Stacey et al., 2000), although other processes such as shear-flow dispersion in unbounded flows may be the dominant dispersion mechanism (Young et al., 1982; Garrett, 2006; Moniz et al., 2014).

In estuaries, tracer dispersion is affected by a number of competing processes. Vertical shear dispersion was used to explain the large diffusivity in the Mersey estuary and elsewhere (Bowden, 1965; Smith, 1977). Fischer (1972; 1979) showed that lateral shear dispersion significantly enhanced longitudinal dispersion. The oscillatory shear due to tidal currents may be much larger than the mean shear due to estuarine circulation, so that dispersion may be dominated by tidal processes. On other hand, tidal dispersion may be limited due to incomplete vertical mixing if the timescale of vertical mixing is much shorter than the tidal period (Young et al., 1982; Fischer et al., 1979). Tidal Straining may play an important in the dispersion process because it leads to tidal variation in vertical mixing (Simpson et al., 1990; Jay and Smith, 1990), which in turn results in tidal variations in the strength of vertical shear.

Geyer et al. (2008) conducted a comprehensive analysis of horizontal tracer dispersion in the Hudson River estuary. They released fluroscein dye in the bottom boundary layer on 4 separate occasions within varying tidal phase and spring-neap conditions, and tracked the dye for up to 30 hours. They found the average longitudinal dispersion rate of about 100 m^2/s, with an ebb maximum of 700 m^2/s and a flood minimum. They also found large differences in the dispersion rate between the spring and neap tides, and suggested that vertical shear dispersion was the principal mechanism during neap tides but lateral shear dispersion became more important during spring tides.

This study is an extension of the dye release study of Geyer et al. (2008). We conducted dye release experiments in the James River estuary, a partially mixed estuary that is much wider than the Hudson River estuary (Pritchard, 1956; Valle Levinson et al., 2000a; 2000b). Field experiments using fluorescein dye are usually limited to the first two tidal cycles: (1) field surveys could not capture all the dye, particularly in later stages when the dye patch had spread over a large area; (2) fluorescein dye experienced photo-degradation such that the total dye mass decreased with time. This study supplements field dye release experiments with numerical model simulations of dye dispersion. The modeling allows us to explore dispersion mechanisms in more details and can track the dye for an extended period of time without the concern for the chemical decay.

This paper is organized as follows. Section 2.2 describes the dye release field experiments in James River. Section 2.3 presents numerical modeling studies to track the dispersion of the dye patch. Section 2.4 discusses the flood-ebb and spring-neap

differences in the dispersion rate and scale-dependent dispersion at later times. Section 2.5 provides the conclusions.

§2.2 Field observations

2.2.1 Field experiments

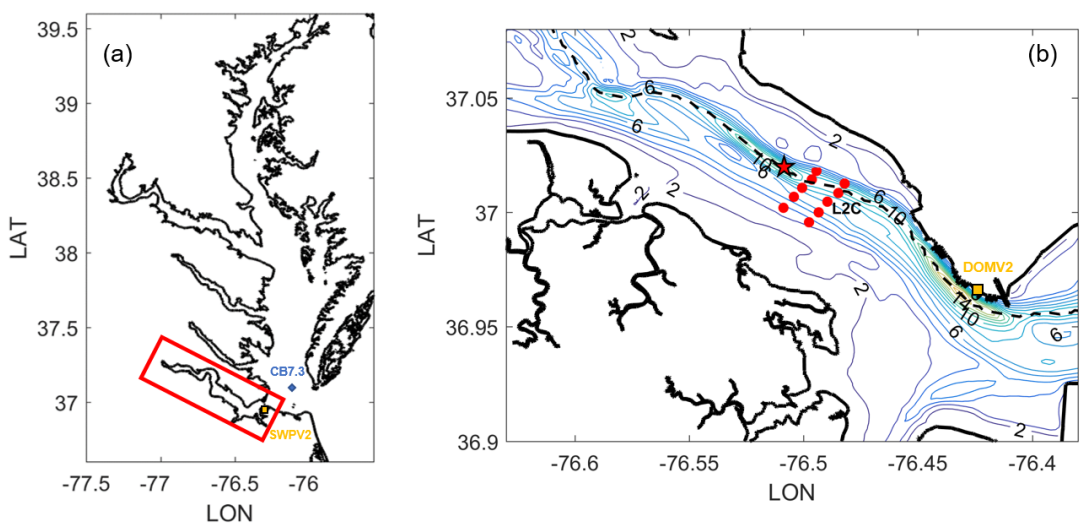

Figure 2.1 (a) Map of Chesapeake Bay and its southernmost tributary – the James River (marked by the red rectangle). Chesapeake Bay Program Station 7.3 is marked with blue rhombus. The yellow rectangle shows the location of weather station at Swells Point, VA (SWPV2). (b) Zoomed-in view of the James River section where dye injection experiments were conducted. The contours show the bathymetry while the red star indicates the approximate observed dye injection location. The red dots specify the location of 10 mooring stations including the central mooring station L2C. The yellow rectangle shows the location of weather station DOMV2.

The James River is the southernmost tributary to the Chesapeake Bay (Fig. 2.1a). It features a channel-shoal bathymetry, consisting of a main channel with a maximum depth of 15 m, located approximately between 0 and 2 km from the northern coast, and a secondary channel, 5-6 m deep, located roughly at 3 km from the northern coast. The field campaign was conducted over a relatively straight channel in the lower James River (Fig. 2.1b). Two mooring arrays were deployed between 28 April and 5 June 2010. They spanned over the entire cross sections and were spaced by 1 km in the along-channel direction. The moorings were equipped with 10 Doppler current meters, 23 CT sensors and four paroscientific pressure sensors. Four dye injection experiments were conducted near the mooring site (see Fig. 2.1b for the injection sites). The first set of two dye studies occurred during a neap tide in first week of May and the second set of two dye studies occurred during a strong spring tide during the last week of May. The location of each injection was selected such that the dye patch would pass through the mooring location during the first tidal cycle after injection.

Approximately 44 kg of fluoroscein dye was injected near the bottom during each release. The dye was diluted with seawater and alcohol to match the density of the target depth. The diluted dye was pumped through a hose to the target depth, 2–3 m above the bottom in the deep channel. The injection technique produced an initial stripe of dye approximately 1 m thick in the vertical, several m wide and about 300 m long. The dye injection took approximately 15 minutes. A CTD (conductivity, temperature, depth recorder) was mounted on the dye injection unit, and the depth of the release was

adjusted to maintain nearly constant salinity (and density) throughout the initial patch. The two-day separation between the two neap/spring injections allowed enough dilution and photo decay of the dye such that the first dye release should have minimal influence on the background concentration during the second dye release (Smart and Laidlaw, 1977).

The dye was tracked by two small vessels, each equipped with a profiling CTD/Fluorometer and an acoustic Doppler current profiler. The dye concentration was measured with an Aquatracka fluorometer mated to a CTD. One vessel surveyed cross-channel transects while the other surveyed the along-channel transects. Surveys of each dye patch began ~ 1 hour after injection and took approximately 1 hour to complete a transect. Six-eight patch surveys were obtained within a tidal cycle after each injection. The data covered a number of sections through the dye patch in both the cross- and along-channel directions until the dye signal was not detectable. Continuous surveying of the dye patch was conducted in the first 14 hours following the dye release, in order to resolve flood-ebb variability of the dispersion processes.

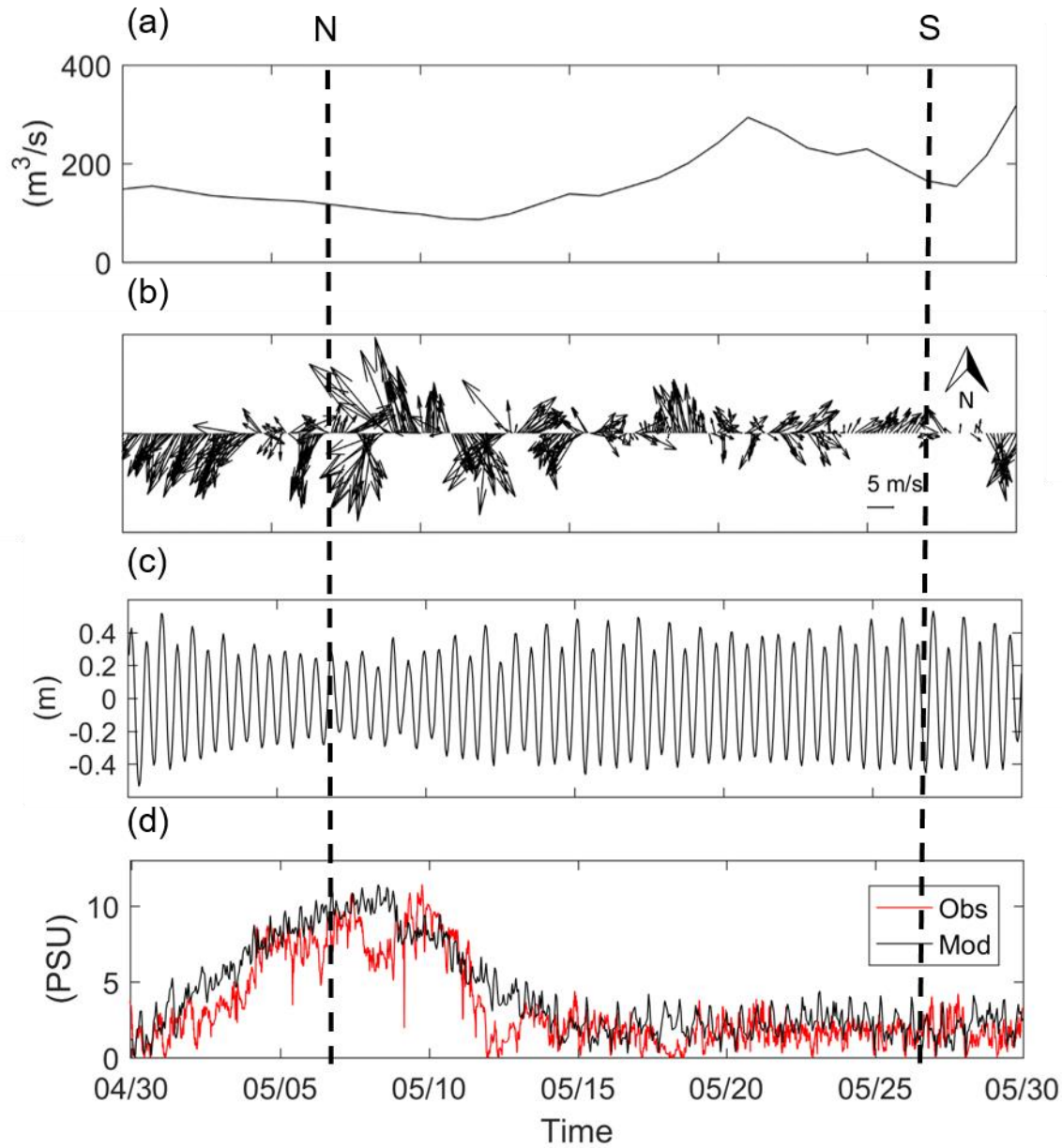

Figure 2.2 Time series of (a) river discharge at USGS station at Richmond, Virginia, (b) wind speed vector from the National Data Buoy Center station DOMV2, (c) observed tidal sea level at Swells Point, Hampton Roads, and (c) stratification at the central mooring station L2C. N marks the neap tide and S marks the spring tide.

The forcing conditions encountered during the dye-dispersion study periods are summarized in Figure 2.2. Daily river discharge Q was obtained from the stream flow data of the USGS (U.S. Geological Survey) station at Richmond, Virginia. It was low (100-150 m^3/s) between May 1 and 15, but doubled between May 16 and 31 with Q varying between 200 and 300 m^3/s (Fig. 2.2a). This compares with a typical peak of 500 m^3/s in March and a typical minimum of 80 m^3/s in August. Wind data were obtained from the NDBC (National Data Buoy Center) Station DOMV2, the meteorological station closest to the mooring site (Fig. 2.2b). The winds were weak between 05/14 and 05/27. Early in the mooring deployment, a wind event started on 05/06 and lasted until the end of 05/09. Water level data were obtained from the NOAA tidal station at the entrance to the James River estuary (Sewells Point, Virginia, Fig. 2.2c). Tides in the James River are predominantly semidiurnal: M_2, N_2, and S_2 are the three most energetic constituents, with M_2 carrying about 80% of the total tidal energy (Browne and Fisher, 1988). Due to the interactions between the three semi-diurnal constituents, the tidal currents exhibit spring-neap variations with monthly asymmetry (one extreme spring and neap per month). Tidal range was about 0.5 m during the weak neap tide (May 5-7) but reached 0.76 m during the strong spring tide (May 25-27). The spring-neap variation of the tidal currents resulted in large changes in the vertical stratification, as shown in Fig. 2d. The bottom-to-surface salinity difference at the mooring station L2C in the deep channel was about 8-10 psu during the neap tide but dropped to about 1-2 pus during the spring tide (Fig. 2.2d).

2.2.2 Observed dye dispersion

The boat surveys produced a sequence of maps of the dye distribution after each dye release. Figures 2.3-5 show four snapshots of the dye patch following an injection on May 27 during the spring tide. The dye was injected to the bottom boundary layer in the deep channel, at a depth of 10 m and salinity around 17 psu. In the plane view of the vertically integrated dye concentration, the dye was initially confined to the deep channel (at hour 3.6, Fig. 2.3a). The flood current advected the dye patch upstream and a second patch appeared on the southern shoal at hour 4.6 (Fig. 2.3b). While the dye patch was diluted and widened in the lateral direction, the length of the patch in the along-channel direction did not change much, indicating weak along-channel dispersion during this flood period. The ebb current advected the dye patch downstream (Figs. 2.3c and d). More noticeably, the dye patch grew dramatically in the along-channel direction, with a doubling of its length. This indicates strong longitudinal dispersion during the ebb tide. There were also changes in the lateral dye distribution, with the width of the dye patch contracting between 7.3 and 9.6 hours after the injection. In both the flood and ebb tide, the center of dye patch remained in the deep channel.

Distributions of the dye concentration in the along-channel and cross-channel sections provide a three-dimensional view of the dye patch. In the along-channel section, the dye patch remained trapped to the bottom layer (about 5 m from the sea bed) during the first 10 hours after the injection (Fig. 2.4). The dye patch displayed modest expansion on the flood tide (Figs. 2.4a and 4b) but expanded greatly in the along-channel direction

on the ebb tide (Figs. 2.4c and 4d). As the dye dispersed longitudinally, the dye concentration dropped. To examine lateral dye spreading, we select a cross-sectional transect closest to the dye centroid at each sampling time (its locations marked in Fig. 2.3). The dye began to spread from the center channel to the southern shoal at hour 3.4 (Fig. 2.5a). The sampling at hour 4.6 was limited to the deep channel and did not capture the full lateral extent of the dye patch (Fig. 2.5b). The second dye branch on the southern shoal was still seen in Fig. 2.5c but at much lower concentration due to dispersion and dilution. By hour 9.1, the dye batch spread over a broad cross section.

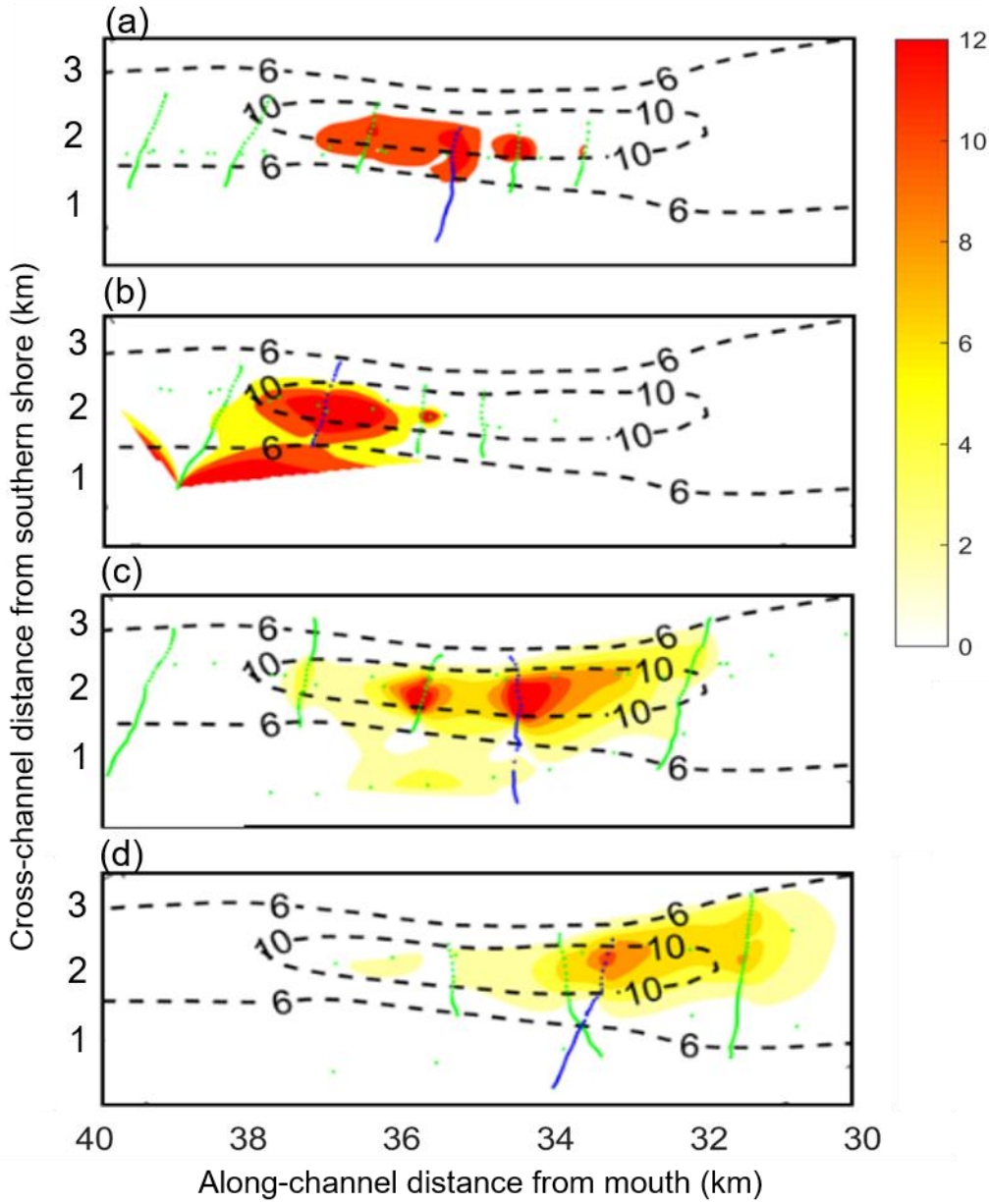

Figure 2.3 Plan view of the vertically integrated dye patch concentration (color, 10^{-5} kg/m^2) at (a) 3.6, (b) 4.6, (c) 7.3, (d) 9.4 hours after the dye release on May 27. The black dashed lines show bathymetry contours in meters. The dotted green and blue lines mark the cross-channel transects taken to sample the dye patch.

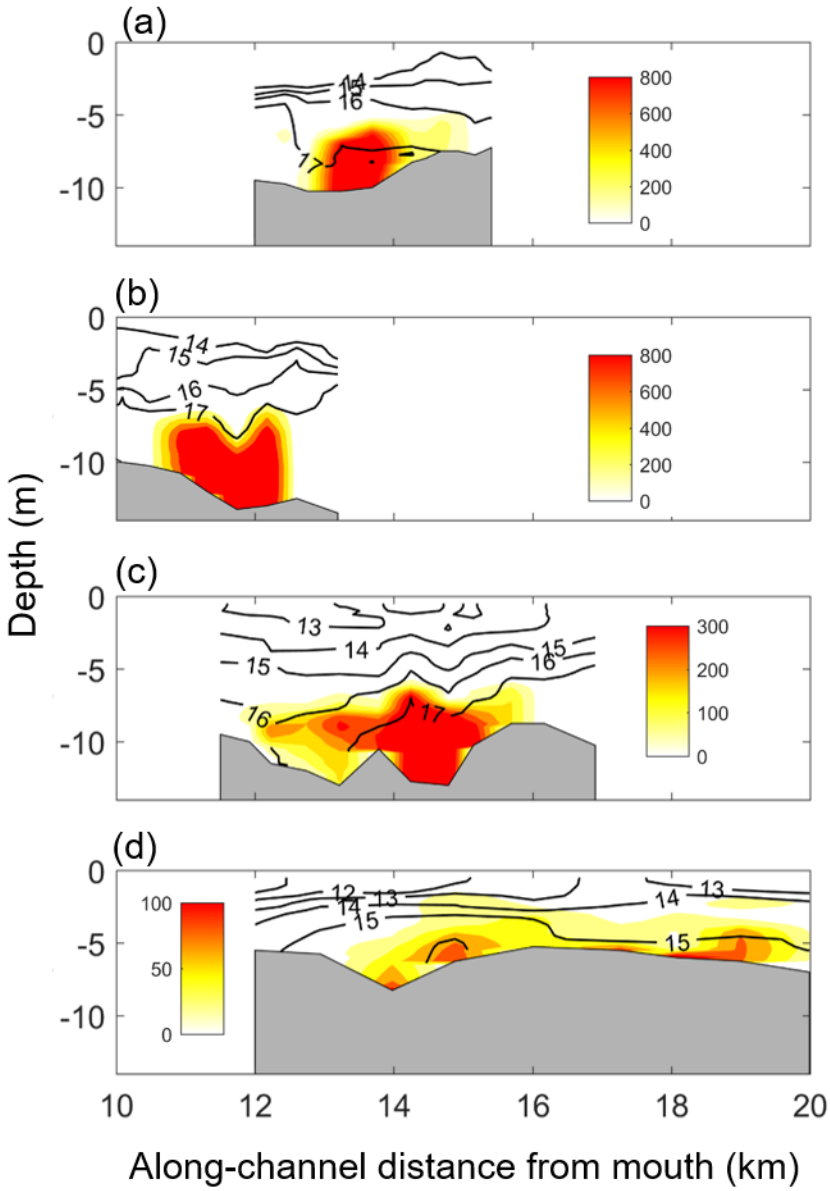

Figure 2.4 Along-channel distribution of dye concentration (color, 10^{-8} kg/m^3) and salinity (contour, psu) at (a) 3.9, (b) 4.5, (c) 8.3, (d) 9.7 hours after the May 27 release.

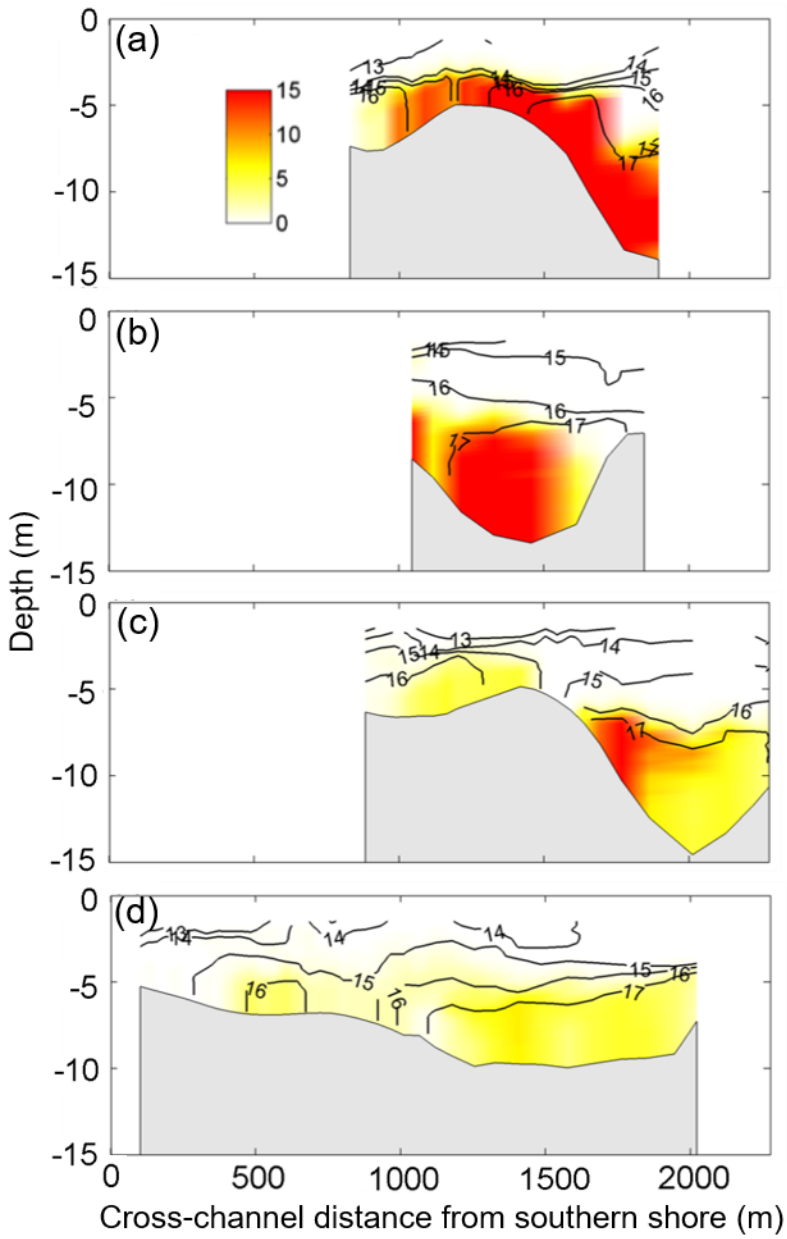

Figure 2.5 Cross channel distribution of dye concentration (color, 10^{-6} kg/m^2) and salinity (contour, psu) at (a) 3.4, (b) 4.6, (c) 7.9 and (d) 9.1 hours after May 27 release. The transect locations are marked as dotted blue lines in Figure 2.3.

To quantify the spreading of the dye in the longitudinal dimension (x), we calculate the second moment σ_x^2 of the dye patch, following the approach of Geyer et al. (2008). The dye measurements collected during the boat surveys are interpolated onto regularly-spaced grids. The dye concentration is averaged over the cross-channel sections to produce sectionally averaged dye concentration (Fig. 2.6). Its along-channel distribution is then fitted to a Gaussian of the form

$$C = C_0 \exp\left\{ \frac{\left(x - \bar{x}\right)^2}{2\sigma_x^2} \right\} \qquad (2.6)$$

where C_0 is the maximum concentration in the along-channel direction and $\bar{x}$ is the location of the centroid of the dye patch. Gaussian fitting to the along-estuary dye distribution reduces the sensitivity of the dispersion rate to the distribution of data, as shown by Geyer et al. (2008). The along-channel dye concentration generally follows the Gaussian distribution, with a regression coefficient r^2 exceeding 0.81 (Fig. 2.6). The value of σ_x^2 is determined by a least squares fit. The flattening of the curves over time indicates the longitudinal dispersion. Between 3.9 and 9.7 hours after the dye injection, the maximum dye concentration dropped from 800×10^{-8} kg/m^3 to $320 \times 10^{-8} \times 250$ kg/m^3 while the along-channel extent of dye increased from 2 km to 9 km. In addition, the center of the dye patch moved upstream and downstream due to tidal advection. Finally, the longitudinal dispersion rate is determined by the time rate of change of σ_x^2 (Eq. 3).

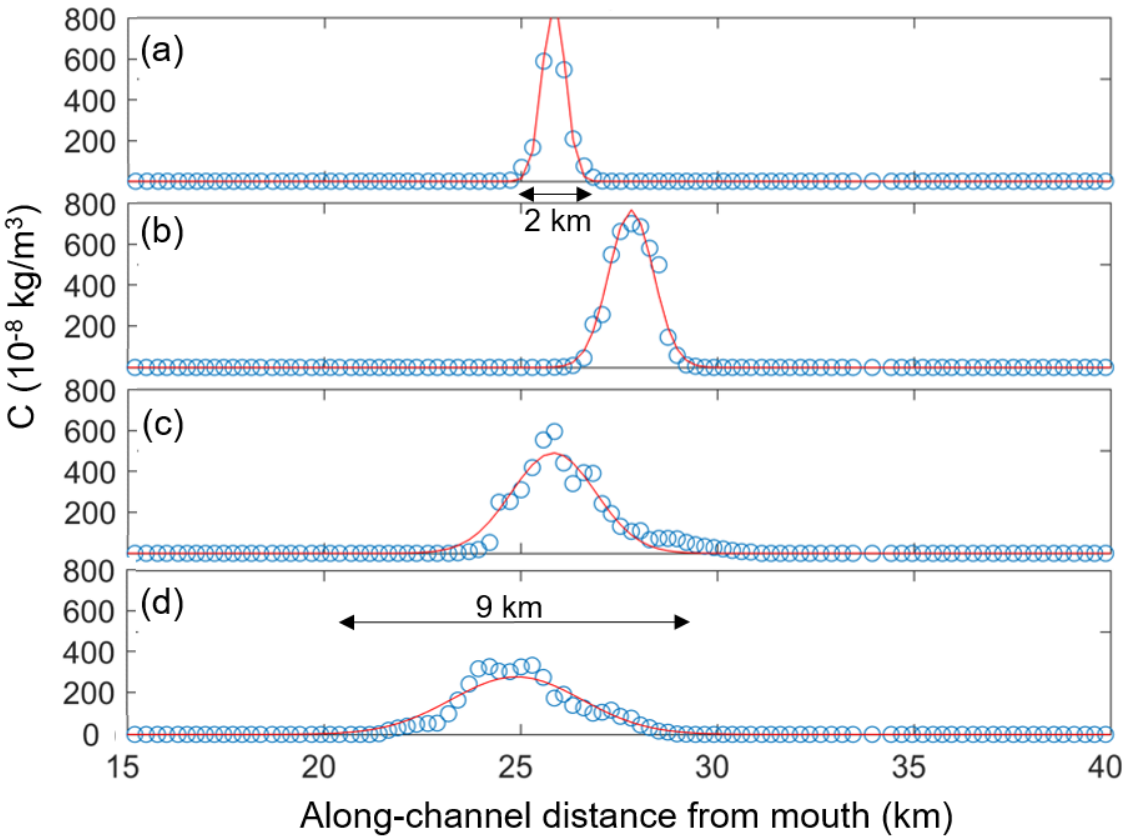

Figure 2.6 Gaussian Fitting to along-channel distribution of sectionally averaged dye concentration at (a) 3.9, (b) 4.5, (c) 8.3, (d) 9.7 hours after May 27 release. The blue dots mark the observed dye concentration and red lines are the fitted Gaussian curves.

The Gaussian fitting method is used to calculate σ_x^2 (defined in equation 3) for the May 27 dye release as well as for the three dye releases, using the dye surveys within the first 10 hours of the dye injections (Fig. 2.7). There are short term variations in the time series of σ_x^2, reflecting the flood-ebb asymmetry in the longitudinal dispersion as noted earlier, but all the time series show σ_x^2 increasing with time. However, not all the curves can be fit into straight lines. According to Eq. (2.4), this suggests that the longitudinal dispersion rate is not a constant and changes with time.

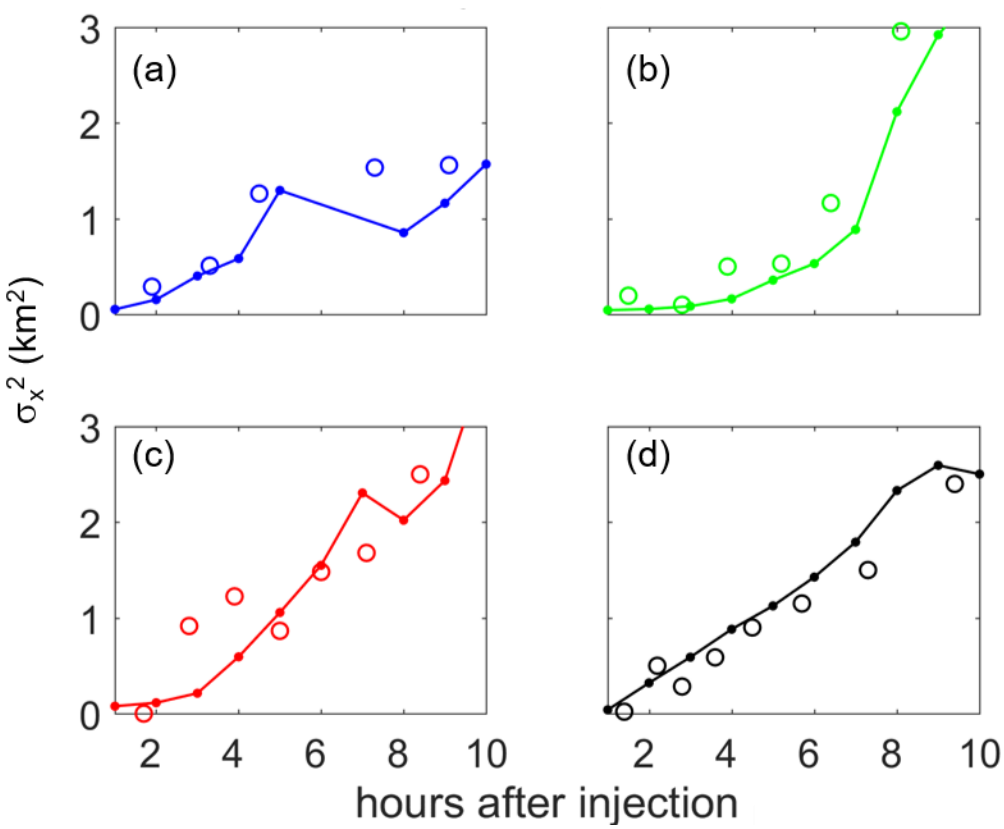

Figure 2.7 Time series of σ_x^2 calculated from the observed (dots) and the predicted (lines) dye distribution for the four dye experiments: (a) May 5, (b) May 7, (c) May 25 and (d) May 27.

§2.3 Numerical modeling

The dye release experiment shows flood-ebb asymmetry and spring-neap differences in the longitudinal dispersion and motivates a modeling study to probe underlying dispersion mechanisms.

2.3.1 Model configuration and validation

We have configured the Regional Ocean Modeling System (ROMS) for the James River. The model domain covers the entire James River estuary and part of the main stem of Chesapeake Bay to establish the open boundary condition (Fig. 2.8). The domain extends upstream by ~100 km to damp out tides at the upstream river boundary, following the approach by Warner et al. (2005a). Bathymetry in the river is extracted from the high-resolution Coastal Relief Model data archived at NOAA's National Geophysical Data Center. The grid spacing is about 100 m in the horizontal direction and the total number of grid points is 120x410. There are 20 terrain-following σ-layers in the vertical direction. The horizontal eddy viscosity and diffusivity are set to 1 $m^2 s^{-1}$ (Zhong and Li, 2006). The vertical eddy viscosity and diffusivity are computed using the k-kl turbulence closure scheme (Warner et al., 2005b) with the background diffusivity and viscosity of 10^{-6} $m^2 s^{-1}$. A quadratic stress is implemented at the sea bed, assuming that the bottom boundary layer is logarithmic with a roughness height of 0.5 mm (Li et al., 2017).

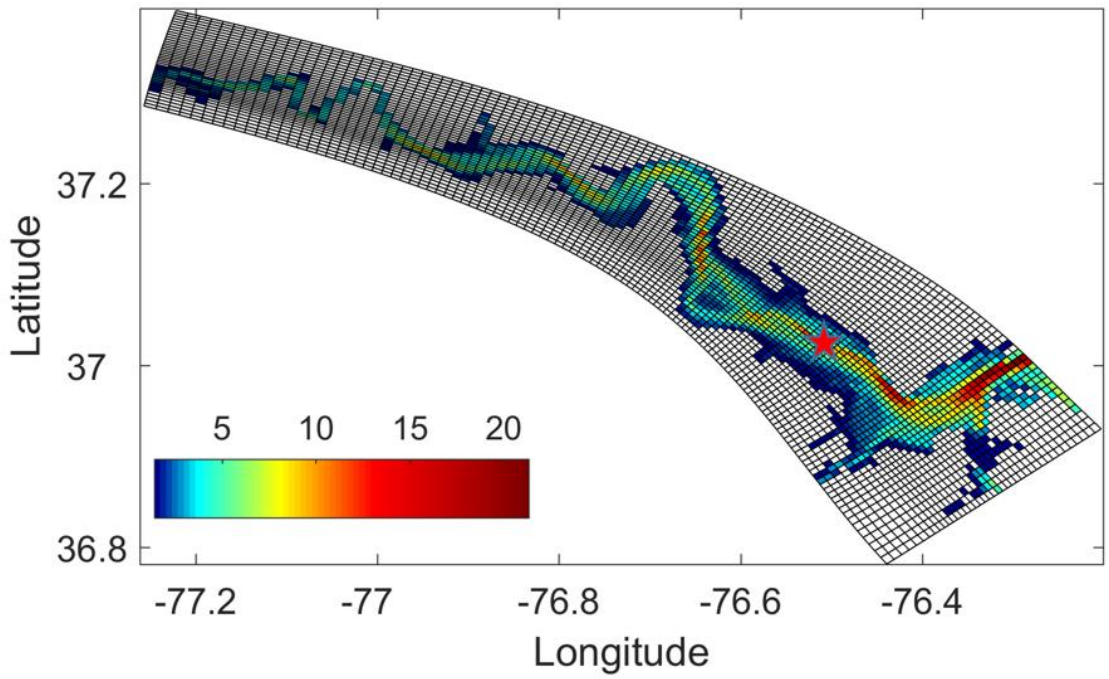

Figure 2.8 ROMS grid and bathymetry of the James River Estuary with the approximate dye injection location marked by red star. Grid points are plotted at every three other points.

The model is forced by river flow at the upstream (western) boundary and by tides at the eastern open boundary. At the upstream boundary, a momentum boundary condition is imposed on the depth-averaged velocity as determined by the river flow. Water in the river is prescribed to have zero salinity. Tidal forcing at the open boundary is specified using tidal harmonics analysis of the observed water level at a tidal gauge station near the open boundary (Hampton Roads, V.A.). Tidal elevation is decomposed into five major tidal constituents, M_2, S_2, N_2, K_1 and O_1. Salinity at the open boundary is specified using the water-quality data obtained at a nearby Chesapeake Bay monitoring

station CB7.3. The open-ocean boundary is treated with a Chapman's condition for surface elevation, a Flather's condition for barotropic velocity, and an Orlanski-type radiation condition for baroclinic velocity and scalars (Marchesiello et al., 2001).

We have run the ROMS model from year 2008 to 2010. Li et al. (2017) used this model to interpret the observed flood-ebb and spring neap variability of the lateral circulation. The model showed a very good skill in reproducing the observed tidal sea levels, tidal currents, stratification (e.g. Fig. 2.2d) and lateral currents, thus laying a solid foundation for the numerical dye experiments in this study.

ROMS incorporates a module to track passive scalars. We take the Eulerian approach by solving an advection-diffusion equation for the dye. Concentration and location data from the first observed dye patch are used to set the initial condition of dye concentration. A total of four numerical dye experiments are conducted to simulate the conditions corresponding to the four dye injections: two at the slack before flood tide on May 5 and May 25 and two at the slack before ebb on May 7 and May 27. The numerical dye simulations run for a period of 48 hours after each dye injection, in order to investigate the long term dye dispersion that could not be captured by the field observations while most of the dye mass is still contained inside the model domain.

To examine if the model reproduces the observed dye dispersion, σ_x^2 is calculated from the model-predicted dye distributions and compared with the observed dispersion for the first 10 hours when the dye measurements were available (Fig. 2.7).

σ_x^2 is calculated using the same Gaussian fitting method. A few data points (e.g. hours 6, 7 in May 5) are omitted because the along-channel dye distributions obtained from the model do not fit well with the Gaussian function. Overall there are reasonable agreements on the time series of σ_x^2 between the model predictions and observations.

2.3.2 Dye dispersion during spring tide

To investigate in detail how the dye patch is advected and dispersed, we plot the following figures which provide a three dimensional view of the dye distribution: (1) plane view; (2) along-channel section; (3) cross-channel section. May 27 release is used for studying dye dispersion during the spring tide.

Six snapshots of the horizontal distribution of the vertically integrated dye concentration are shown in Figure 2.9: four during the first two tidal cycles after the dye release and two at 36 and 48 hours after the release. At hour 3 (flood tide), the dye patch was a small blob situated in the deep channel (Fig. 2.9a). At hour 9 (ebb tide), the dye patch was split into two blobs: one in the deep channel and one on the southern shoal (Fig. 2.9b). At the following flood tide (hour 15), the dye was elongated in the longitudinal direction but the two patches merged in the upstream end (Fig. 2.9c). The dye patch experienced much more spreading during the next ebb tide (hour 21), with its longitudinal extent more than doubled and its width expanding to the shallow shoals (Fig. 2.9d). The longitudinal dye dispersion was much larger during the two ebb tides than during the two flood tides, in agreement with the flood-ebb asymmetry noted in the

observations (see Fig. 2.3). At later times, the flood-ebb asymmetry was not as pronounced because the length of the dye patch (about 30-40 km) exceeded the tidal excursion distance (about 4 km). Due to continuous dispersion, the peak dye concentration at hour 36 was about 1/20 of that at hour 3 (Fig. 2.9e). A significant part of the dye patch was stretched along the southern shore of the lower James River. By hour 48, the dye patch had spread to the lower estuary, covering the southern half of the estuarine channel there. The total dye mass was 100% conserved over 48 hours, indicating that no dye was leaked out through the model's open boundary.

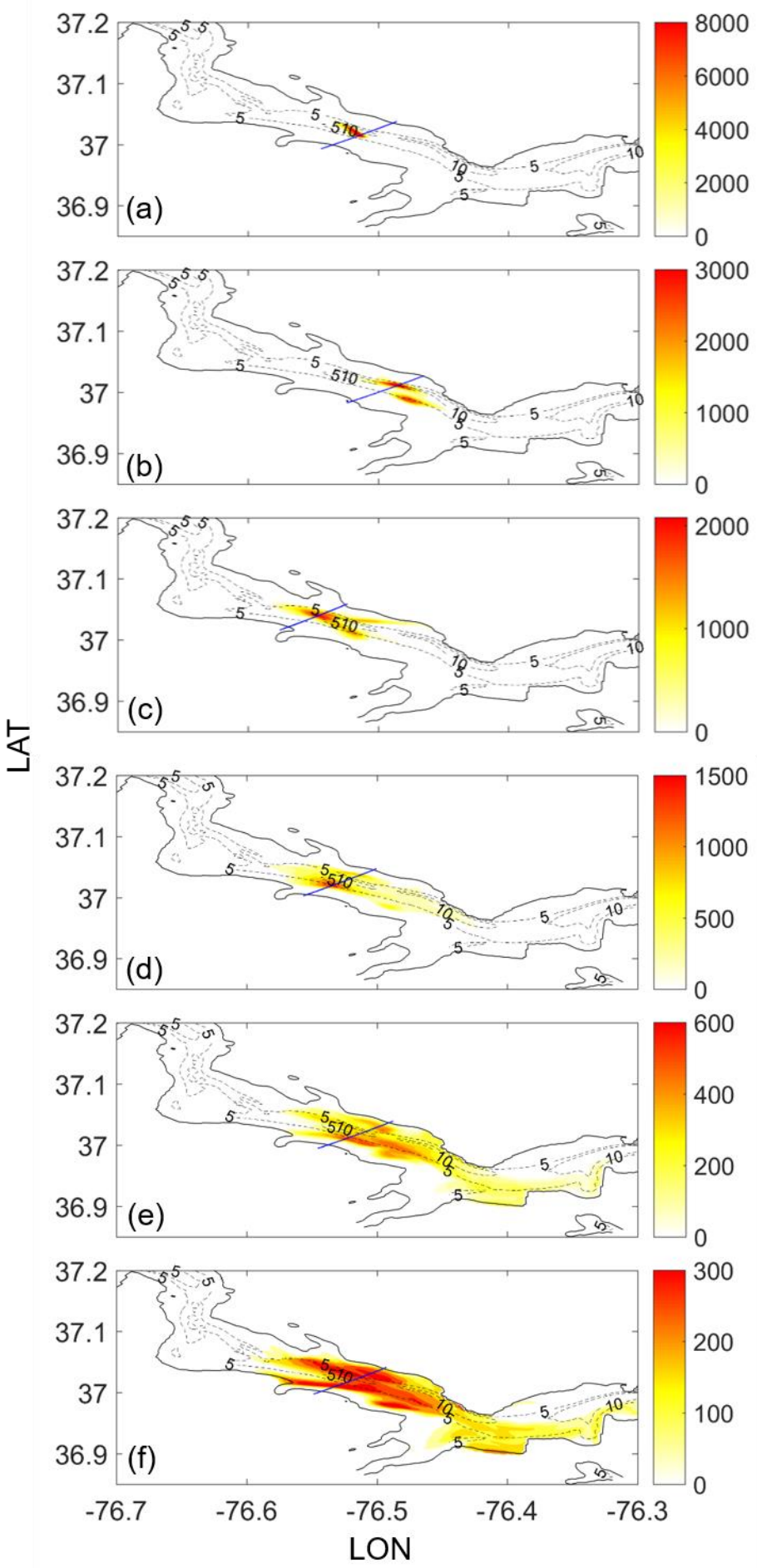
(a)
(b)
(c)
(d)
(e)
(f)
LAT
LON
37.2
37.1
37
36.9
-76.7
-76.6
-76.5
-76.4
-76.3
8000
6000
4000
2000
0
3000
2000
1000
0
2000
1000
0
1500
1000
500
0
600
400
200
0
300
200
100
0

Figure 2.9 Plan view of the model-predicted vertically integrated dye concentration at 3, 9, 15, 21, 36 and 48 hours following the dye-release on May 27. Blue dots represent the cross-channel locations in Figure 2.11.

The dye distribution in the along-channel section is plotted in Figure 2.10. To see how the dye patch is affected by the currents and mixing, we also plot the along-channel velocity, salinity and vertical eddy diffusivity. Under the spring conditions of May 27, the vertical stratification was weak, with the bottom-to-top salinity difference of 1-2 psu. Strong tidal mixing produced a thick bottom boundary layer, with the eddy diffusivity reaching 10^{-2} m^2/s. At hour 3, mixing in the bottom boundary layer thickened the dye patch to a height of 5 m as the flood current advected it (together with water with salinity of ~14 psu) upstream (first row). Tidal straining during the following ebb tide restratified the water column and reduced the mixing (second row). The combination of weaker mixing and strong vertical shear caused the dye to disperse horizontally, a clear manifestation of the vertical shear dispersion mechanism that was first articulated by Taylor (1953). It is interesting to note that the dye patch appeared to spread along the sloping isopycnals between 12 and 14 psu. This is similar to the eddy-induced stirring along isopycnals in the open ocean (Garrett, 2006). The next flood current partially reversed the along-isopycnal spreading while the stronger turbulent mixing associated with the flood tide straining caused the dye patch to extend nearly to the sea surface (row 3). Subsequently, the dye experienced the vertical shear in the ebb current across the entire water depth, resulting in much stronger longitudinal dispersion (row 4). As the length of dye patch surpassed the tidal excursion distance, the tidal straining effects were

local and did not cause major differences in the overall patch size. The horizontal dye dispersion was more rapid at this late stage as the full depth of the vertical shear was involved in dispersing the dye (rows 4 and 5). Hour 36 was at the slack tide and hour 48 was in early flood such that the vertical eddy diffusivity was small. The along-channel dye distributions did not capture the branch of the dye patch in the lower estuary shown in Figs. 2.9e and 9f since this branch moved off the deep channel.

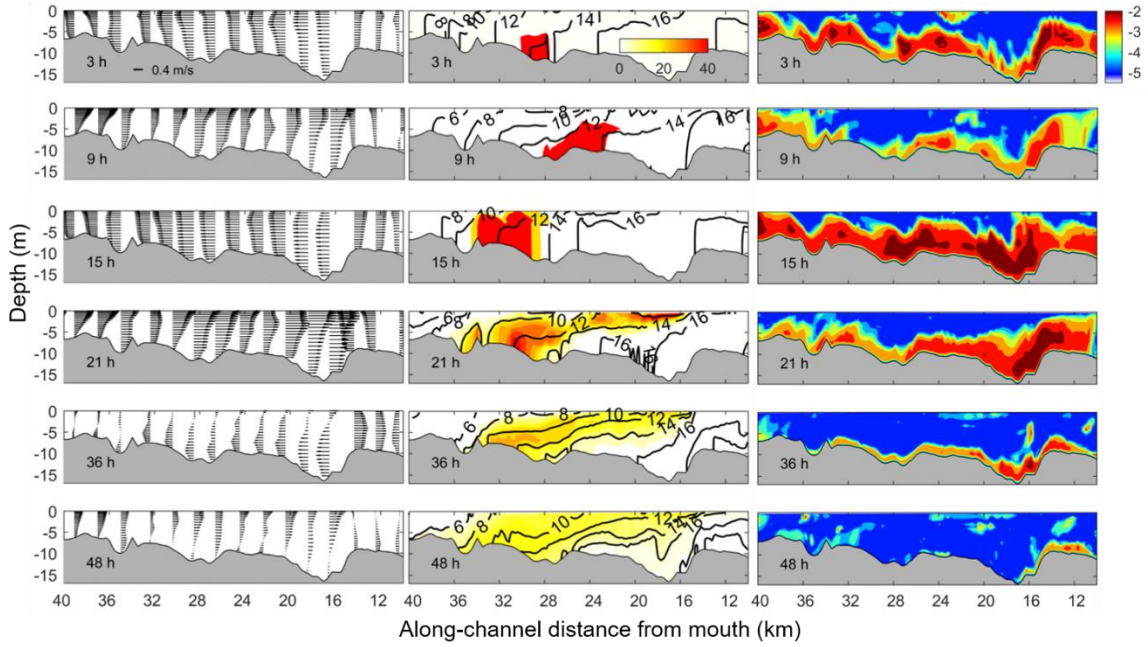

Figure 2.10 Along-channel distributions of along-channel velocity (left column), salinity (contours) and dye concentration (color, 10^{-8} kg/m^2) (middle column) and vertical diffusivity (m^2/s) (right column) at 3, 9, 15, 21, 36 and 48 hours after May 27 release.

The bifurcation of the dye patch into two pieces and their subsequent merging (shown in Figs. 2.9a-c) revealed that the lateral circulation affected the dye dispersion (Fig. 2.11). The dye was initially injected to the deep channel of the estuary, and the clockwise lateral circulation on the flood tide advected the dye patch towards the shallow

southern shore (first row). On the following ebb tide, the lateral circulation consisted of a counter-clockwise circulation which advected the blob back to the deep channel (second row). However, the width of the dye patch increased substantially. The dye patch appeared to be split into two blobs (third row), as the preceding clockwise circulation advected the main blob onto the southern shoal while the remaining dye got dispersed in the deep channel. This bifurcation could be seen more clearly at downstream sections, as shown in Fig. 2.9c. In the subsequent ebb tide, the dye patch not only occupied the deep channel but also spread over significant portions of the southern and northern shoals (fourth row). Over the next 24 hours, the dye patch gradually filled in the entire cross section (fifth and sixth rows), as the lateral dispersion almost achieved nearly uniform dye concentration in the cross section.

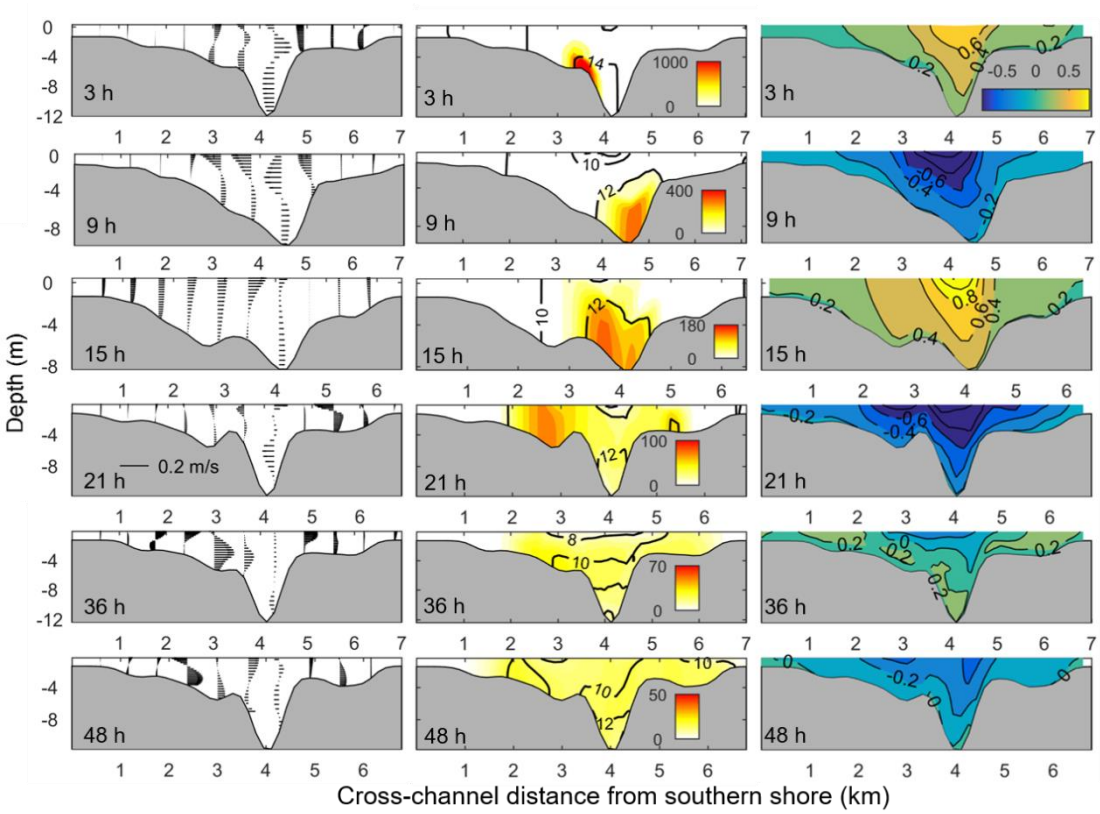

Figure 2.11 Cross-channel distributions of lateral velocity (left column), salinity (contours) and dye concentration (color) (middle column) and along-channel velocity (right column) at 3, 9, 15, 21, 36 and 48 hours after May 27 release.

2.3.3 Dye dispersion during neap tide

For comparison the time evolution of the dye patch for the neap injection on May 5 is shown in Figs. 2.12-14. The plane view of the vertically integrated dye concentration shows a dye patch that was initially confined to the deep channel (hour 6, Fig. 2.12a), bifurcated into two patches during the ebb tide (hour 12, Fig. 2.12b), merged into one during the flood (hour 18, Fig. 2.12c), and bifurcated again in the following ebb (hour 24, Fig. 2.12d) but with higher dye concentration on the southern shoal. Over the next 12 and 24 hours, the dye spread across the whole estuary's cross section and experienced strong longitudinal dispersion (Figs. 2.12e and 2.12f). Compared with the dye distribution at the same time during the spring tide, the length of the dye patch was much shorter.

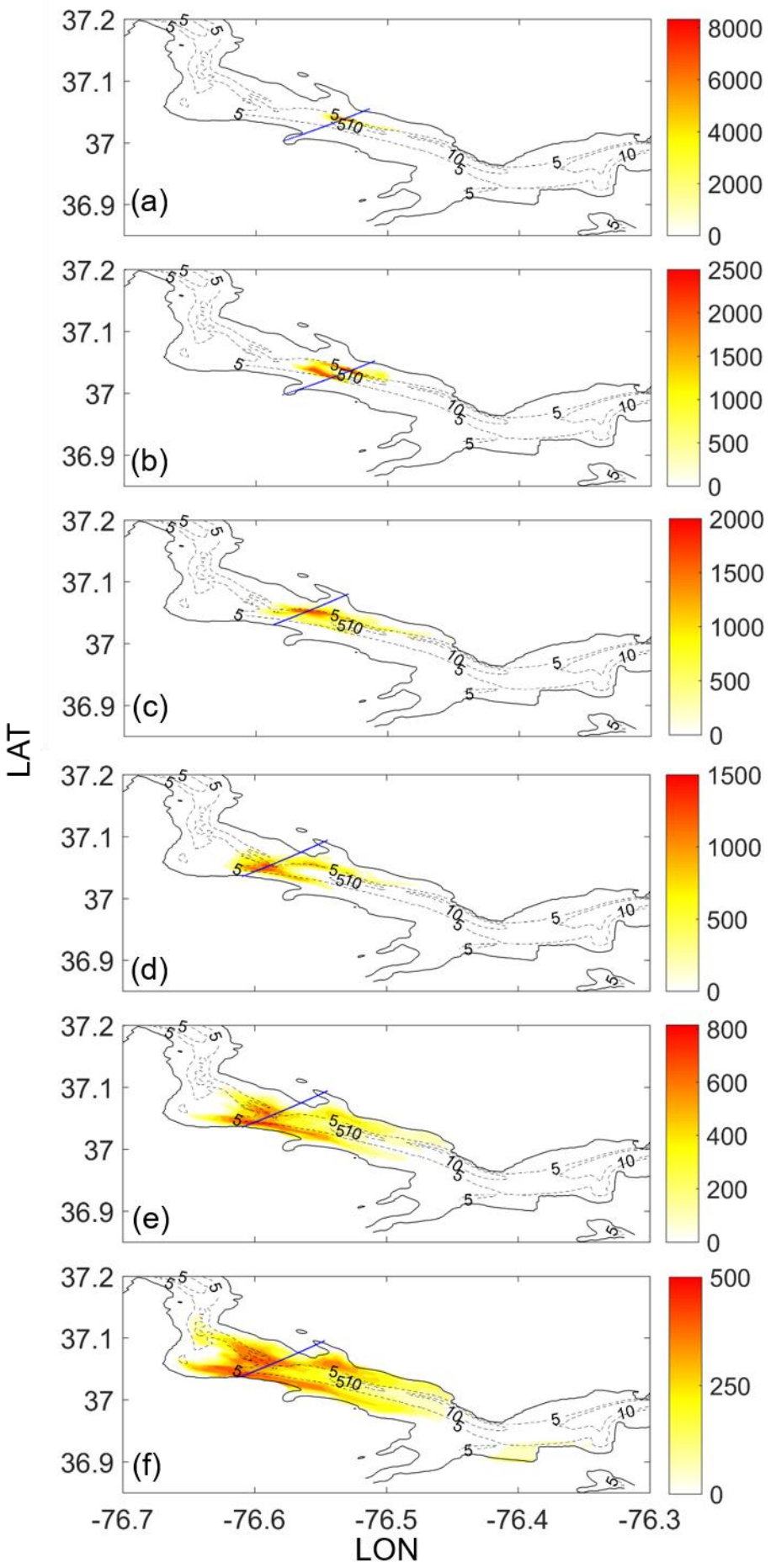
(a)
(b)
(c)
(d)
(e)
(f)
LAT
LON
37.2
37.1
37
36.9
-76.7
-76.6
-76.5
-76.4
-76.3
8000
6000
4000
2000
0
2500
2000
1500
1000
500
0
2000
1500
1000
500
0
1500
1000
500
0
800
600
400
200
0
500
250
0

Figure 2.12 Plan view of the model-predicted vertically integrated dye concentration at 6, 12, 18, 24, 36 and 48 hours following the dye release on May 5. Blue dots represent the cross-channel locations in Figure 2.14.

The weaker longitudinal dispersion is related to the fact that strong neap stratification limited the vertical penetration of the dye patch, as shown in the along-channel distribution of the dye concentration (Fig. 2.13). The effect of tidal straining on the patch dispersion was still evident: strong flood mixing grew the dye patch vertically (up to the pycnocline) (rows 1 and 3) and strong ebb shear and weak mixing promoted horizontal shear dispersion (rows 2 and 4). At hour 24, a branch of the dye patch stretched along the isohalines of 10 psu (row 4). Over the next 24 hours, the dye patch essentially spread across the isohalines of 8-12 psu (row 5 and 6). Little dye concentration was found in waters of other salinity classes. Unlike the spring tide in which strong mixing expanded the dye patch across the whole water depth, the neap strong stratification confined the dye patch to bottom waters and only allowed it to spread along isohaline surfaces, thus limiting the exposure of the dye patch to the vertical shear dispersion and leading to weaker longitudinal dispersion.

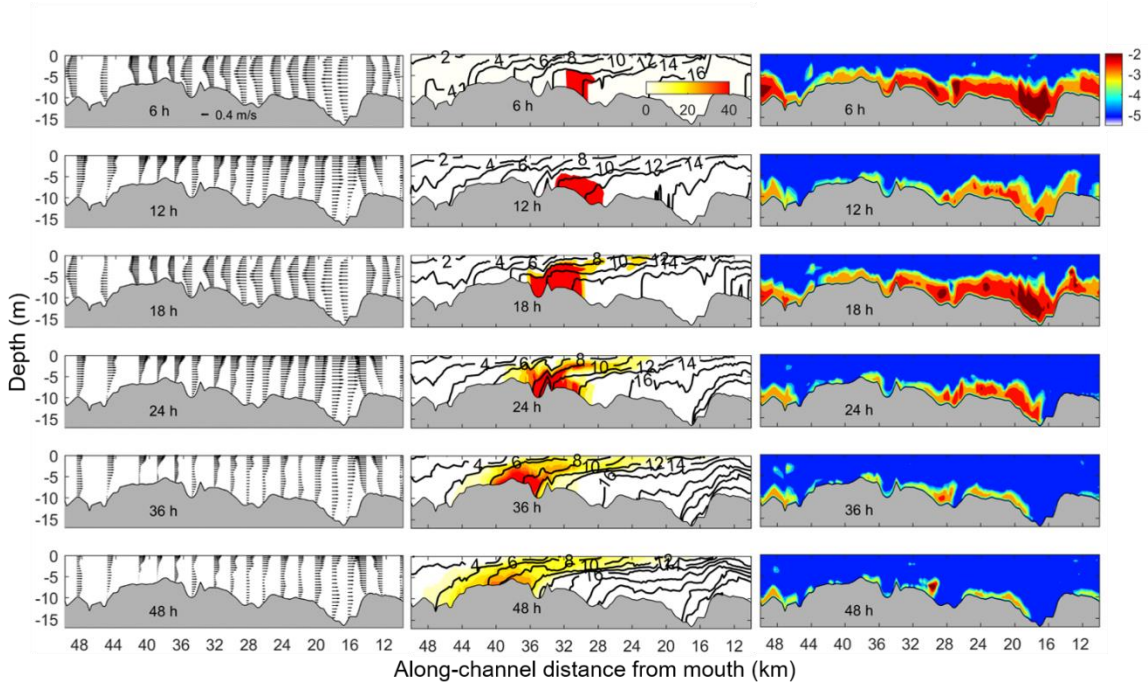

Figure 2.13 Along-channel sections of along-channel velocity, dye patches concentration and vertical diffusivity at 6 (flood), 12 (ebb), 18 (flood), 24 (ebb), 36, and 48 hours after May 5 release. Concentration is in unites of 10^{-8} kg/m2; vertical diffusivity is plotted using a log-10 scale.

Similar effects of the lateral circulation on the dye dispersion in the cross-channel section were seen during the neap tide (Fig. 2.14). During the first tidal cycle after the dye release, the dye patch in the deep channel was split into two by the clockwise lateral circulation during the flood tide (first row) whereas the counter-clockwise lateral circulation during the ebb tide advected the secondary patch on the southern shoal towards the deep channel (second row). This process was repeated during the second tidal cycle (third and fourth rows), but substantial lateral dispersion had occurred over this tidal period, with the dye patch occupying the most of the cross-channel section. Over the

next 24 hours, the gradients in the dye concentration were reduced due to continued mixing and dispersion (fifth and sixth rows).

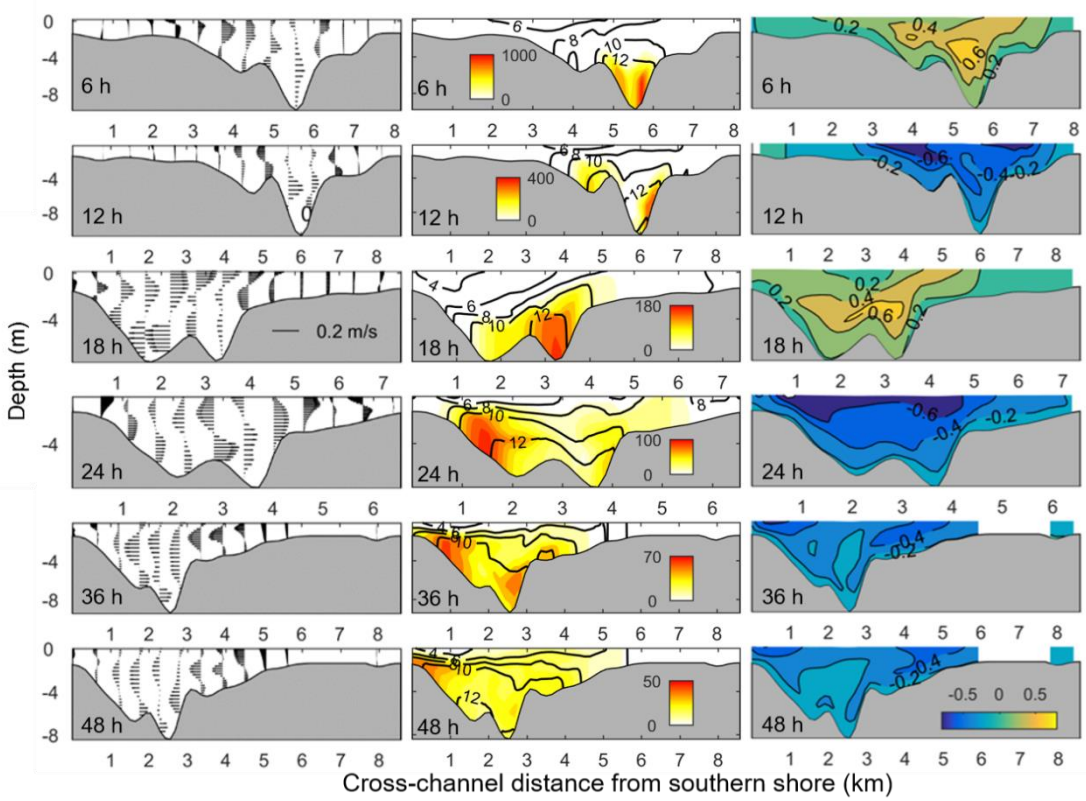

Figure 2.14 Cross-channel sections of cross-channel velocity (a-f), dye patches concentration (g-l) and along-channel velocity (m-f) at 6 (flood), 12 (ebb), 18 (flood), 24 (ebb), 36, and 48 hours after May 5 release.

§2.4 Discussion

2.4.1 Flood-ebb and spring-neap variations in the longitudinal dispersion

The temporal evolution of the dye distribution reveals a clear difference in the longitudinal dye dispersion between the flood and ebb tides. To quantify this difference,

we plot the time series of σ_x^2 calculated from the model outputs (Fig. 2.15). Assuming a Fickian diffusion, we estimate K_x. During the neap tide of May 5, K_y was around 25 m^2/s during the first flood tide but jumped to 200 m^2/s in the following ebb tide (Fig. 2.15a). In the second flood tide, K_x weakened dramatically to 15 m^2/s. Similar strong flood-ebb asymmetry in the longitudinal dispersion was found during the spring tide of May 27 (Fig. 2.15b). In the first ebb tide after the dye release, K_x was around 30 m^2/s. However, the dye patch shrank in the longitudinal direction in the following flood tide, with K_x = -10 m^2/s. In contrast, the dye dispersed rapidly in the subsequent ebb tide, with K_x reaching 500 m^2/s.

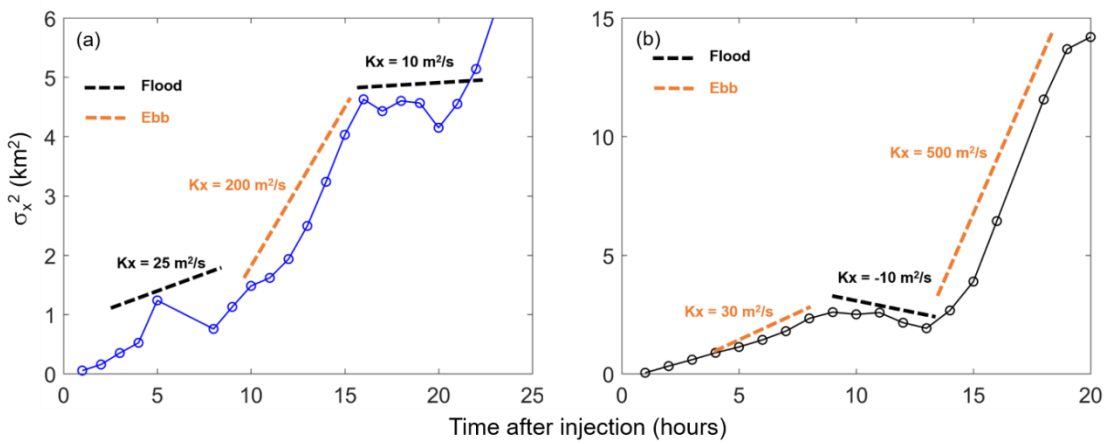

Figure 2.15 Time series of σ_x^2 in the first 24 hours after the dye release: (a) May 5 and (b) May 27. σ_x^2 increases with time rapidly during ebb tide but shows slow increases or contraction during the flood tide. The numbers are the estimated longitudinal diffusivity for the flood and ebb periods.

What causes this flood-ebb asymmetry in K_x? The vertical shear in the ebb current is amplified by the residual estuarine circulation while stronger ebb stratification

suppresses vertical mixing. In comparison, the vertical shear in the flood current is weakened by the residual estuarine circulation while turbulent mixing is enhanced. Consistent with Taylor's (1954) classic theory for shear dispersion, K_x is much larger during the ebb tide. This tidal straining effect was observed in all the four dye experiments. In the dye-release experiments in the Hudson River estuary, Geyer et al. (2008) also reported that ebb tides contributed most to the longitudinal dispersion.

In addition to the flood-ebb asymmetry in the longitudinal dispersion, there were large differences in K_x between the spring and neap dye releases, as shown in Fig. 16a. These differences could also be qualitatively interpreted from Taylor's (1954)'s formula for horizontal shear dispersion

$$K_x = \alpha \frac{u^2 h^2}{K_z} \qquad (7)$$

where u is the magnitude of the vertical variation of velocity, h is the water depth, K_z is the vertical turbulent diffusivity, and alpha is a coefficient (~1–10×10^{-3}) that depends on the vertical structure of the velocity and diffusivity (Bowden, 1965). Due to strong turbulent mixing during the spring tide, the dye patch quickly extended from the bottom to the surface. The dye patch was thus exposed to the vertical shear in the entire water column such that the vertical shear dispersion was most effective. In contrast, most of the dye was limited to the bottom few meters during the two neap releases due to weak mixing. Although weak vertical mixing may facilitate longitudinal dispersion based on Taylor's equation, there was smaller vertical shear across the thin dye patch during the neap tide. Consequently, K_x is much smaller during the neap tide than the spring tide.

Although the large spring-neap differences in the dispersion rate are consistent with the interpretation in terms of the vertical shear dispersion, other mechanisms have been proposed to explain the differences. Geyer et al. (2008) found evidence of a cross-estuary shearing of the dye patch in the Hudson River estuary and suggested that lateral shear dispersion due to the cross-channel variation of the along-channel currents may be more important than the vertical shear dispersion during the spring tides. In the wide James River estuary, the vertical shear is always greater than the lateral shear during both spring and neap tides (the third column in Fig. 2.11 and 2.14), such that the lateral shear dispersion may be of secondary importance. On the other hand, Figures 11 and 14 clearly show that the lateral circulation contributes to the longitudinal dye dispersion by splitting and distributing the dye patch in cross-channel sections and exposing it to the along-channel currents of varying magnitude (higher velocities in the deep channel than on the shallow shoals), thereby enhancing the longitudinal dispersion. Nevertheless, the lateral circulation cannot explain the large spring-neap differences in the longitudinal dispersion rate because both the observations and modeling studies showed that the lateral circulation strength in the James River did not change much over the spring-neap tidal cycles (Li et al., 2017).

2.4.2 Scale-dependent dispersion at large times

The time series of σ_x^2 clearly deviate from straight lines, particularly at large times (Fig. 2.16a). Figure 2.16b suggests that σ_x^2 could be better fitted into a power law (Eq. 2.2) with $2<m<3$, indicating non-Fickian diffusion. Okubo (1971) found that the

variance of tracers in the ocean increases with time at a power of around 2.34 and *m* varies between 2 and 3 for various macroscopic oceanographic conditions. The results from the four dye experiments generally fall in this range: with *m* on spring tides close to 3 and on neap tides close to 2.34.

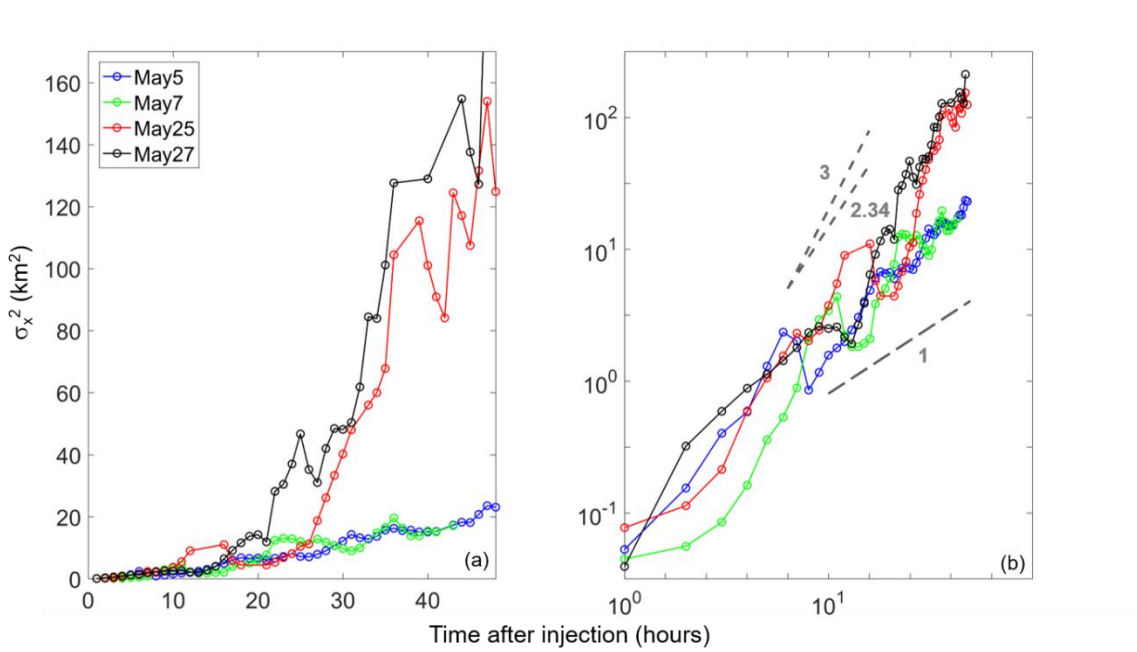

Figure 2.16 σ_x^2 versus time during four releases: (a) linear scale; (b) log scale. The grey dashed lines indicate the slope of 1, 2.34 and 3, respectively.

The power law time dependence of σ_x^2 implies a scale-dependent dispersion, as shown in Eq. (2.5). We plot K_x as a function of the dye patch size which is estimated using σ_x. Figure 2.17 shows K_x scales approximately as $(\sigma_x)^{4/3}$, which is consistent with the famous "four-thirds" law describing relative dispersion in turbulent flows (Richardson, 1926; Batchelor, 1952). Such power law was also found to describe the oceanic dispersion in a wide range of flow conditions (Okubo 1971;Vasholz and

Crawford 1985; Stacey et al. 2000; Fong and Stacey 2003; Jones et al. 2008; Moniz et al. 2014), although other processes such as shear-flow dispersion in unbounded flows may be the dominant dispersion mechanism (Young et al., 1982; Garrett, 2006; Moniz et al., 2014). It is intriquing that the "four-thirds" law applied to the longitudinal dispersion in shallow estuaries. Perhaps such a power law applies to a wider range of flows than assumed in the original theory. We must also point out that the data points in Figure 2.17 display a wide scatter and reflect large spring-neap differences in K_x.

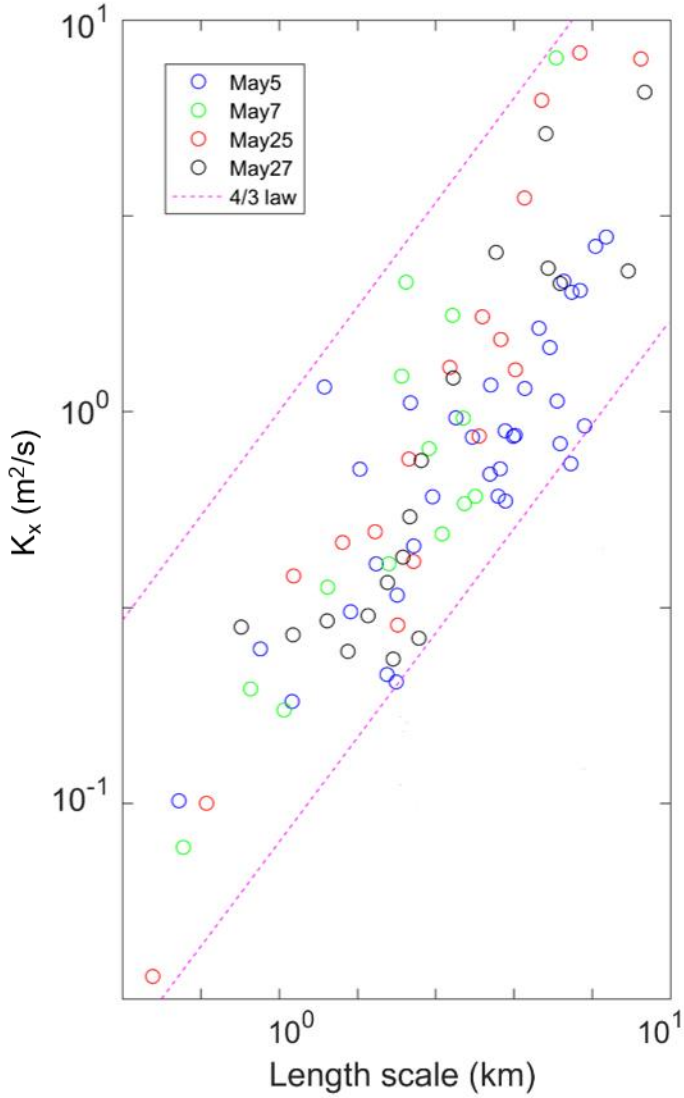

Figure 2.17 Longitudinal diffusivity versus the length scale for four dye experiments. The dashed magenta lines indicate the slope of 4/3.

§2.5 Conclusion

The four dye release experiments in the James River estuary showed that the longitudinal dispersion rate had large flood-ebb and spring-neap differences. The numerical model reproduced the observed dispersion and provided an explanation in terms of the vertical shear dispersion. Tidal straining enhances vertical current shear on ebb tides and promotes longitudinal dispersion. In contrast, tidal straining reduces vertical shear on flood tides and increases vertical mixing, thus suppressing longitudinal dispersion. The large differences in the dispersion rate between spring and neap tides can also be interpreted in term of the differences in the vertical shear dispersion. Due to strong spring mixing, a dye patch quickly extends from the bottom to the surface, exposing to the full vertical shear in the water column and leading to strong longitudinal dispersion. In contrast most of the dye patch is limited to bottom few meters during neap tides. Although weak vertical mixing facilitates longitudinal dispersion, the vertical shear across the thin dye patch is much weaker, leading to weak longitudinal dispersion during neap tides.

The numerical model allows us to investigate dye dispersion at large times. The second moment of the dye patch in the along-channel direction increases with time at a power of between 2 and 3. The longitudinal dispersion rate varies as the four-third power

of the dye patch size, indicating scale-dependent diffusion. This is consistent with the "four-thirds" law describing relative dispersion in turbulent flows (Richardson, 1926; Batchelor, 1952) and has been found to describe oceanic dispersion in a wide range of flow conditions (Okubo 1971).

Acknowledgements: We are grateful to NSF (OCE-0825826, OCE-0825833, OCE-0825876) for the financial support.

CHAPTER 3. COMPARATIVE STUDY OF SALT FLUXES IN PARTIALLY MIXED AND WELL MIXED ESTUARIES

Abstract

Salt dispersion and transport are examined in a comparative numerical modeling study between the partially-mixed Chesapeake Bay and the well-mixed Delaware Bay. To investigate how different physical mechanisms drive the salt transport into the estuaries, the longitudinal salt fluxes are decomposed using the Eulerian and quasi-Lagrangian methods. Under the Eulerian framework, the salt flux is decomposed into three parts: an advective term F0 associated with the barotropic forcing, a steady shear dispersion term Fe associated with the estuarine exchange flow, and a tidal oscillatory salt flux Ft. In both estuaries, F0 fluctuates with a main period of 2 days and is dominant over Fe and Ft in the temporal variation of total salt flux. In Chesapeake Bay, the steady shear dispersion is the dominant mechanism and the tidal oscillatory salt flux Ft is small. In Delaware Bay, the steady shear dispersion and tidal dispersion are comparable. The along-channel variation of Ft is mainly due to changes of the phase difference between the tidal current and salinity. Isohaline analysis using the quasi-Lagrangian methodology yields a new interpretation of the estuarine exchange flows and describes the evolution path of different salinity classes.

This chapter is organized in the following way. Section 3.1 reviews recent studies on the salt flux analysis as a motivation and provides an outline for this research work. Section 3.2 describes the methods including FVCOM model configuration, validation and two salt flux decomposition methods. Section 3.3 provides the results. Section 3.4 discusses the factors controlling the fluctuation of F0 term and the along-channel

variation of Ft term, and interprets the isohaline analysis results. Section 3.5 summarizes the conclusions.

§3.1 Introduction

Salinity is a critical factor in understanding physical and biogeochemical processes in the estuaries. Many climatic and oceanic factors, including streamflows and tidal currents, have important influences on the salinity of the estuaries. The flux of salt into the estuaries may be influenced by processes such as steady shear dispersion and tidal oscillation; however, the estuarine response to these factors may be quite different in different types of estuaries.

Hanson and Rattray (1965) firstly provide the solution of combined equations for estuarine dynamics with simply assumption about the strength and structure of tidal dispersion. Many studies have applied the Eulerian method of subtidal salt transport decomposition for estuaries. First, the salt fluxes are simply separated by their directions: the downstream salt transport due to river outflow and atmospheric forcing, the upstream salt transport due to the estuarine exchange flow and tidal dispersive mechanisms, respectively (Pritchard 1954; MacCready 2004, 2007; MacCready and Geyer 2010). Then the upstream salt transport can be decomposed into two parts: the subtidal salt transport due to spatial correlation between tidally averaged mean velocity, known as estuarine exchange flow obtained by the Eulerian mean method (Lerczak et al. 2006), and subtidal

salinity, and the subtidal salt transport due to correlation between tidal variations in velocity and salinity (Fischer 1976; Bowen and Geyer 2003).

The observation study in Hudson River by Lerczak et al. (2006) found that steady shear dispersion is the dominant mechanism in driving the upstream salt flux with the maximum strength during neap tide and minimum strength during spring tide. They also indicate the variation in the advective salt flux has a period of 3-5 days resulting from the variation in river discharge. However, their result is limited to a single section without indication on the along-channel direction. The study in a lagoon by Jia and Li (2012) shows the wind's effect on the advective salt flux. They also find that tidal pumping is active in the narrow outlet while steady shear dispersion is dominant in a section inside the lagoon. Their findings in different sections indicates the variation of salt fluxes components in the along-channel direction and their mechanism may vary. Aristizabal and Chant (2013) applied an idealized model with constant river discharge to study the salt fluxes variation in one neap-spring tidal cycle in DB. They suggest that the lateral flows bring velocity and salinity out of quadrature and induce a large tidal oscillatory salt flux. The assumption of constant river discharge in the model simplifies their analysis, but it may not predict the correct magnitude of the advective salt flux or the relative importance among three salt flux components. Again Aristizabal and Chant (2015) studied the salt flux across a mid-bay section in Delaware Bay using the observation data and found that the advective salt flux dominates over the steady shear dispersion and tidal oscillatory salt flux, and its fluctuation is driven mainly by wind. The along-channel variation of salt flux is not explained.

The tidal oscillatory salt flux could play an important role in driving the upstream salt flux. Many attempts have been made to explain various mechanisms behind the tidal oscillatory salt flux. The most common mechanisms include the jet–sink theory (Stommel and Former, 1952; Jia and Li, 2012; Chen et al., 2012), tidal trapping (Okubo, 1973), tidal shear dispersion (Taylor, 1954; Bowden 1965; Fischer, 1973), chaotic stirring (Zimmerman, 1986) and hydraulic response (Wang et al, 2016). A recent study in Hudson River by Wang et al (2016) found that tidal oscillatory salt flux appears to be a non-dispersive. They concluded that the tidal oscillatory salt transport is mainly due to the hydraulic response of the halocline to the longitudinal variation of topography during neap tide and is thus the advective transport of salt. All these studies reveal the uncertainties of the mechanisms driving the tidal oscillatory salt flux and its along-channel variation.

There are essentially two ways to observe the physical properties in flow field: Eulerian method is a way of looking at fluid motion that focuses on specific locations in the space through which the fluid flows as time passes. This is a most common way to observe. For example, a person stands at the river bank and watches the river flows, which is an Eulerian way. While the Lagrange method is a way of looking at fluid motion where the observer follows an individual fluid parcel as it moves through space and time. This can be visualized as sitting in a boat and drifting down a river. Most of oceanic numerical models, such as ROMS and FVCOM, use the Eulerian description of equations. Due to the nature of the Eulerian framework, the physical properties may vary

in three dimensional space and thus the diffusive schemes need to be be introduced in three spatial directions to describe the diffusion processes. However, the diffusion processes are not well studies or accurately predicted. Contrarily, Lagrange framework can treat the physical properties as one dimension. In this way, we can find the surfaces where the value of physical properties does not change and thus the movement can be exactly described without introducing the diffusive schemes. The advantages of Eulerian and Lagrange methods inspire us to apply both to better understand the dispersion processes of salt.

Under the Eulerian framework, the along channel salt flux could be decomposed into an advective term F0 associated with the barotropic forcing such as river flow and wind-induced sea level difference, a steady shear dispersion Fe associated with the estuarine exchange flow, and a tidal oscillatory salt flux Ft, which is due to the correlation between tidal variations in velocity and salinity. In different types of estuaries, the salinity field could be dominated by the advective salt flux (Aristizabal and Chant, 2015) or the steady shear dispersion (Lerczak et al., 2006) or various tidal pumping mechanisms (Jia and Li, 2012; Chen et al., 2012).

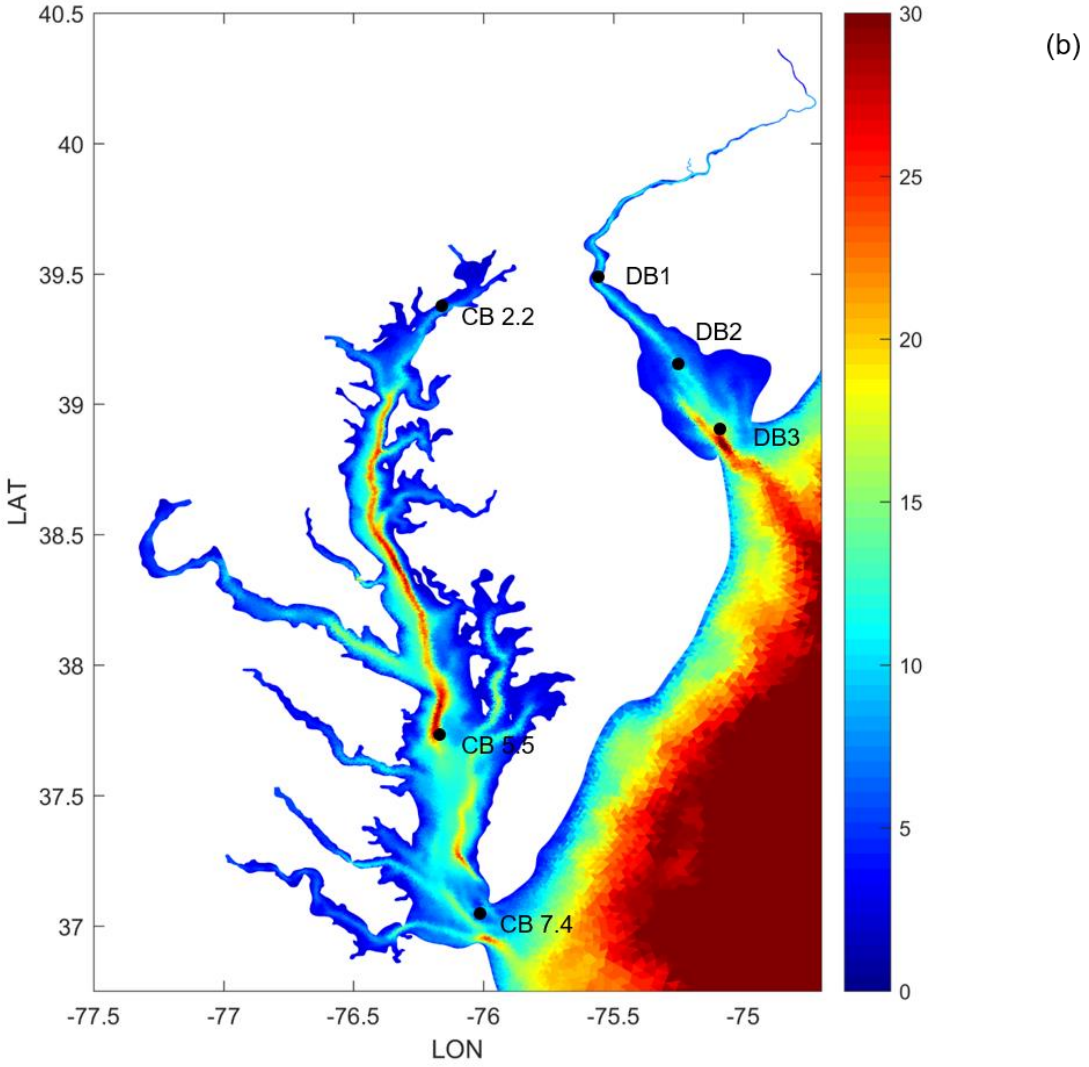

Figure 3.1 Bathymetry of Chesapeake Bay, Delaware Bay and their adjacent coastal area. Depths are in meters. Black dots are the locations of CBP stations and Delaware Bay survey sites. DB1 represent the upper bay station, DB2 mid-bay station and DB3 lower bay station.

To study the mechanisms driving the salt fluxes in different estuaries, we have chosen two adjacent but contrasting estuaries in the Mid-Atlantic Region of the U.S.,

namely the partially mixed Chesapeake Bay and the well-mixed Delaware Bay (Fig. 3.1). By conducting this comparative study of salt fluxes for the Chesapeake and Delaware Bays, we aim to discern the key processes responsible for driving salt in/out of the bays through the Eulerian salt flux decomposition (Lerczak, 2006; Aristizable and Chant, 2013).

Physical properties	Chesapeake Bay	Delaware Bay
Averaged River Discharge (m^3/s)	4000	1300
Averaged Tidal Amplitude (m/s)	0.5	0.88
Length (km)	325	180
Volume (m^3)	6.8×10^{10}	1.95×10^{10}
Shape	relative constant channel width; Lots of branches/tributes	Channel widens significantly near the mouth
Averaged Salinity (psu)	16	21
Stratification	Partially mixed	Well mixed

Table 3.1 Comparison of physical properties of Chesapeake Bay and Delaware Bay

Table 3.1 shows the comparison of physical properties between Chesapeake and Delaware Bays. The Chesapeake Bay estuary has a long main channel interacting with a number of tributaries arrayed along its axis (Fig. 3.1). The length of the main channel is about 320 km from the mouth of the Susquehanna River at Havre de Grace, Maryland, to the seaward end at Cape Charles and Cape Henry, Virginia. The bay is generally shallow, with a mean water depth of 6.5 m. However, a deep paleo-channel running in the north-south direction, with a maximum depth of 40 m, dominates the bathymetry in the middle reaches of the main bay. River discharge into the bay is from eight major tributaries

including Susquehanna, Patapsco, Patuxent, Potomac, Rappahannock, York, James and Choptank. The Susquehanna River at the northern extreme of the bay provides approximately one half of the total freshwater input (Zhong and Li, 2006).

The Delaware Estuary is located to the northeast of the Chesapeake Bay (Fig. 3.1). The Delaware River is its main source of freshwater discharge with an annual-mean river input of 330 m^3s^{-1} (Aristizabal and Chant, 2015). The length of the main channel is much shorter than the Chesapeake Bay. The mean depth of the estuary is 8 m and the maximum depth is about 45 m. The mouth of the bay is approximately 18-kmwide, but the estuary widens to a maximum of about 40 km at a distance of around 30 km for its mouth. Further upstream, the estuary narrows and forms a funnel shape.

What mechanisms are important in driving the downstream and upstream salt fluxes in the Chesapeake Bay and Delaware Bay has not been fully answered. It is also of great interest to examine two types of estuaries in one model with same external forcings. There is seldom a study on salt flux for Chesapeake Bay. Li and Li (2011) studied the up-stream and down-stream wind's role in modulating salt flux due to steady shear dispersion. Aristizabal and Chant (2013) applied an idealized model with constant river discharge to study the salt fluxes variation over a neap-spring tidal cycle in Delaware Bay. This assumption of constant river discharge could not realistically reveal its determinative role in modulating the salt flux at seasonal or even storm event time scales. In another study Aristizabal and Chant (2015) studied the salt flux in Delaware Bay using the observational data, but their results were limited to one cross section and lasted only about one month.

Many questions will be addressed in this study. How do the river flows and salt fluxes through the estuarine mouths affect the seasonal evolution of salinity distribution in the two bays? Salt flux can be decomposed into tidal pumping, subtidal shear dispersion and subtidal barotropic components by Eulerian method. What physical processes are controlling these salt fluxes components? What are the relative importance of tidal pumping and shear-dispersion mechanisms in supplying salt to the two estuaries? Wind-driven flows have been shown to be an important mechanism for the estuary-shelf volume exchange at the mouth of some estuaries (e.g. Valle-Levinson et al., 2001). Will the local wind or remote wind contribute to the wind-driven flows and thus influence the salt flux into the bays? What are the differences in salt flux mechanisms between the bays?

§3.2 Methods

In this study, we develop a realistic high-resolution numerical model to investigate the spatial and temporal variations of salt fluxes in two bays. Then we apply the commonly used Eulerian decomposition method and the newly introduced isohaline decomposition method to study the salt fluxes and provide new insights on the differences of salt transport processes in the two bays.

Finite-Volume Community Ocean Model (FVCOM) (Chen et al. 2006, 2007, 2011) is a state-of-the-art regional ocean model that has found wide ranging applications, especially in coastal water areas. FVCOM solves the governing equations in unstructured

triangular volumes with a second-order accurate discrete flux scheme, resulting in more accurate representations of mass, momentum, heat, and salinity conservation (Chen et al. 2011). This model provides fine resolutions in Chesapeake Bay and Delaware Bay to examine the temporal variation of salinity and velocity field in hours and spatial resolutions in meters.

We have chosen the unstructured-grid Finite Volume Coastal Ocean Model (FVCOM) to develop a coupled estuary-shelf model for Chesapeake Bay, Delaware Bay, Mid-Atlantic Bight, and South Atlantic Bight. Compared with another popular oceanic numerical model – Regional Ocean Modeling System (ROMS), FVCOM has the advantage of more accurately following the complicated coastlines by using unstructured triangle grids. Huang et al. (2008) demonstrated that FVCOM provides overall a second-order spatial accuracy for the vertically averaged equations (i.e., external mode), and with increasing grid resolution the model-computed solutions show a fast convergence toward the analytic solutions regardless of the particular triangulation method. FVCOM has taken advantage of the new development in computational fluid dynamics in resolving flow problems containing discontinuities. Thus we selected this model to develop fine resolution grids and computation in this study. It exactly resolves small-scale flows inside the two estuaries while simulating the Gulf Stream and coastal currents on the shelf. Our development of this model is based on the recent work by Peng Cheng, Andrew Ross and collaborators, who constructed the grid and nested this regional FVCOM within the global Hybrid Coordinate Ocean Model (HYCOM) and conducted a hindcast simulation from 2002 to 2011 (Ross et al., 2017; Lee et al., 2017; Zhang et al. 2017). The model

results are in reasonable agreement with the observational data of sea level height collected in Chesapeake Bay and Delaware Bay but will require a more accurate prediction of current and salinity field in both bays. Thus we have further configured and validated the model as follows.

3.2.1 Development of FVCOM model for Chesapeake and Delaware Bays

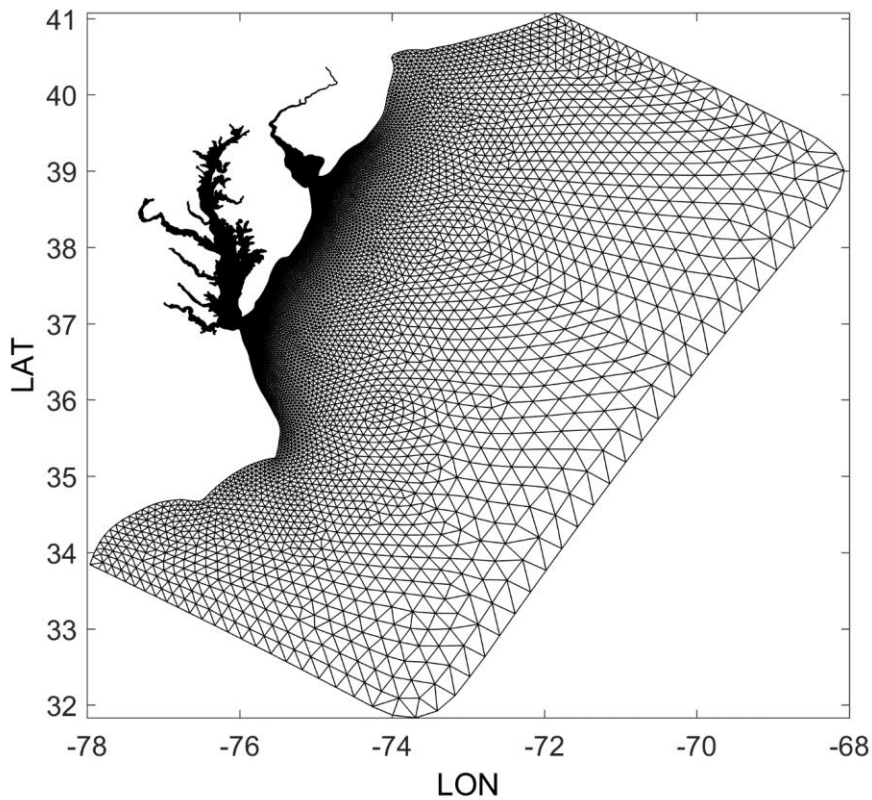

Figure 3.2 FVCOM Model domain and grids

The model domain (Fig. 3.2) covers a wide shelf area with grid sizes ranging from 0.4 to 20.2 km. It is aligned in a direction roughly parallel to the U.S. East Coast, and has 70,000 triangular grids and 40 sigma layers in the vertical direction. The eastern

boundary is placed several hundred kilometers from the coast and lies in the deep ocean. The southern and northern boundaries are roughly perpendicular to the coast and located at 34° and 41° N, respectively. The Chesapeake & Delaware Canal is not included since the transport volume and salinity gradient is small through it. The unstructured mesh allows a large model domain with high spatial resolution in the Chesapeake and Delaware Bays (about 0.18 km). The model has been set up with atmospheric forcing, offshore tidal sea level and river discharge. It has been previously validated using 10 years' outputs (2002-2011) and gives the good predictions in salinity, tidal velocity, water level and temperature.

Improvement has been made on the salinity prediction. It was found that the previously model bathymetry may have limited the deep-channel salt intrusion due to the abrupt change of depth among nearby model grids. Thus we resampled and smoothed the model bathymetry to ensure that the landward salinity transport is not restricted. The k-kl (modified Mellor–Yamada) turbulence closure model was used to calculate vertical viscosity and diffusivity (Warner et al. 2005b; Li et al. 2005). The background diffusivity and viscosity are set at 10^{-6} m^2s^{-1}. This study analyzes the model results in 2011.

The model gives a reasonable prediction of the tidal heights and surface and bottom salinity in the two bays. Fig. 3.3 show a time-series comparison between the observed and modeled sea levels at five tidal gauge stations across Chesapeake Bay and Delaware Bay in year 2011. These stations are selected to cover the entire bay region. The model generally matches the tidal variation in observation. However, it

underestimates the positive sea level peaks in three Chesapeake Bay stations covering upper, middle and lower bay areas and Lowes station in Delaware Bay. It appears that the modeled sea level is larger than the observed one at Ready Point station in Delaware Bay. Following Warner et al., (2005b) and Li and Zhong (2009), the model prediction skill for sea level ranges from 0.8 to 0.91 among the stations. Overall, the prediction in sea level is reasonable.

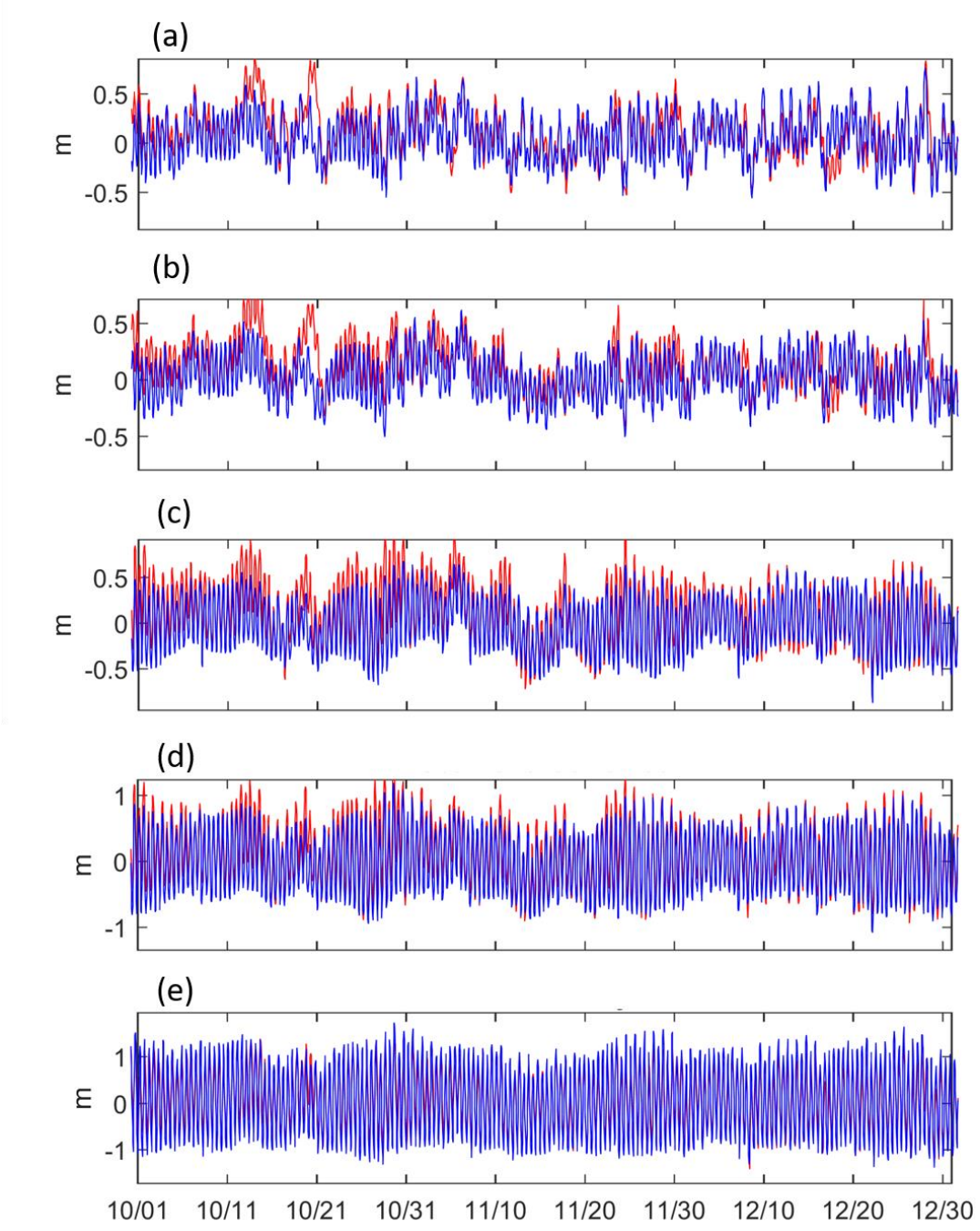

Figure 3.3 Time series of observed (red) and modeled (blue) sea level at tidal gauge station Baltimore (a), Soloman Island (b), CBBT (c) in Chesapeake Bay and Lowes (d), and Reedy Point (e) in Delaware Bay.

Fig. 3.4 shows the comparisons of both surface and bottom salinity in three Chesapeake Bay Program (CBP) stations located at upper, middle and lower bay. It appears that almost all of the observation data points fall on the modeled lines. The RMSE for all comparison in these three stations is 1.2. FVCOM model reasonably predicts both the surface and bottom salinity in Chesapeake Bay. The surface salinity in Delaware Bay is compared with observation data in three stations (Fig. 3.5). The upper bay station has the latitude and longitude of (39.455, -75.56); the mid-bay station is at (39.1731944, -75.2812778) while the lower bay station is at (38.9277778, -75.1) (Fig. 3.1). The RMSE for the comparison in Delaware Bay is 0.9. The observation data is limited to the surface of water and only available from April through October. It shows that most of observed salinity data points are within the range of modeled salinity, which indicates that the modeled salinity is consistent with the observed data. Thus the FVCOM model gives a reasonable reproduction of surface salinity in Delaware Bay in 2011. Due to lack of observation data, the bottom salinity is not compared in Delaware Bay.

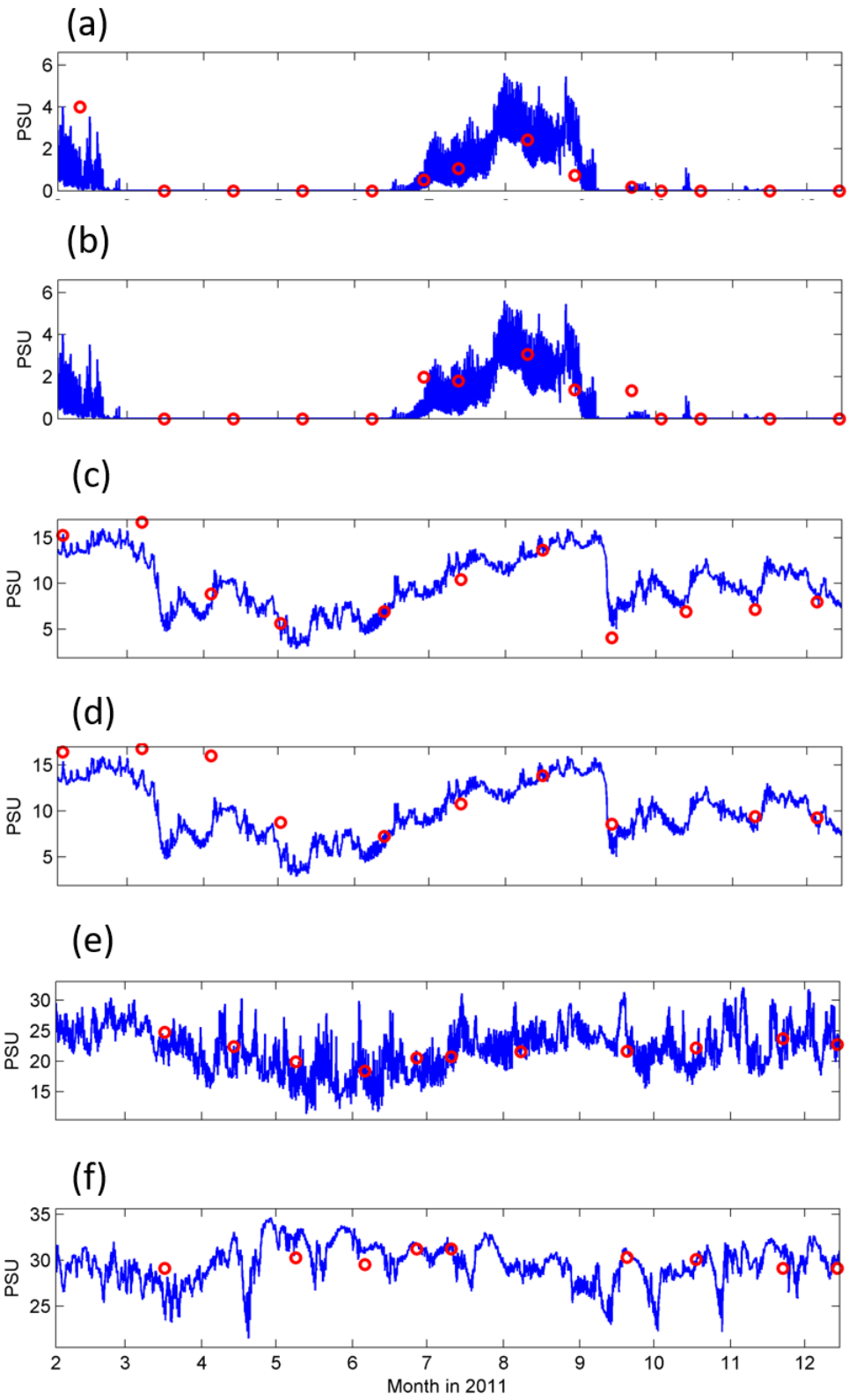
(a)
PSU
6
4
2
0
(b)
PSU
6
4
2
0
(c)
PSU
15
10
5
(d)
PSU
15
10
5
(e)
PSU
30
25
20
15
(f)
PSU
35
30
25
2
3
4
5
6
7
8
9
10
11
12
Month in 2011

Figure 3.4 Comparisons of surface and bottom salinity in three Chesapeake Bay Program (CBP) stations CB2.2 , CB5.5 and CB7.4 located at upper (a, b), middle (c, d) and lower (e, f) bay (See Fig. 3.1). Red dots represents observation data and blue line represents the model data.

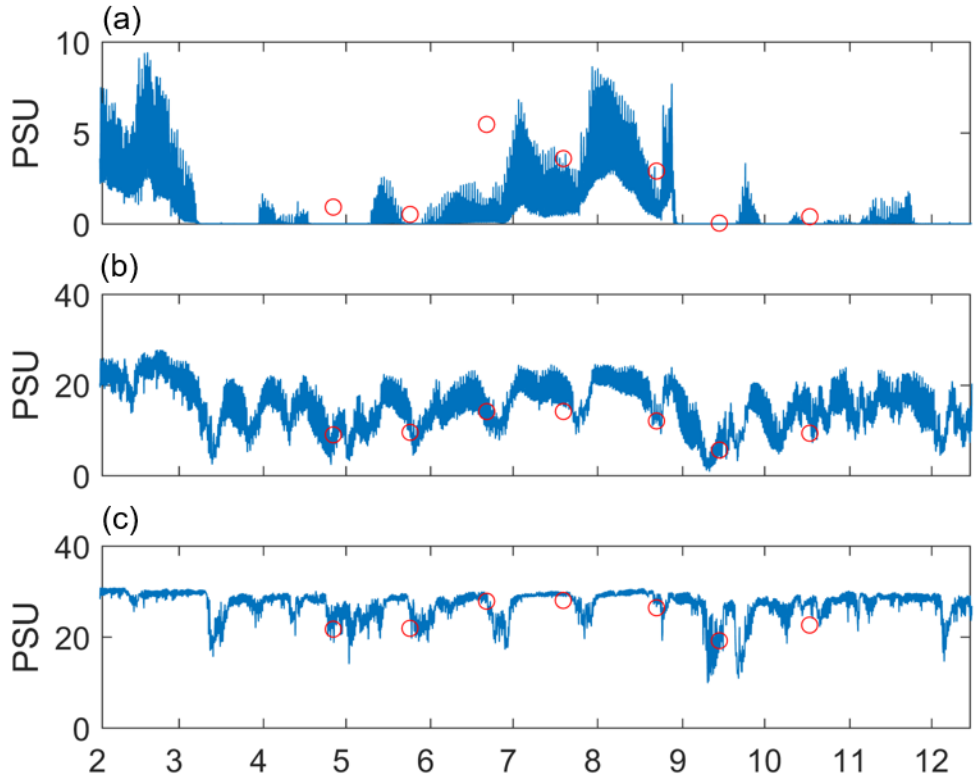

Figure 3.5 Observation-model comparison of surface salinity in upper (a), middle (b) and lower Delaware Bay. Red dots represent observation data and blue lines represent the model data.

3.2.2 Eulerian Decomposition of Salt Fluxes

To examine what processes are driving salt in/out of the bays, we have conducted the Eulerian salt flux decomposition (Lerczak, 2006; Aristizable and Chant, 2013). The subtidal salt flux F through a section:

$$F = < \int usdA > \tag{3.1}$$

where u is velocity, s is salinity and A is the area of section. The angle brackets indicate a subtidal low-pass filter. The tidally averaged area A_0 is defined by

$$A_0 \equiv < \int dA > \tag{3.2}$$

$$dA_0 \equiv < dA_0 > \tag{3.3}$$

The sectionally and tidally averaged velocity u_0 and salinity s_0:

$$u_0 \equiv \frac{<\int udA>}{A_0} \tag{3.4}$$

$$s_0 \equiv \frac{<\int sdA>}{A_0} \tag{3.5}$$

The sectionally varying tidally averaged velocity u_1 and s_1:

$$u_1 \equiv \frac{<udA>}{A_0} - u_0 \tag{3.6}$$

$$s_1 \equiv \frac{<sdA>}{A_0} - s_0 \tag{3.7}$$

The spatially and tidally varying velocity u_2 and s_2:

$$u_2 \equiv u - u_0 - u_1 \qquad s_2 \equiv s - s_0 - s_1 \tag{3.8}$$

The subtidal salt flux may then be decomposed into three parts (river, exchange, and tidal) as

$$F = < \int (u_0 + u_1 + u_2)(s_0 + s_1 + s_2) dA >$$

$$= u_0 s_0 A_0 + u_1 s_1 A_1 + u_2 s_2 A_2 \quad (3.9)$$

The cross terms are approximately zero because they are largely uncorrelated by definition (MacCready, 2011). We have compared the total salt flux and the sum of three terms in several cross sections in two bays. They are nearly equal and thus prove the accuracy of this approximation.

Generally, F0 removes salt from the estuary, Fe and Ft, due to the exchange flow and tidal correlations, add salt. F0 is considered as the subtidal salt flux driven by river flow, but it also could include the subtidal salt flux driven by the wind forcing (Lerczak et al, 2006).

3.2.3 Isohaline Decomposition of Salt Fluxes

An alternate way to look at subtidal estuarine salt flux is to average the transport as a function of salinity instead of as a function of spatial position within the section. Adopting salinity as a coordinate allows us to better keep track of the flux of specific types of water (McCready 2011). One advantage of the isohaline analysis is that its terms map directly into an exact version of the Knudsen relation. The volume flux of the landward transport can be calculated precisely using the isohaline framework.

The tidally averaged volume flux of water with salinity greater than s is defined as

$$Q(s) \equiv < \int_{A_s} u dA > \tag{3.10}$$

where A_s is the tidally varying portion of the cross section with salinity greater than s. The volume flux in a specific salinity class can be evaluated as

$$-\frac{\partial Q}{\partial s} = -\lim_{\delta s \to 0} \frac{Q\left(s+\frac{\delta s}{2}\right) - Q\left(s-\frac{\delta s}{2}\right)}{\delta s} \tag{3.11}$$

The Total Exchange Flow (TEF) is defined as incoming volume Q_{in} and outgoing volume Q_{out}

$$Q_{in} \equiv \int \frac{-\partial Q}{\partial s}|_{in} ds \quad (3.12) \qquad Q_{out} \equiv \int \frac{-\partial Q}{\partial s}|_{out} ds \quad (3.13)$$

The salt flux due to TEF positive (incoming) salt flux F_{in} and negative (outgoing) salt flux F_{out} is given by

$$F_{in} \equiv \int s \frac{-\partial Q}{\partial s}|_{in} ds \quad (3.14) \qquad F_{out} \equiv \int s \frac{-\partial Q}{\partial s}|_{out} ds \quad (3.15)$$

The flux-weighted salinities s_{in} and s_{out} that characterize the inflow and outflow are given by

$$s_{in} \equiv \frac{F_{in}}{Q_{in}} \quad (3.16) \qquad s_{out} \equiv \frac{F_{out}}{Q_{out}} \quad (3.17)$$

In terms of volume conservation, it shows as

$$Q_{out} + Q_{in} = -Q_R \tag{3.18}$$

where Q_R represents the volume of river discharge.

We have examined that the isohaline method gives the consistent results as the Eulerian method. By comparing 11 months' time series of net salt flux across the near-mouth section in Chesapeake Bay calculated with two methods, it demonstrates they are equally accurate in calculating the salt fluxes with trivial difference at the peak due to filtering error. The same results are also found in Delaware Bay.

§3.3 Results

3.3.1 Neap-spring variation of subtidal velocity and salinity field

In order to show the subtidal longitudinal structure of the bays' salinity, the along-channel section is selected with the grid points of maximum depth in the cross-channel direction. The main circulation in Chesapeake Bay has two layers in the vertical direction (Fig. 3.6). The surface layer moves the salt seaward while the bottom layer transports salt landward in the bottom layer (Carter and Pritchard, 1988). There are certain neap-spring variations in the strength of main circulation with intensified circulation during the neap tide and weakened circulation during the spring tide. The subtidal current speed reaches up to 0.3 m/s. The vertical salinity difference varies from 2 psu during springs to 8 psu during neaps. And the length of salt intrusion reaches up to 270 km from the mouth (Fig. 3.7). A cross section in mid Chesapeake Bay is selected to show the salinity structure. The Chesapeake Bay is relatively wide and the salinity in the eastern shore is generally higher than the western shore due to the Coriolis effect (Fig. 3.8). The neap-spring variation of stratification is significant.

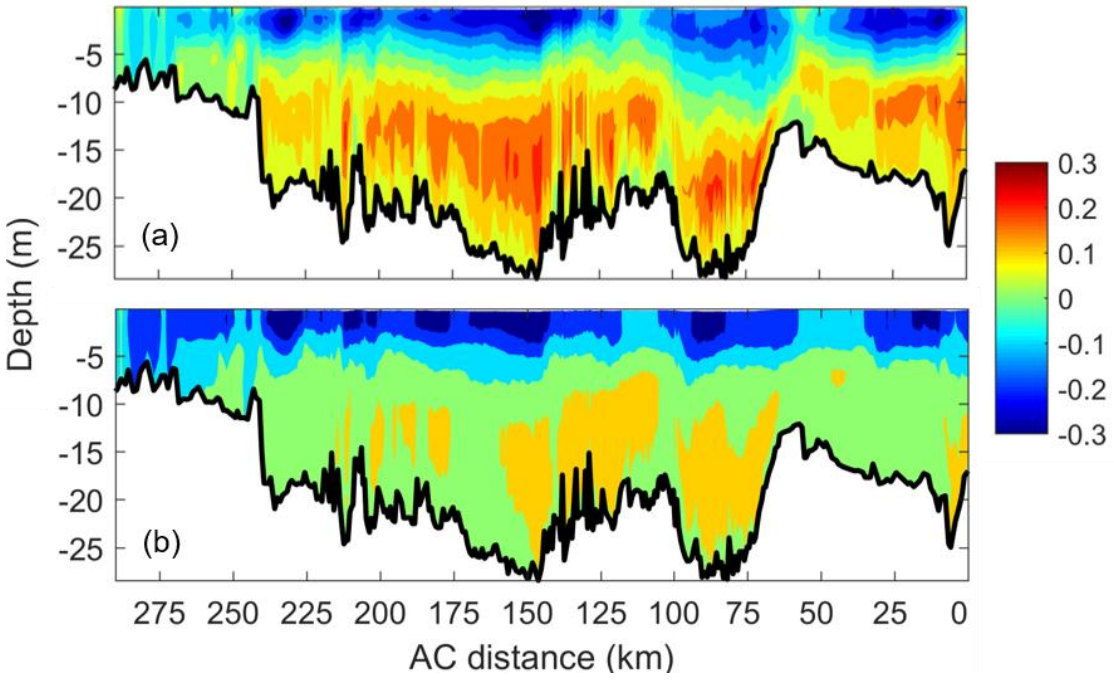

Figure 3.6 Along-channel sections of subtidal along-channel velocity during neap tide (a) and spring tide (b) in Chesapeake Bay in December, 2011. Low-pass filtered velocity is shown.

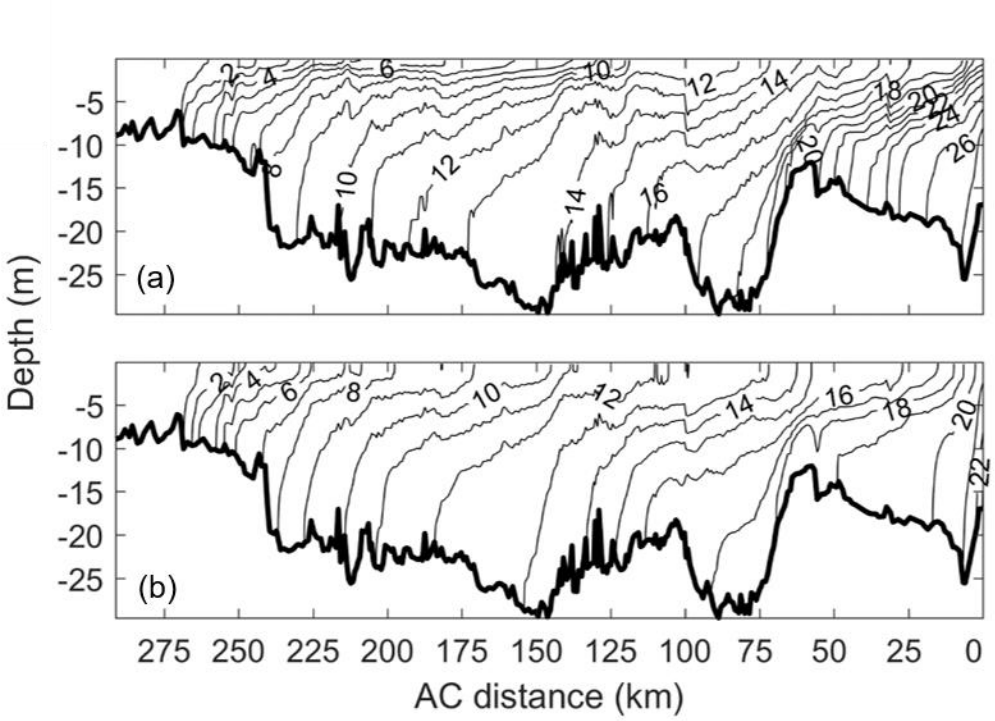

Figure 3.7 Along-channel sections of averaged salinity field during neap (a) and spring (b) tide in Chesapeake Bay in December, 2011.

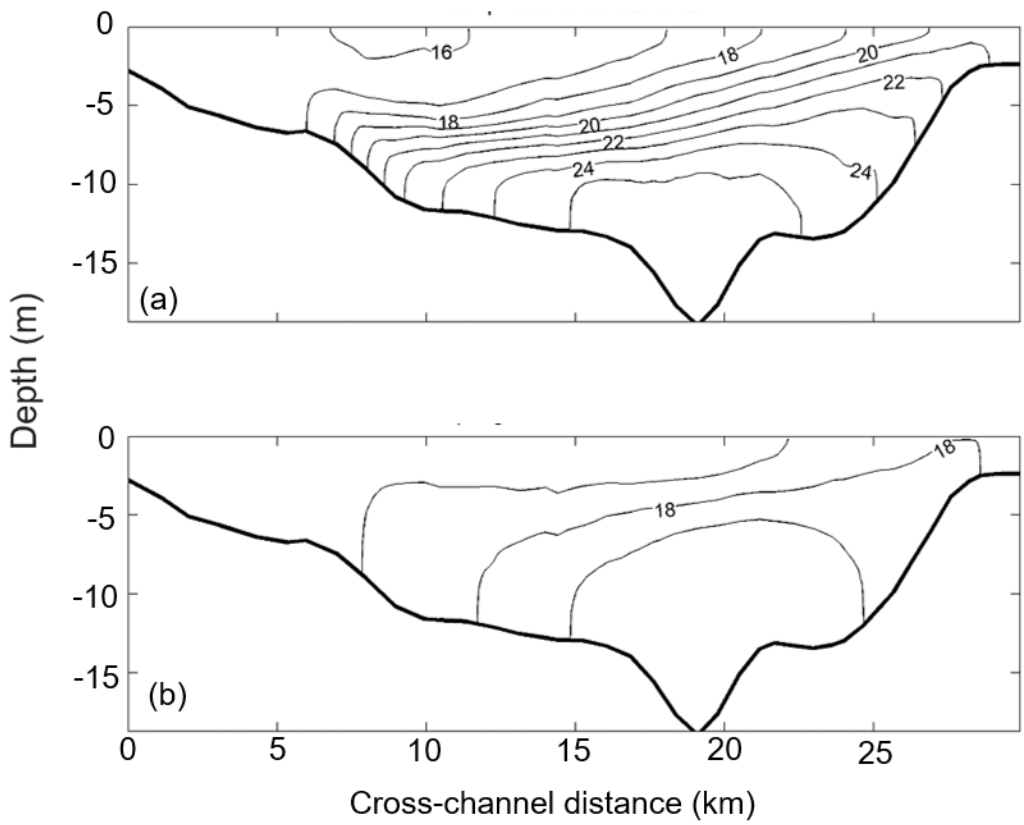

Figure 3.8 Cross-channel section of averaged salinity field during neap (a) and spring (b) tide in lower-Chesapeake Bay (Facing into the estuary) in December, 2011.

The residual current in Delaware Bay shows a vertical two-layer structure but is relatively weak (Fig. 3.9). The along-channel section is built up with the grid points of maximum depth in the cross-channel direction. Compared to Chesapeake Bay, the bottom layer residual current is significantly weaker and could potentially limit the salt intrusion. Consistent with the findings by Garvine et al. (1992), our model shows that salt intrusion in Delaware Bay extends up to 100 km through the lower half of the estuary (Fig. 3.10). Even though previous studies have identified Delaware Bay as a well-mixed estuary (Beardsley and Boicourt 1981; Garvine et al. 1992), both the observations (Aristizabal

and Chant, 2013) and our model simulations show that this system can present a vertical stratification as high as 12 psu in the main channel but is consistently well mixed on the flanks (Fig. 3.11).

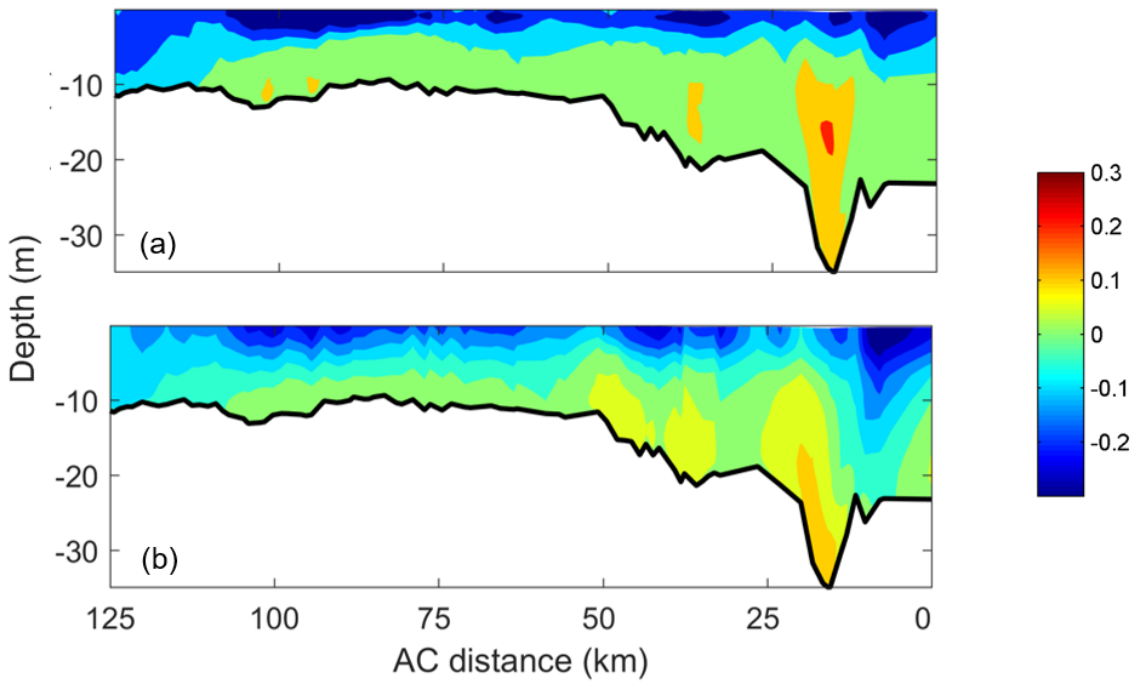

Figure 3.9 Along-channel sections of the subtidal velocity in Delaware Bay during the neap (a) and spring (b) tides in December, 2011. Low-pass filtered velocity is shown.

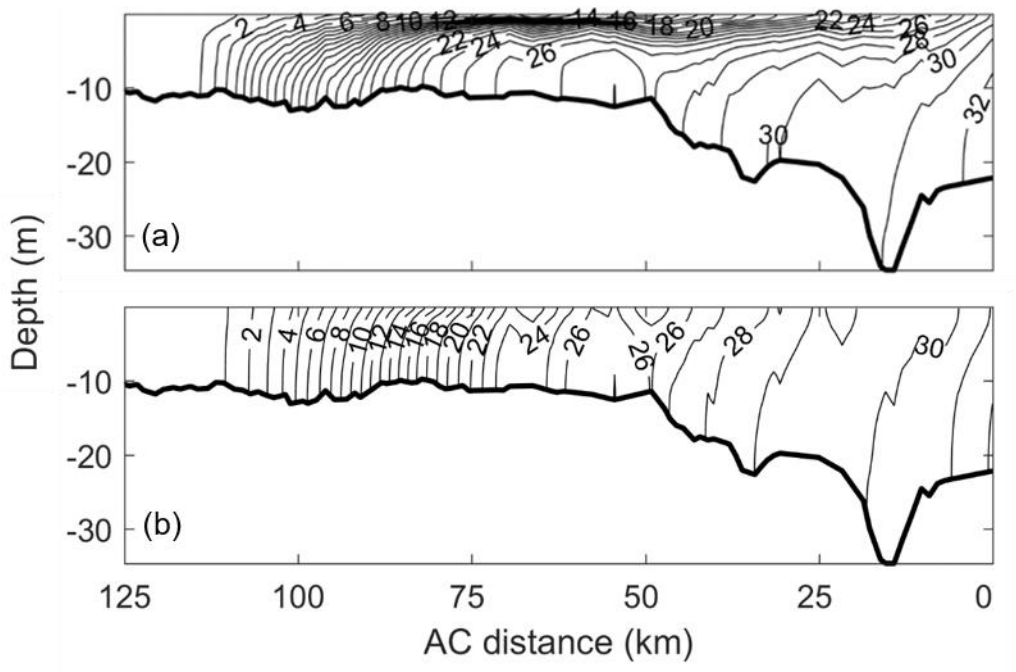

Figure 3.10 Along-channel sections of averaged salinity field during neap tide (a) and spring tide (b) in Delaware Bay in December, 2011.

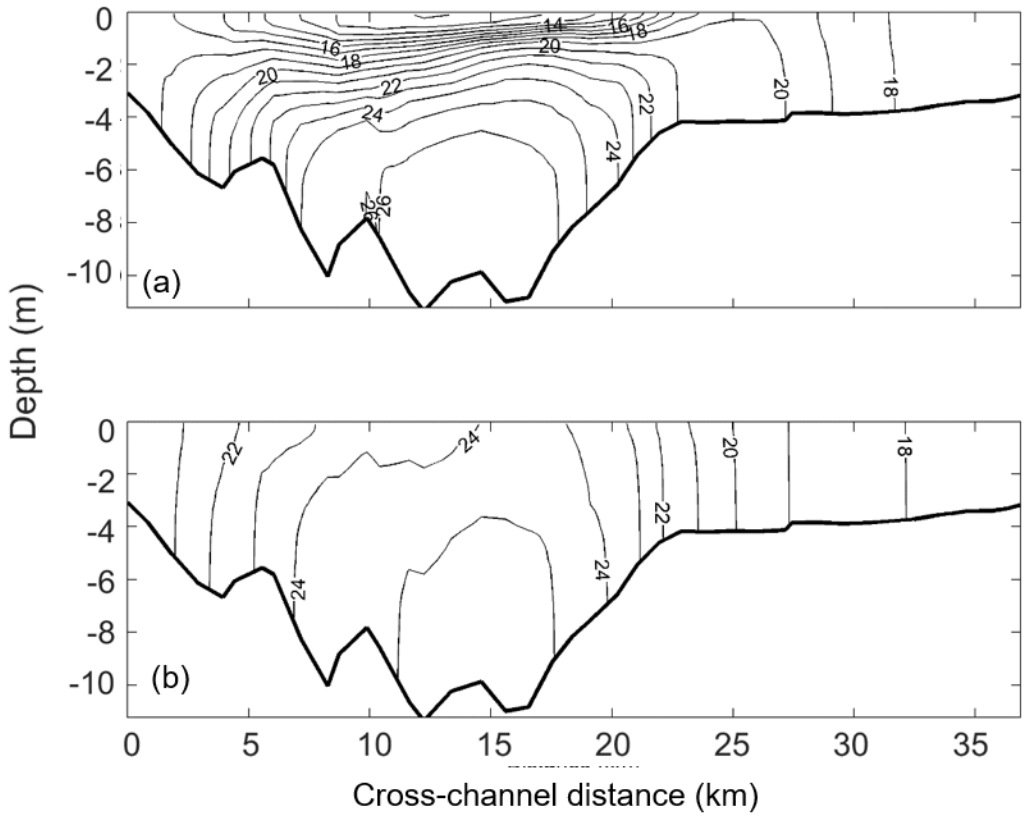

Figure 3.11 Cross-channel sections of salinity field during neap (a) and spring (b) tide in lower Delaware Bay in December, 2011.

3.3.2 Salt budget and salt balance

As shown in the above figures, there are large differences in the salinity distribution and stratification between Chesapeake and Delaware Bays. To understand what drives these differences, we now investigate the salt budget and salt balance for the two estuaries. The river discharges have a well-defined seasonal cycle: high flows during spring and low flows during summer. Several storm and hurricane events were recorded in 2011 and affected the river runoff during the fall.

We calculate the total salt content $Ms=\int S dV$ in the two bays where S is salinity and V is the volume. At the same time, the salt content is calculated using another method: the initial salt content plus the integrated salt flux that is the accumulated salt flux from the initial to the certain time. Then we plot their temporal evolution together in Fig. 3.12. Both figures show that the integrated salt flux matches with the variation of salt contents in two bays, which proves the accuracy of the salt flux calculation. The total salt content in Chesapeake Bay is around 1.2×10^{12} psu m^3 while it in Delaware Bay is around 3×10^{11} psu m^3. Seasonal variation of salt content is similar for the two estuaries. Because of large river discharges, the salt content Ms decreased rapidly during spring and reached a minimum in May. When river discharge was low, Ms experienced substantial increases during the summer months and reached a maximum in the beginning of September. Due to the presence of Hurricane Irene and Tropical Storm Lee, the river discharge jumped in September. This led to the freshening in both bays and Ms reached ae minimum in mid-September for both bays. The salt content stayed constant during the last few months of 2011. For the year of 2011, the salt content in Chesapeake Bay was about the same between the beginning and end of the year, even though it experienced large seasonal variations. However, the Delaware Bay appeared to have lost salt during the same time period and did not recover to the same condition as the beginning of 2011. This may be due to the unusually large river discharge into Delaware River during September, and it may take more than three months to recover to the regular state. Monthly averaged salt flux is shown in Fig. 3.12 c and f. Positive salt transport was into both bays during the

summer months (May, June, July and August) while negative salt flux was found during the winter months (February, March and April).

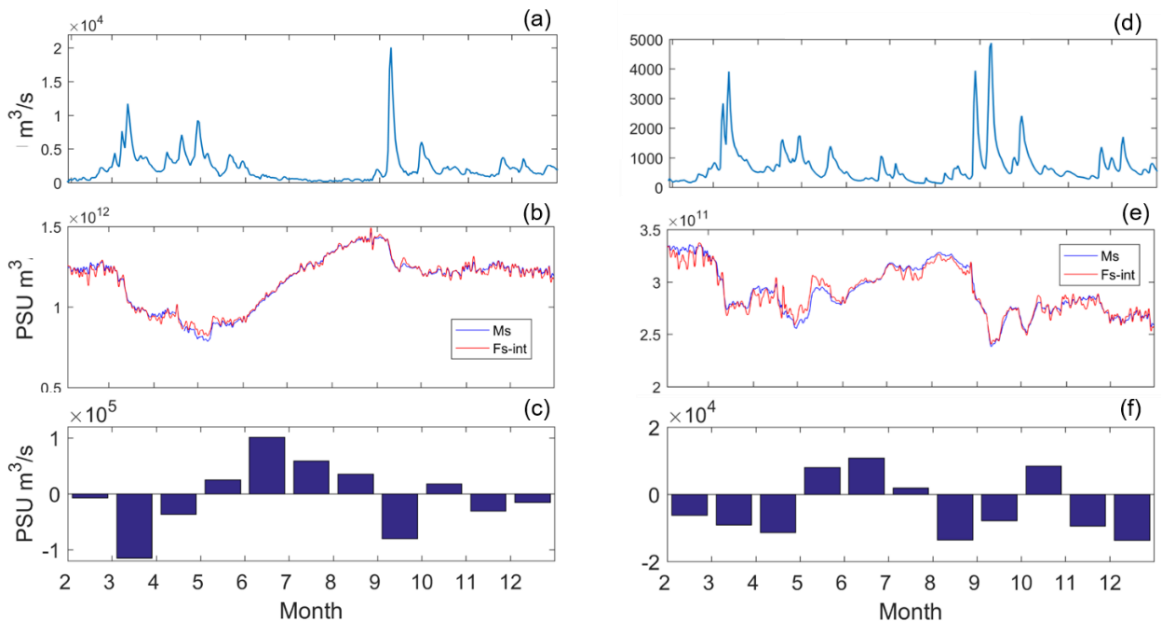

Figure 3.12 Time series of Susquehanna River discharge (a), salt content (blue line in b) and integrated salt flux (red line in b), and monthly salt flux (c) in Chesapeake Bay, and Delaware River discharge (d), salt content (blue line in e), and integrated salt flux (red line in e), and monthly salt flux (f) in Delaware Bay.

3.3.3 Temporal variation of Salt Flux Components: F0, Fe and Ft

To ascertain the relative importance of the different salt flux components, we have selected 80 cross sections from the bay mouth to the upstream end in both Chesapeake Bay and Delaware Bay and calculated the three components of the salt fluxes.

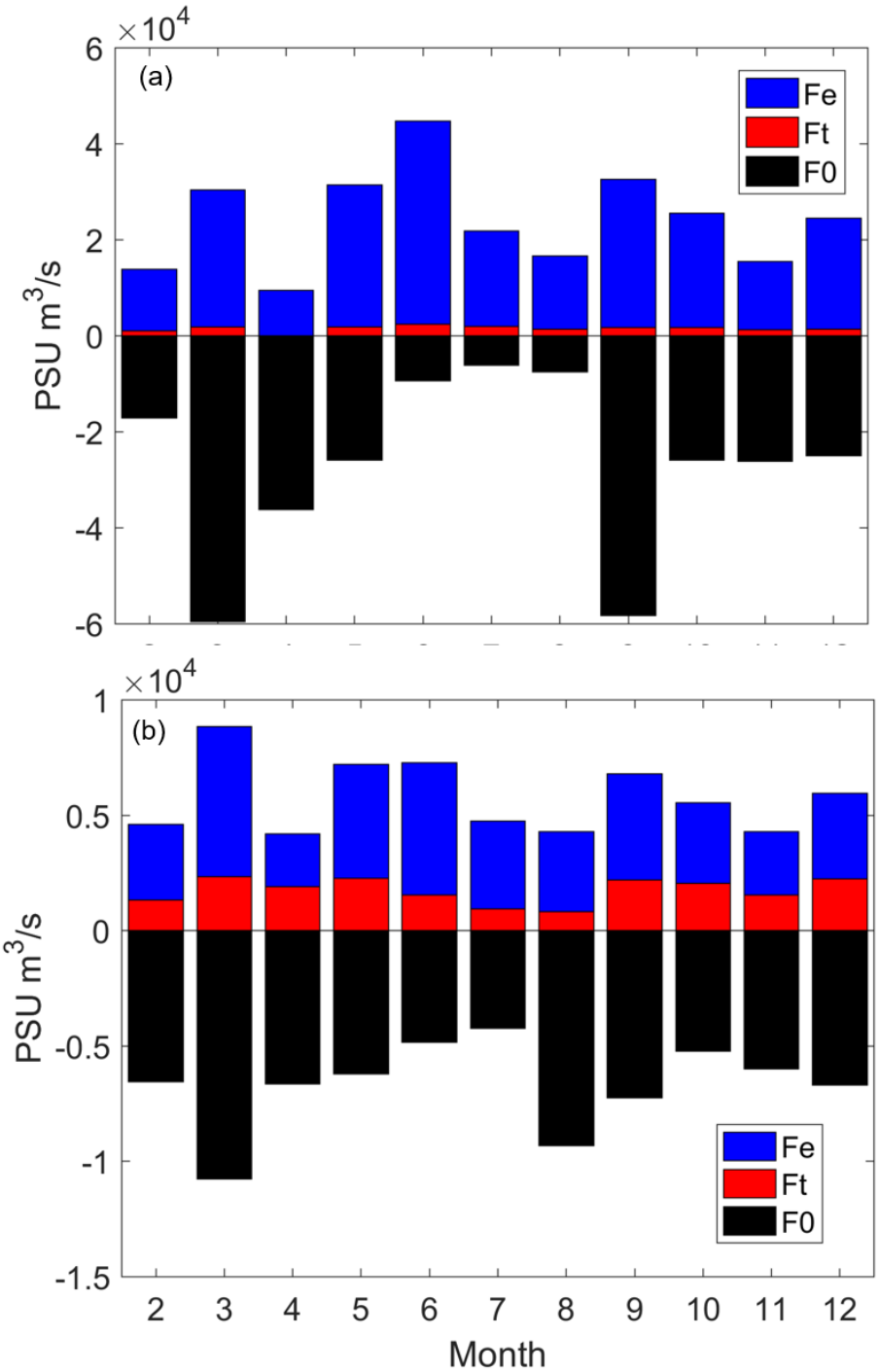

Figure 3.13 Averaged monthly salt flux decomposition components at 80 cross-sections in Chesapeake Bay (a) and Delaware Bay (b). Shear dispersion due to baroclinic

exchange flow Fe is shown with blue bar, tidal oscillatory salt flux is marked by red bar, and the advective salt flux F0 black bar.

Throughout the Chesapeake Bay, the salt flux induced by steady shear dispersion (Fe term) is always dominant in driving upstream salt flux (Fig. 3.13). This is not surprising because the estuarine circulation is strong in this partially-mixed estuary. The tidal oscillatory salt flux (Ft term) is trivial by averaging in the along channel direction. While keeping driving salt out of the bay for the entire year, the advective salt flux (F0 term) shows a strong seasonal variation: The value reaches the minimum during the dry time in summer and the maximum during winter and fall, which is consistent with the change of river discharge in the monthly scale.

In Delaware Bay, the tidal oscillatory salt flux (Ft term) becomes significant. The salt flux induced by steady shear dispersion (Fe term) plays an important role, even though Delaware Bay is a well-mixed estuary and the gravitational circulation is weak. In general, the two upstream salt flux terms Fe and Ft are comparative, which is consistent with the previous observation study in Delaware Bay by Aristizabal and Chant (2015).

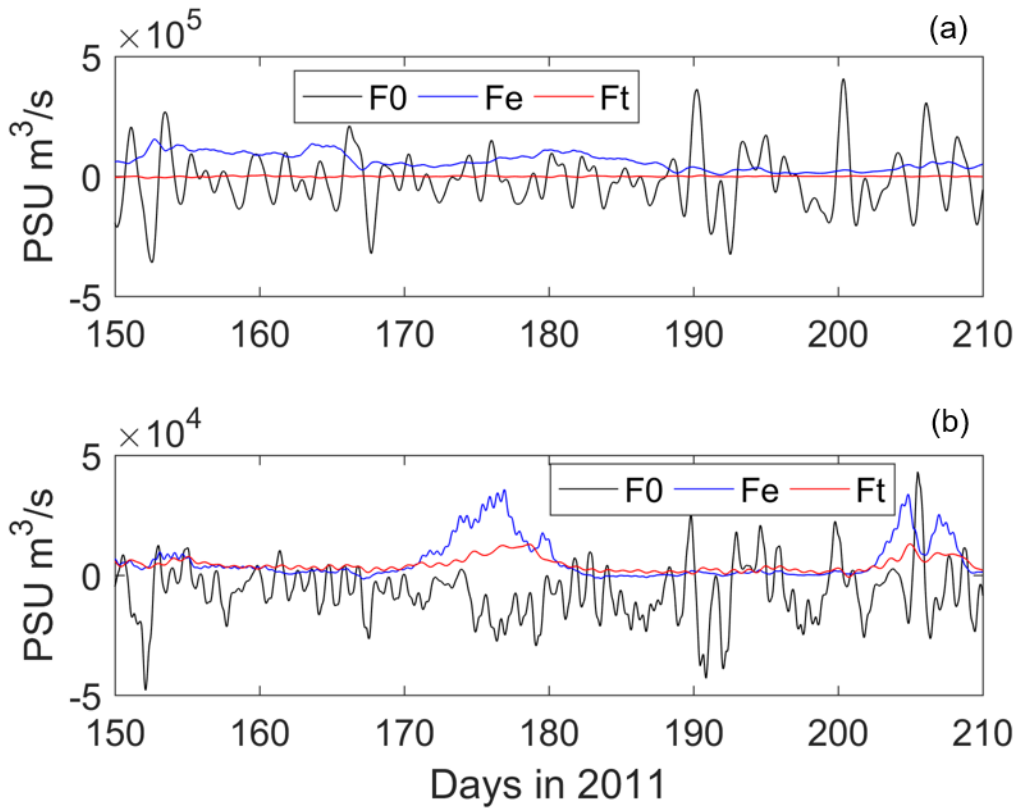

Figure 3.14 Times series of salt flux decomposition components at mid-bay section in Chesapeake Bay (a) and Delaware Bay (b): Shear dispersion due to baroclinic exchange flow Fe (blue), tidal pumping Ft (red), and subtidal barotropic transport F0 (black).

F0 term is the salt flux component associated with subtidal barotropic forcing, which includes river discharge and atmospheric forcing. In both bays, the fluctuation of F0 fluctuation is larger than Fe and Ft terms. In the long term, the bays should be in steady state where the upstream salt flux (Fe and Ft) should be balanced by the downstream salt flux (F0). F0, whose seasonal variation is consistent with seasonal river discharge change, always drives salt out of the bay. However, in the short term, F0 could lead to both landward and seaward salt transport. Consistent with the observational findings by Aristazabel and Chant (2015), the advective salt flux F0 is the dominated

component compared with the steady shear dispersion and tidal oscillatory salt flux in both Chesapeake Bay and Delaware Bay.

Time series of salt flux components (Fig. 3.14a) has also shown that the steady shear dispersion Fe is dominant in Chesapeake Bay in driving upstream salt flux. The evidence of Fe dominance for entire bay could be found in Figure 3.15. In this mid-bay section, the tidal oscillatory salt flux Ft is near to 0. This indicates the steady shear dispersion is the major mechanism driving the upstream salt flux in Chesapeake Bay. In Delaware Bay (Fig. 3.14b), Even though Ft is still smaller than Fe during strong neap tide (day 175 and 205), these two terms are comparable at most times. This result suggests that both steady shear dispersion and tidal dispersion are important in driving the upstream salt flux in Delaware Bay.

In both bays, the temporal variation of Fe and Ft terms is at the same pace. During the neap tides, both bays tends to be more stratified and the mixing is limited, thus the exchange flow is intensified and leads to a strong positive salt transport Fe. During neap tide, Ft is also enhanced. This is contrary to the case expected from previous studies by MacCready (2007). His parameterizations suggest that the along-channel dispersion coefficient is positively correlated with the magnitude of tidal current. Thus the weakened tidal current should lead to small Ft in neap tide and big Ft in spring tide. Our finding is consistent with the numerical simulations and observation study in Delaware Bay by Aristizabal and Chant (2013, 2014). The reason for such Ft variation is due to the stratification change. During neap tide, the stratification is large and leads to a big

variation of tidal salinity oscillation St. Thus the big tidal oscillatory salt flux is induced. During spring tide, even though the tidal currents increases, the reduced stratification causes a significantly small variation of St. Therefore, a small tidal oscillatory salt flux is found during spring tide.

3.3.4 Along-channel Variation of Salt Flux Components: Fe and Ft

Salt intrusion may be quantitatively determined by the combination of Fe and Ft. Their along-channel structures indicate to what extent the salt goes into the bays.

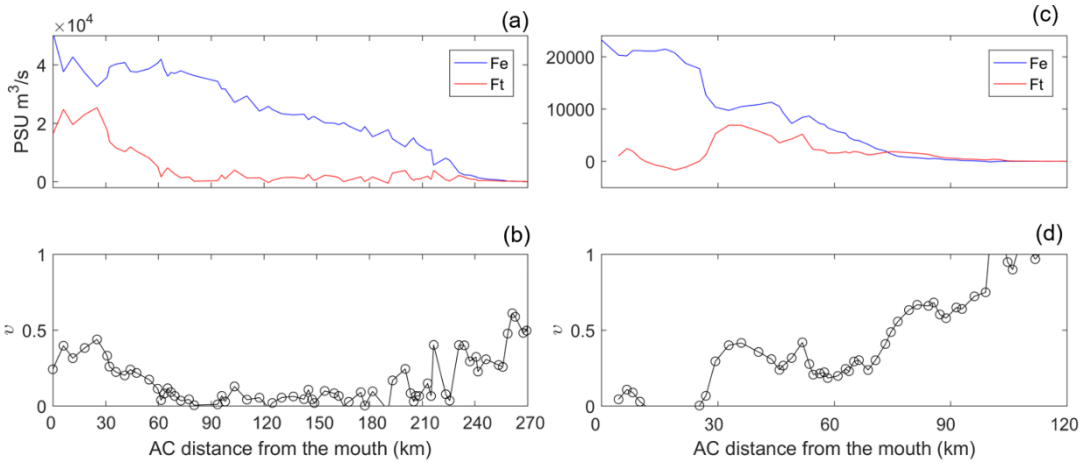

Figure 3.15 Along-channel distribution of lateral-integrated steady shear dispersion Fe and tidal oscillatory salt flux Ft and dispersive fraction of upstream salt fluxes (Ft/(Fe+Ft)), along the Chesapeake Bay (a, b) and Delaware Bay (c, d) estuary. Data plotted has been averaged in 2011.

Fig. 3.15 shows the area-integrated steady shear dispersion Fe and tidal oscillatory salt flux Ft and dispersive fraction of upstream salt fluxes, along the Chesapeake Bay and Delaware Bay estuary. In Chesapeake Bay, Fe is always larger over Ft and decreases almost linearly from the mouth to the upper bay. Ft term is large in lower-bay region (0-20 km) but decreases rapidly afterward. This may be because tidal pumping is only active in Chesapeake Bay mouth where a narrow constriction exists. It also shows the dispersion fraction is always smaller than 0.5 and almost close to zero in mid-bay. Because Fe and Ft tends to be zero from 160 to 180 km, the dispersion fraction may not accurately predict the dispersion processes in that area.

In Delaware Bay Fe term is much larger than Ft from 0 to 20 km. Ft even becomes negative in certain along-channel locations. From 20 to 60 km, Ft is closer to or even bigger than Fe term. This indicates the steady shear dispersion is relatively active in lower bay area and tidal dispersion becomes more and more significant toward the upstream direction. Overall, the dispersive fraction for Chesapeake Bay is much smaller than 0.5 while that for Delaware Bay is close to or much larger than 0.5 in mid and upper bay regions. Thus two bays' comparison shows that Delaware Bay is more dispersive than Chesapeake Bay, which means that a larger portion of salt is dispersed by tides into Delaware Bay than Chesapeake Bay. It also shows that the weakening of salt fluxes due to steady shear dispersion from the bay mouth to the upper bay is close to linear in Chesapeake Bay. The variation of salt flux components in Delaware Bay is not linear, which may be largely influenced by the variation of channel width.

§3.4 Discussion

3.4.1 What is controlling in the fluctuation of F0?

Fig. 3.16 shows that F0 is correlated with wind-driven sea surface height set-up and set-down. This subtidal sea level difference could be affected by various physical processes such as river discharge, local and remote wind's effect. It suggests even though in longer time scale such as one month F0 correlates well with river discharge, F0 does fluctuate extensively and primarily controls the total salt transport in short time scales such as several days.

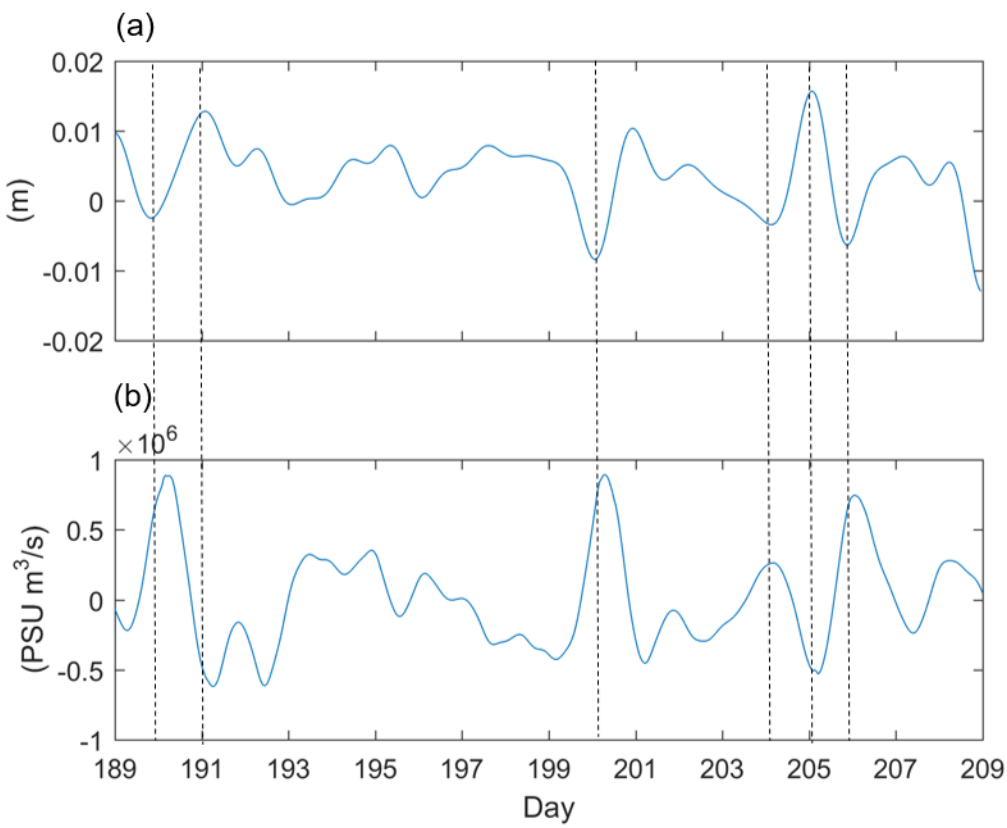

Figure 3.16 Time series of subtidal sea level difference across the near-mouth section (a) and F0 (b) in Chesapeake Bay.

3.4.2 What factor is controlling the along-channel variation of Ft?

Previous studies on the tidal oscillation salt flux Ft focused on the phase difference between tidal current V_t and tidal salinity variation S_t in order to explain the temporal and cross-channl variation of Ft (Wang et al, 2016; Aristizabal and Chant, 2013). When the phase difference between tidal velocity and salinity is close to 90 degrees (in quadrature), it appears to be standing wave and tidal oscillatory salt transport is close to 0; when the phase difference is smaller than 90 degrees, tidal oscillatory salt transport is positive, leading to upstream salt transport; when the phase difference is larger than 90 degrees, tidal oscillatory salt transport is negative, leading to downstream salt transport.

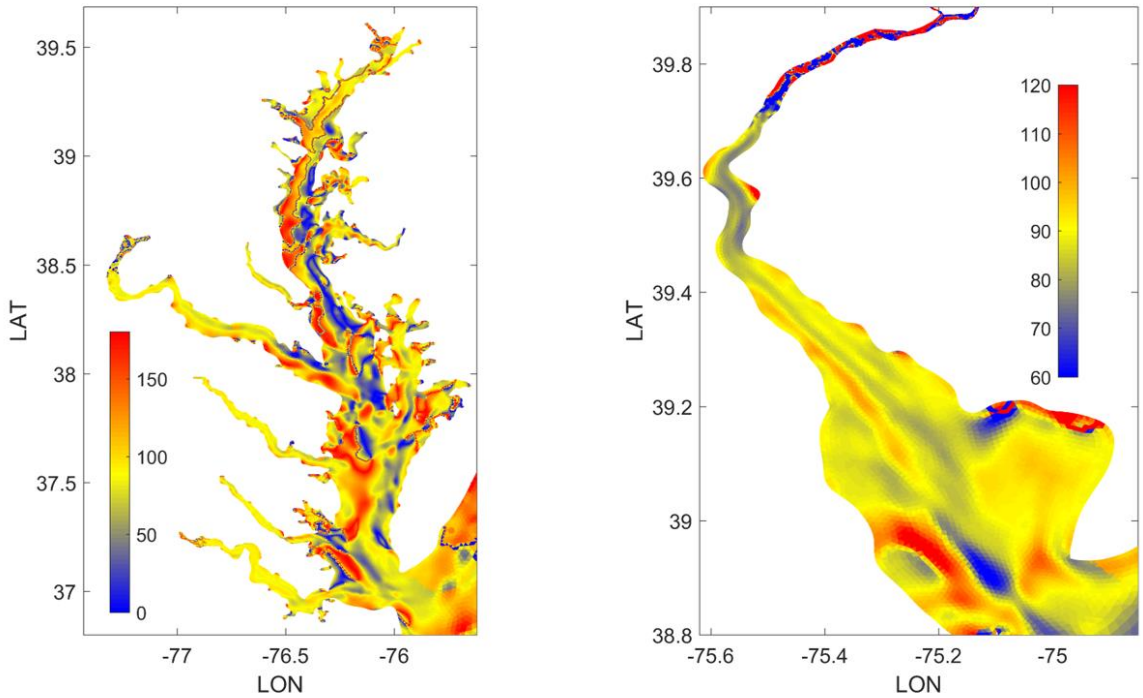

Figure 3.17 Phase difference between tidal current and tidal salinity variation in Chesapeake Bay (a) and Delaware Bay (b).

Fig. 3.17 shows the map of phase difference between the M2 components of tidal current and tidal salinity variation in Chesapeake Bay and Delaware Bay. In Chesapeake Bay, generally the phase difference is smaller than 90 degrees on the eastern shore (blue color), producing the positive values of Ft in this region. While on the western shore, the phase difference is larger than 90 degrees (red color). The yellow regions in Chesapeake Bay represent the existence of standing waves, which will limit the tidal salt flux. Lateral flows may result in this lateral variation of phase difference on two shores (Aristizabal and Chant, 2013). In Delaware Bay, the standing wave appears in most part of the lower-bay region where the phase difference is 90 degrees (in yellow). The phase difference

smaller than 90 degrees exists in the deep channel areas while the phase difference larger than 90 degrees is close to the western shore area.

The phase difference between tidal current Vt and tidal salinity variation St has been used by previous studies to explain the temporal variation of tidal oscillatory salt flux Ft in Hudson River (Wang et al., 2015) and the cross-channel variation of Ft in Delaware bay (Aristizabal and Chant, 2013). Figure 3.18 shows three scenarios of phase difference (smaller than, equal to or larger than 90 degrees) and correlated Ft sign.

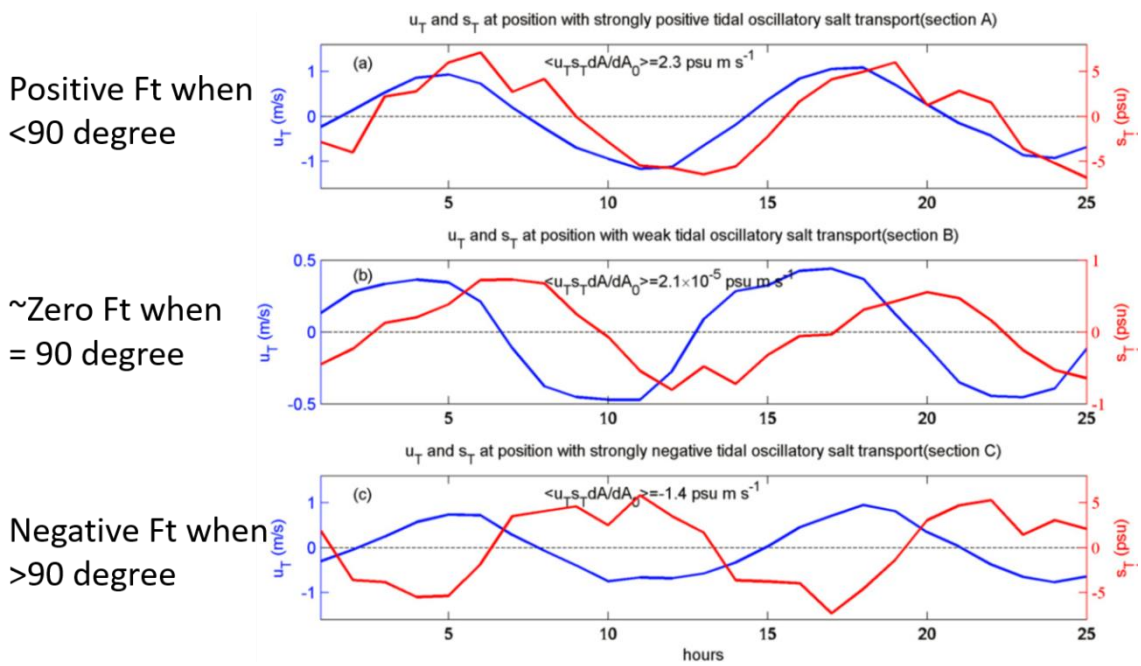

Figure 3.18 Three scenarios of phase difference (smaller than, equal to or larger than 90 degrees) and correlated Ft sign (Wang et al., 2015).

Here we examine whether the phase difference could explain the along-channel variation of Ft. The cross-channel average of phase difference is taken for 80 cross-channel sections in each of two bays (Fig. 3.19d and Fig. 3.20d).

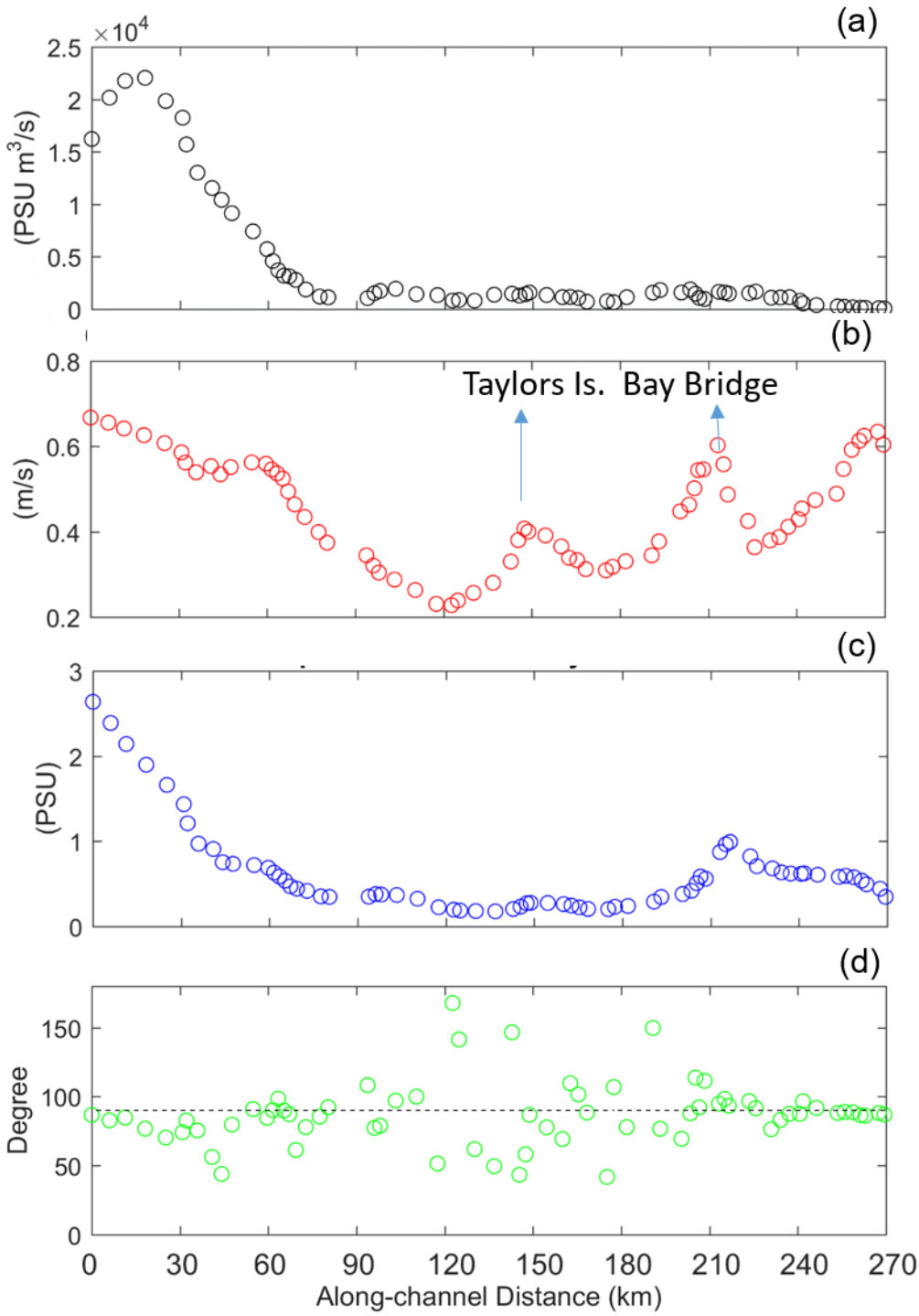

Figure 3.19 Along-channel distribution of (a) Ft, (b) amplitude of tidal current Ut, (c) tidal salinity oscillation St and (d) phase difference between Ut and St in Chesapeake Bay.

Ft in Chesapeake Bay is generally small and decreases rapidly in the along-channel direction (Fig. 3.19a). Due to the complicated coastline and many tributaries in Chesapeake Bay, the averaged phase difference shows a lot of fluctuations in the middle bay regions (Fig. 3.19d). In this case, the along-channel variation of phase difference is not obviously correlated with the along-channel variation of Ft. However, the longitudinal variation of tidal salinity oscillation St is correlated with the along-channel variation of Ft with a correlation coefficient of 0.87. Even though the tidal current is strong in Chesapeake Bay (Fig. 3.19b), the along-channel gradient of salinity is quite small due to the relatively long salt intrusion length (Fig. 3.19c). Thus the tidal oscillation of salinity is less than 3 psu in the mouth and rapidly decreases to a very small value in the lower bay region. Finally, Ft is only significant near the mouth region where the longitudinal gradient of salinity is large and remains close to 0 in other regions of Chesapeake Bay.

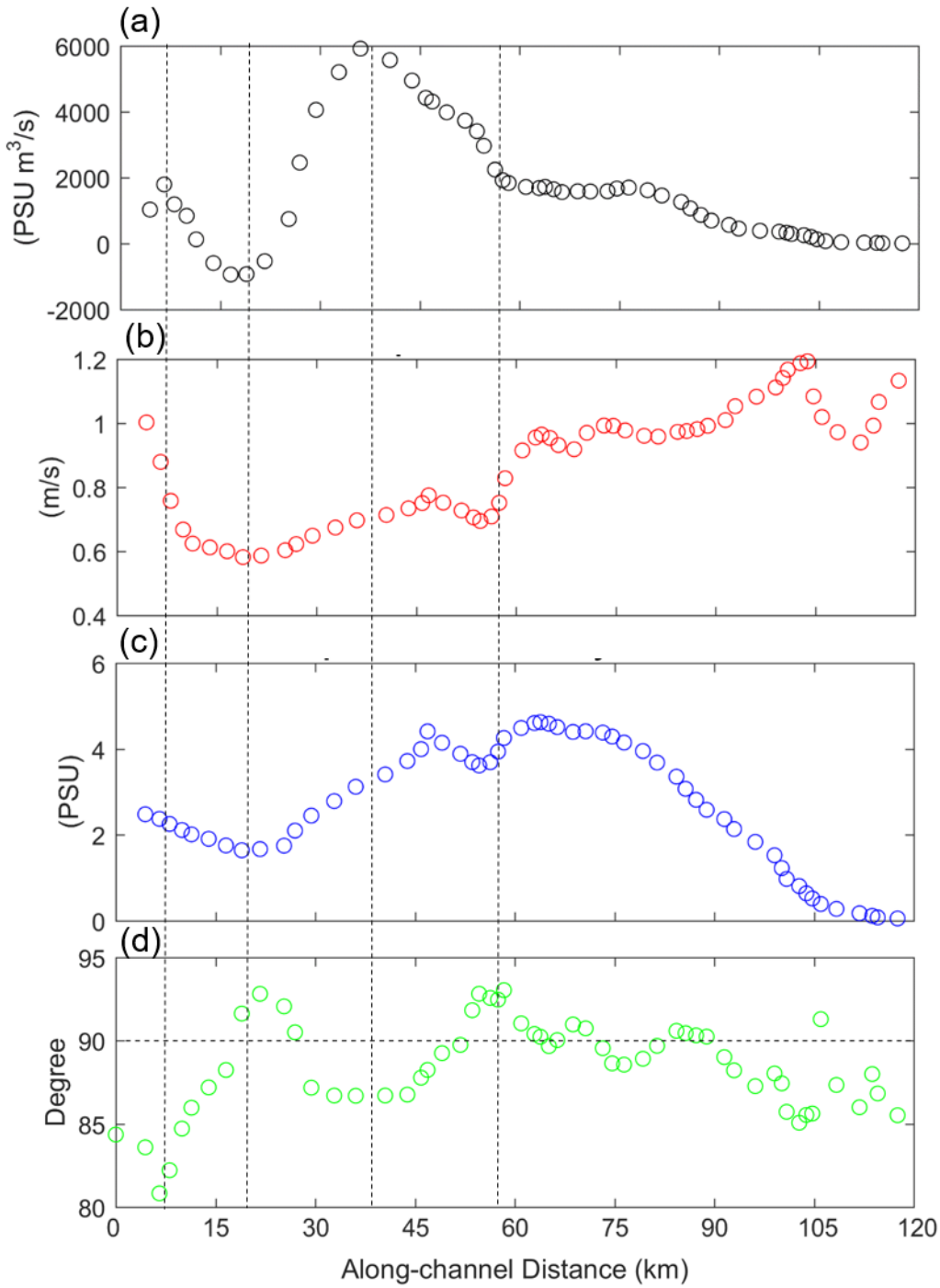

Figure 3.20 Along-channel distribution of (a) Ft, (b) amplitude of tidal current Ut, (c) tidal salinity oscillation St and (d) phase difference between Ut and St in Delaware Bay.

In Delaware Bay, the phase difference plays a dominant role in determining the Ft. In the lower and middle bay regions, the maximum value of Ft is always associated with the minimum value of phase difference while the minimum value of Ft is correlated with the maximum value of phase difference (as shown with vertical dashed black lines in Fig. 3.20). In the upper bay, the small Ft values appear to be caused by the decline of the salinity oscillations regardless of the intensified tidal current.

3.4.3 Isohaline Decomposition of Salt Fluxes

The volume flux through the mouth section using the isohaline analysis, $\partial Q/\partial s$, is plotted versus salinity in Fig. 3.21. This reveals that the average inflow into Chesapeake Bay happens over a relatively wide salinity range (28-34). The outflow in Chesapeake Bay occurs over a relatively larger salinity range distributed from 20 to 28. This is indicative of the mixing that occurs within the estuary. Compared with Chesapeake Bay, the average inflow and outflow in Delaware Bay covers a relatively narrow salinity range (22-33). The difference between average inflow and outflow salinity in Delaware Bay (1 psu) is very small compared with Chesapeake Bay (9 psu). There is a smaller range of low salinity classes (such as 26) going landward in Delaware Bay. This may be due to the existence of multiple layers of the lateral exchange flow in Delaware Bay.

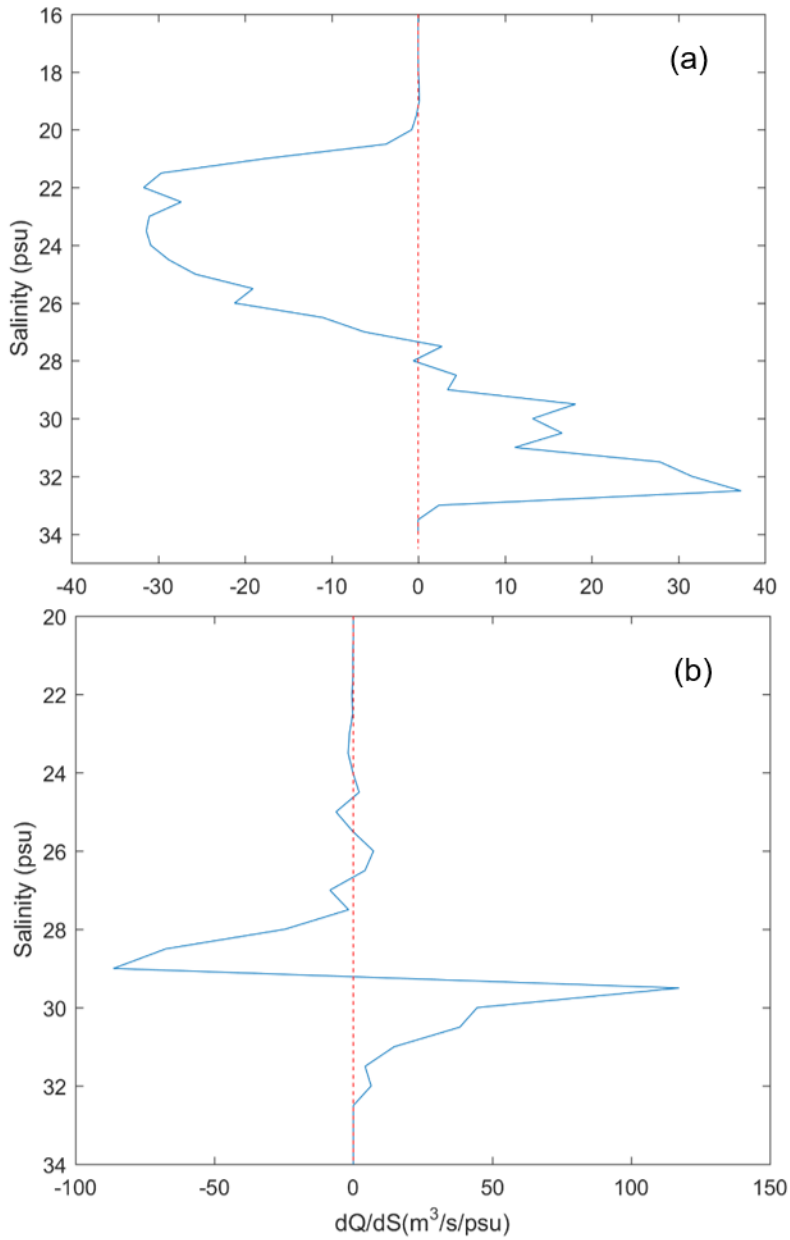

Figure 3.21 The differential isohaline transport function ∂Q/∂s vs salinity, at the Chesapeake Bay (a) and Delaware Bay (b) sections closest to the mouth, averaged over a year.

The isohaline analysis does not directly explain what physical processes are controlling the salt content variability. Here we look at the temporal variation of TEF and

its possible correlation with the river discharge. The temporal variation of TEF term $\partial Q/\partial s$ is presented in Fig. 3.21 S_{out} ranges from 12 to 24 and S_{in} only varies from 30 to 34. It appears that in Chesapeake Bay the outflow salt transport has a large seasonal variation correlated with seasonal river forcing. High river runoff freshens the outflow salinity in spring and fall. Low river runoff and high evaporation leads to saltier outflow during summer. The inflow salinity transport variation is limited.

In Delaware Bay the outflow salt transport shows an apparent significant correlation with storm events happened in 2011. For example, Hurricane Irene (August 21 – August 28) made landfall on Cape Lookout, North Carolina and Tropical Storm Lee reached mid-Atlantic area at the beginning of September. Both drove a large river runoff from Delaware River, which may have caused an extreme jump in outflow salinity transport and thus a decrease in outflow salinity S_{out}. As it was found in Columbia River (McCready 2011), Puget Sound (Sutherland et al. 2011) and Hudson River (Wang et al. 2016), Q_{in} and S_{in} are almost constant regardless of normal river discharge change. We found the same in Delaware Bay, where Sin is around 31 psu even though a seasonal river discharge variation and storm events are imposed. Many previous studies (Aristazabel and Chant 2013; Garvine et al. 1992) indicated that there is a buffering mechanism in Delaware Bay, making salt intrusion insensitive to river discharge. The relative steady values of Qin and Sin are another indicator of this buffering mechanism.

Finally we calculated the quantity ‘river amplification factor’ (MacCready 2011).

$$\alpha_R = \frac{Q_{in}}{Q_R} \tag{3.19}$$

This is a dimensionless expression of the exchange flow, a defining estuarine property. It could be useful for characterizing different estuarine systems. It may show how effective an estuary exchange flow could be induced by river discharge. It also could represent how well an estuary is mixed. α_R is around 1 for Columbia River and 20 for Puget Sound at Admiralty Inlet (Babson et al. 2006). Our calculation shows that α_R is about 25 for Chesapeake Bay and 157 for Delaware Bay. This indicates that even though the river discharge is much smaller in Delaware Bay than Chesapeake Bay, Delaware Bay is more ffective in driving the exchange flow given the same amount of runoff volume. One of the reasons for that may be because the complicated coastline and bathymetry in Chesapeake Bay yields big friction and slows down the estuarine circulation while the funnel shape of Delaware Bay speeds up the outflow.

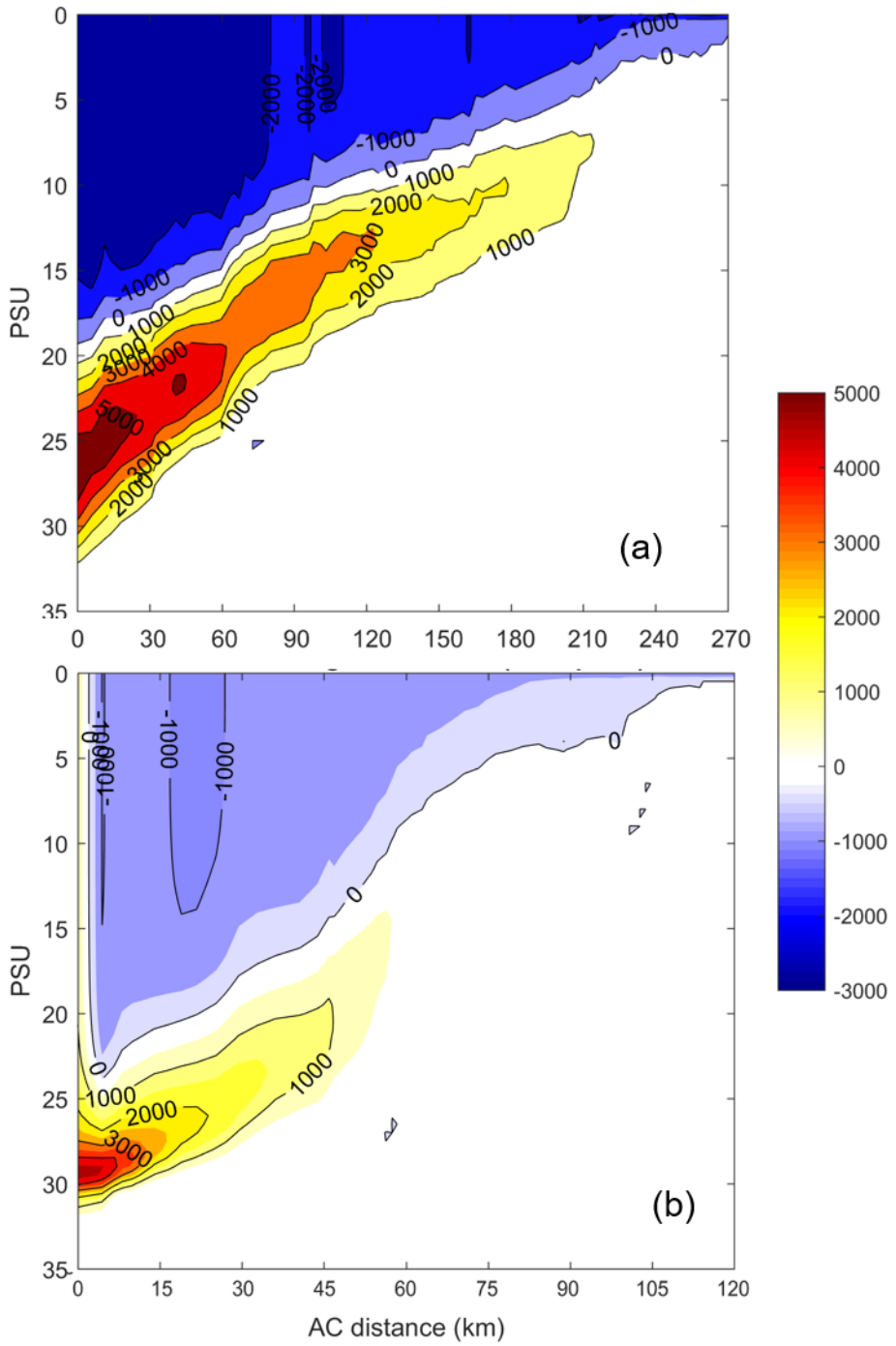

Figure 3.22 Contour plot of the isohaline transport function Q(x, s) in Chesapeake Bay (a) and Delaware Bay (b), averaged over a year.

The isohaline transport function Q(x, s) is plotted in Fig. 3.21. In the isohaline framework, this estuarine circulation map describes how the salty water comes into the bay, travels upstream, mixes with freshwater, and then returns back to the ocean with a lower salinity. The Q contours of the outflowing water slope are downward toward the mouth. This indicates that outgoing water is being continually made saltier. Turbulence mixing needs to take effect in this process. To the opposite, the inflowing water has Q contours sloping up toward the river end, indicating turbulent freshening. The maximum value of Q at any along-channel location is equal to Q_{in} at that place. Fig. 3.21 demonstrates one advantage of isohaline coordinate. It gives more information than traditional exchange flow (such as how much is the volume transport in certain salinity classes) regardless of channel depth, width or shape.

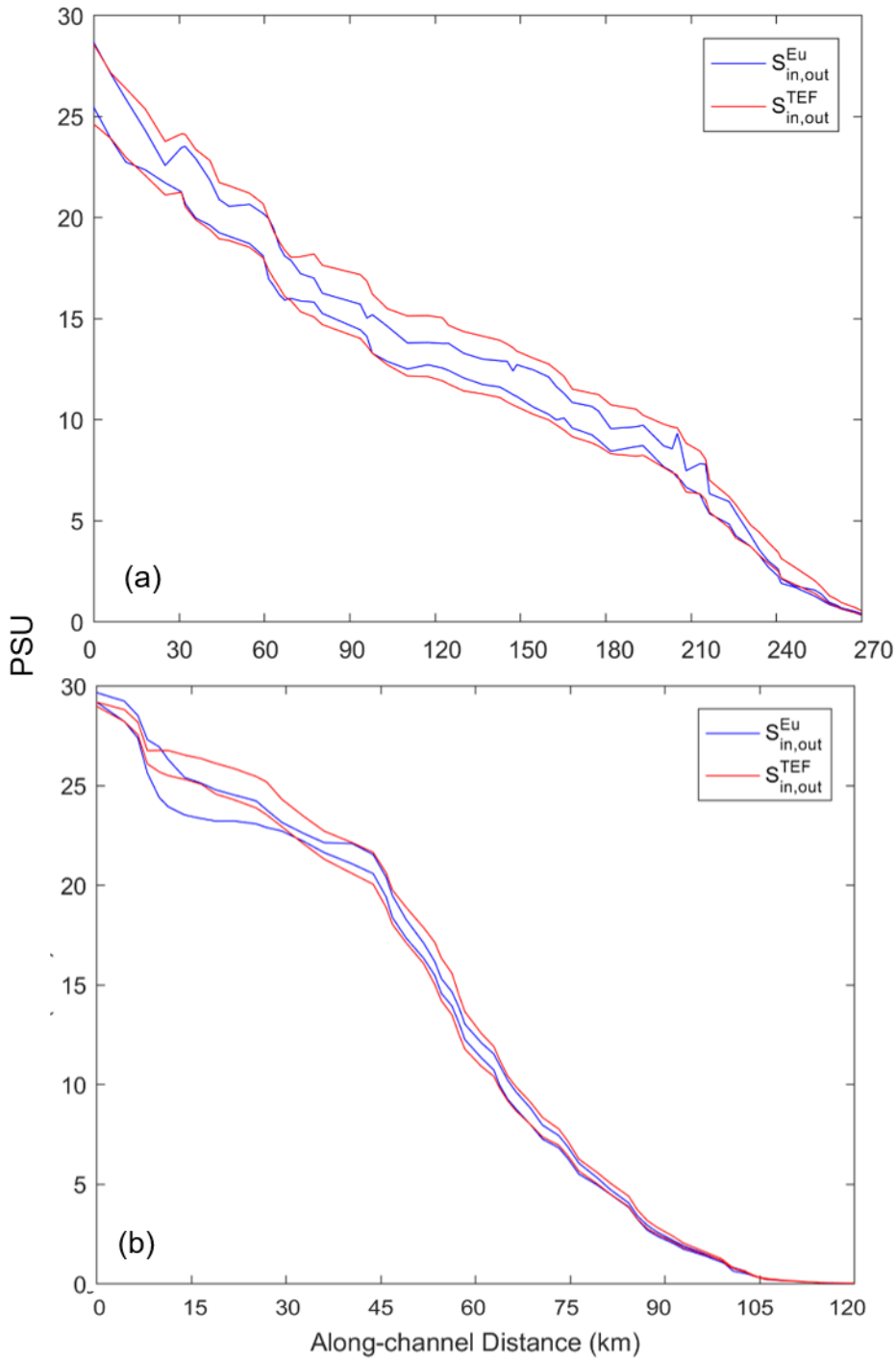

Figure 3.23 TEF salinity (red) in Chesapeake Bay (a) and Delaware Bay (b) vs along-channel distance, averaged over a year. For comparison, the same properties calculated from the Eulerian-averaged properties are plotted in blue.

Fig. 3.23 shows the along-channel distribution of S_{in}, and S_{out}. The isohaline exchange transports a generally greater range of salinity values. Same as in Eulerian framework, the difference between S_{in} and S_{out} is larger in more stratified Chesapeake Bay than in the generally well-mixed Delaware Bay. An interesting difference of along-channel distribution of S_{in} and S_{out} between Chesapeake Bay and Delaware Bay is that $\partial S/\partial x$ is smaller in mid-bay area compared with other areas in Chesapeake Bay while bigger in mid-bay area compared with other areas in Delaware Bay.

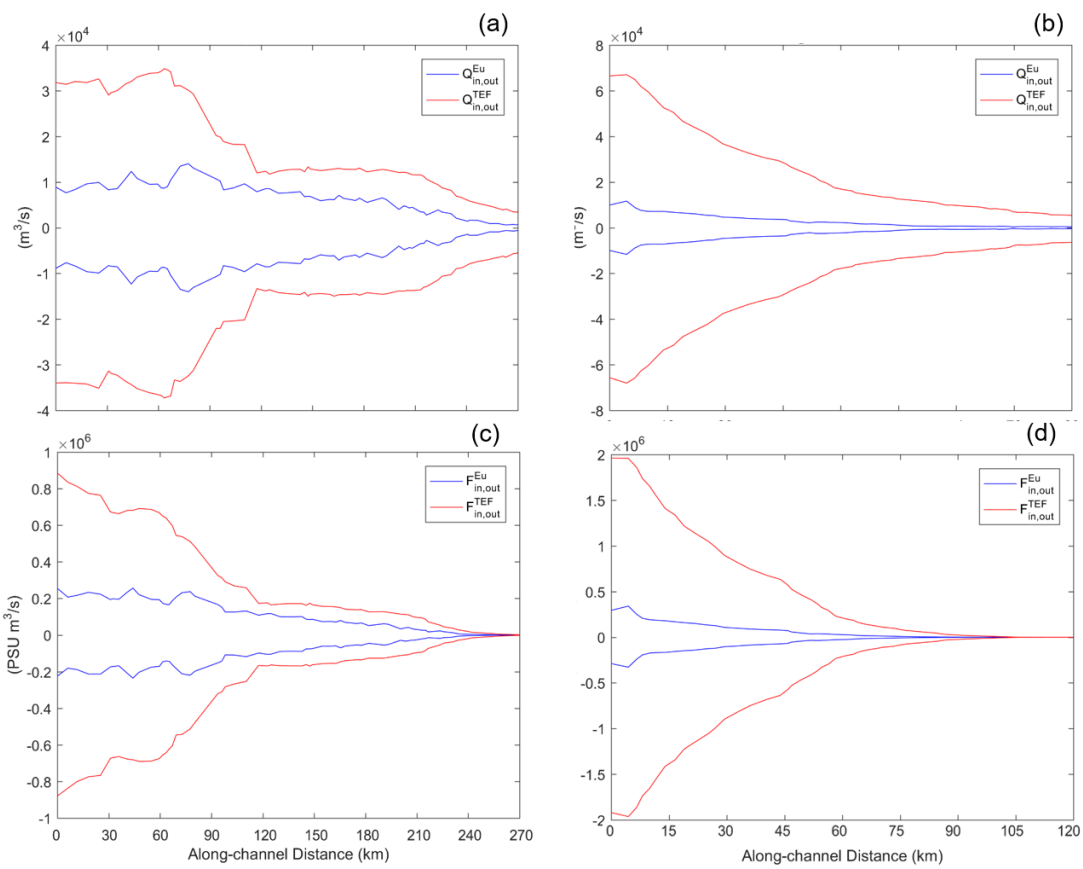

Figure 3.24 Along-channel distribution of TEF transport (red) in Chesapeake Bay (a) and Delaware Bay (b) and the TEF salt flux (red) in Chesapeake Bay (c) and Delaware

Bay (d), averaged over a year. For comparison, the same properties calculated from the Eulerian-averaged properties are plotted in blue lines.

The total exchange flow looks like an enhanced version of the Eulerian exchange flow: Both the volume of TEF inflow and outflow are generally 3 times larger than that of the Eulerian exchange flow. Evidence is shown in Fig. 3.24a-b. In both bays, the isohaline exchange is much larger than its Eulerian counterpart. The along-channel distribution of $Q_{in,out}$is much smoother in Delaware Bay than Chesapeake Bay. This may be because the complex shoreline in Chesapeake Bay affects the tidal processes by storing or releasing water with certain salinity classes. In Delaware Bay, $Q_{in,out}$ decreases smoothly from the oceanside to landside. The situation is different in Chesapeake Bay, where $Q_{in,out}$ decreases rapidly from 40km to 80km and almost remains unchanged in other areas. This indicates the cross-critical isohaline salt transport (entrainment) is strong from 40km to 80km and weak in other along-channel regions. Fig. 3.24c-d differentiates the salt flux induced by subtidal processes from tidal processes. $F_{in,out}^{Eu}$ represents the magnitude of subtidal salt fluxes while $F_{in,out}^{TEF}$ is the magnitude of total salt fluxes. And their difference is the salt fluxes included by tidal processes, which is around 75% of the total salt flux in Chesapeake Bay and about 85% of that in Delaware Bay. This suggests the more important role of tides in driving the salt transport in Delaware Bay than in Chesapeake Bay. In addition, it also indicates that most of the total salt transport is driven by tides in both Chesapeake Bay and Delaware Bay. However, the salt transport by tides may not lead to a net salt transport over a tidal cycle, which

explains why the tidal salt flux term Ft is smaller than the subtidal salt flux term Fe in both Chesapeake Bay and Delaware Bay (Fig. 3.14). The sudden drop of $Q_{in,out}^{TEF}$ and $F_{in,out}^{TEF}$ could be seen at 80 km in Chesapeake Bay, which results from one significant part of water and salt transport going into one major Chesapeake Bay tribute - Potomac river. The smooth along-channel variation of volume transport $Q_{in,out}^{TEF}$ and salt transport $F_{in,out}^{TEF}$ provides a natural and combined picture of the along-channel salt transport from the bay mouth to the upstream regardless of whether tidal or subtidal processes are dominant. The isohaline exchange flow is larger than its Eulerian counterpart, which indicates the contribution of tidal exchange. In Chesapeake Bay, TEF is around three times as large as its Eulerian counterpart while in Delaware Bay TEF is around ten times as large as its Eulerian counterpart. This difference suggests that the tidal exchange plays a more important role in Delaware Bay than in Chesapeake Bay.

§3.5 Conclusions

A numerical model using the Finite Volume Coastal Ocean Model (FVCOM) is configured to study the salt fluxes in Chesapeake and Delaware Bays for the year 2011. The model covers Chesapeake Bay, Delaware Bay and Mid-Atlantic Bight, and is forced by realistic atmospheric forcing, tides and river discharge. The model gives reasonable prediction in sea level and salinity in Chesapeake Bay and Delaware Bay.

Salt budget analysis shows the seasonal salinity variation: both Chesapeake Bay and Delaware Bay are gaining salt during summer and losing salt during spring and

winter. Storm-induced high river discharge flushes the two bays significantly in September but salt compensation happens in following October. Consistent with observation in 2011, the Delaware Bay has been freshened to a large extent due to the high precipitation induced by several storms.

Two methods are used for the analysis of salt flux. Under the Eulerian framework, the along-channel salt flux is decomposed into three parts: an advective term associated with the barotropic forcings such as river flow and wind, a steady shear dispersion term Fe associated with the estuarine exchange flow, and a tidal oscillatory salt flux Ft. Time series of F0, Fe and Ft shows that the advective salt flux is dominated in salt transport variation over the other two terms. F0 correlates well with river discharge in a monthly time scale but fluctuates with a main period of 2 days, associated with wind-driven sea surface height set-up and set-down. This indicates wind stress may act in the water surface and induce significant barotropic forcing, which dominates F0 variaion.

In Chesapeake Bay, the exchange flow is relatively strong, thus steady shear dispersion is always the dominant mechanism in salt transport and tidal oscillatory salt flux only contributes about 10% of total upstream salt flux in the near-mouth sections. The trivial value from Ft may result from the fact that Chesapeake Bay has a relatively long channel and its along-channel salinity gradient is too small to generate the strong oscillation of salinity by tidal current.

In Delaware Bay, the channel is relatively short and exchange flow is weak due to well mixed conditions. Thus, these two salt flux components Fe and Ft are comparable, which indicates Delaware Bay to be more dispersive than Chesapeake Bay. The difference of the steady shear dispersion between two bays is that it is mainly induced by the vertical shear in Chesapeake Bay while by the lateral shear in Delaware Bay. The along-channel variation of Ft term could be explained by looking at the variation of the amplitude of tidal current and tidal salinity oscillation and the phase difference between them. In Chesapeake Bay, the along-channel variation of Ft is mainly limited by the magnitude of the tidal oscillation in salinity. The tidal oscillatory salt flux Ft is trivial except in the near-mouth sections where the tidal oscillation of salinity is significant. In Delaware Bay, the along-channel variation of Ft is mainly due to the change of phase difference between tidal current and salinity.

The isohaline analysis gives detailed information about the salinity classes that are transported in or out of the bay and their respective volume. Compared with Eulerian results, it also appears that a relatively larger range of salinity classes is transported by the isohaline exchange flow in both bays. The isohaline exchange flow exactly fits in the Knudsen's relation by incorporating and vanishing the dispersion term and thus provides a more accurate estimate of exchange flow. Results show that the isohaline exchange flow is about 3 times as large as the Eulerian exchange flow in Chesapeake Bay and around 10 times in Delaware Bay, which indicates the important role of tide in salt exchange in Delaware Bay.

The isohaline outflow transport Q_{out} has a significant temporal variation correlated with river forcing and storm events. However, the isohaline inflow transport Q_{in} is relatively steady especially in Delaware Bay regardless of river discharge change. This is consistent with previous findings in Columbia River (McCready, 2011), Puget Sound (Sutherland et al. 2011) and Hudson River (Wang et al. 2016). It is still a question what causes the relatively steady value of Q_{in}.

The isohaline exchange flow exactly fits in the Knudsen's relation by incorporating and vanishing the dispersion term and thus provides a more accurate estimate of exchange flow. Under isohaline framework, the along-channel variations of salt transport decreases smoothly in both bays regardless of whether tidal or subtidal processes are dominant.

CHAPTER 4 CONCLUSIONS

§4.1 Research Conclusions

Using a combination of numerical models and field observations, this dissertation investigated the time and scale dependence of estuarine longitudinal dispersion and the relative importance of physical mechanisms in driving salt longitudinal dispersion in partially-mixed and well-mixed estuaries. The research findings are applicable to many other estuaries with similar tidal forcing conditions or mixing types. A summary of major research findings is listed below.

Time and scale dependence of estuarine longitudinal dispersion

The four dye release experiments in the James River estuary showed that the longitudinal dispersion rate had large flood-ebb and spring-neap differences. The numerical model reproduced the observed dispersion and provided an explanation in terms of the vertical shear dispersion. Tidal straining enhances vertical current shear on ebb tides and promotes longitudinal dispersion. In contrast, tidal straining reduces vertical shear on flood tides and increases vertical mixing, thus suppressing longitudinal dispersion. The large differences in the dispersion rate between spring and neap tides can also be interpreted in term of the differences in the vertical shear dispersion. Due to strong spring mixing, a dye patch quickly extends from the bottom to the surface, exposing to the full vertical shear in the water column and leading to strong longitudinal dispersion. In contrast most of the dye patch is limited to bottom few meters during neap tides. Although weak vertical mixing facilitates longitudinal dispersion, the vertical shear

across the thin dye patch is much weaker, leading to weak longitudinal dispersion during neap tides.

The second moment of the dispersive estuarine material in the along-channel direction increases with time at a power of between 2 and 3. The longitudinal dispersion rate varies as the four-third power of the material size, indicating scale-dependent diffusion. This is consistent with the "four-thirds" law describing relative dispersion in turbulent flows (Richardson, 1926; Batchelor, 1952) and has been found to describe oceanic dispersion in a wide range of flow conditions (Okubo 1971).

Comparative study of salt fluxes in partially mixed and well mixed estuaries

Salt dispersion and transport are examined in a comparative numerical modeling study between the partially-mixed Chesapeake Bay and the well-mixed Delaware Bay. To investigate how different physical mechanisms drive the salt transport into the estuaries, the longitudinal salt fluxes are decomposed using the Eulerian and Lagrangian methods. Under the Eulerian framework, the salt flux is decomposed into three parts: an advective term F0 associated with the barotropic forcing, a steady shear dispersion term Fe associated with the estuarine exchange flow, and a tidal oscillatory salt flux Ft. In both types of estuaries, F0 fluctuation is larger than Fe and Ft and contribute most to the temporal variation of total salt flux. In partially-mixed estuary, the exchange flow is significant and the steady shear dispersion is the dominant mechanism and the tidal oscillatory salt flux Ft is small. In well-mixed estuary, the exchange flow is relatively

weak and tides are strong, so tidal dispersion becomes important. The along-channel variation of Ft is mainly due to changes of the phase difference between the tidal current and salinity. Isohaline analysis using the Lagrangian methodology can be applied to describe the evolution path and transport volume of each salinity class. The comparison of results from Eulerian and Isohaline analysis demonstrates the relative importance of tidal and subtidal processes in driving salt transport in different types of estuaries: tidal volume exchange contributes to larger portion of total volume exchange and salt exchange between estuaries and ocean in well-mixed estuary than partially-mixed estuary.

§4.2 Research Applications

The improved understandings of estuarine dispersion imply meaningful use for broad areas of ocean science.

This study provides positive implications for estuarine biological restoration. For example, location is usually an important factor to consider for maximizing the oyster restoration benefits (Mann and Evans, 2004). This dissertation suggests that timing may also be a key factor that influences the dispersion of larvae: More will stay in the targeted locations of the estuary if being placed during neap tide while more will be dispersed widely if during spring tide. Our better understanding of the dispersion processes will contribute to the development of quantitative models that reflect the bio-physical interactions in our ecosystem.

This dissertation work also potentially promotes our understanding for the protection of the coastal environment. Estuaries are under the potential contamination by human activities such as the disposal of sewage and industrial waste (Goldberg et al. 1978; Kadirvelu et al. 2001). In case of the pollutants injected or oil spill in the estuaries, the study of longitudinal dye dispersion gains our knowledge about their dispersion. The findings about the flood-ebb variation in dispersion rate indicate that soluble materials dropped in the estuaries may be transported much faster during ebb than flood time. Their dispersal is also even quicker if the oil spill accident happens during spring tide. Furthermore, skilled realistic modeling of dispersion could be a supporting tool in predicting the pollutant transportation. The consistency between model results and observation dataset provides more confidence in applying hydrodynamic numerical simulations to solve real world problems.

The comparative study of salt flux in the partially-mixed Chesapeake Bay and the well-mixed Delaware Bay suggests their different response toward the variation of external forcings. Delaware Bay loses about 1/3 of its salt content during 2011 when storm events are frequent. Kundzewicz et al. (2007) summarized from many hydrological modeling studies that precipitation is projected to occur less frequently (longer dry periods) but the intensity of precipitation events will increase (Meehl et al., 2007). The strong link between precipitation and streamflow indicates the streamflow will be more extreme in future. Owning to this, it indicates that Delaware Bay may be more vulnerable to the impact of climate change. In the case of Chesapeake Bay, the salt is mostly driven

by steady shear dispersion. Increased river flow may accelerated the gravitational flow. And the enhanced steady shear dispersion will neutralize the increased salt lose due to the advective salt flux. With this modulation effect, the Chesapeake Bay may be more resistant to future climate variability.

APPENDIX A

OBSERVATION OF DYE DISPERSION IN JAMES RIVER ON MAY 5, 7 AND 25, 2010.

Four dye release survey has been conducted in James River estuary. Chapter 1 show the one happened on May 27, 2010. In this appendix, we show the three-dimensional evolution of observed dye in May 5, 7 and 25 releases.

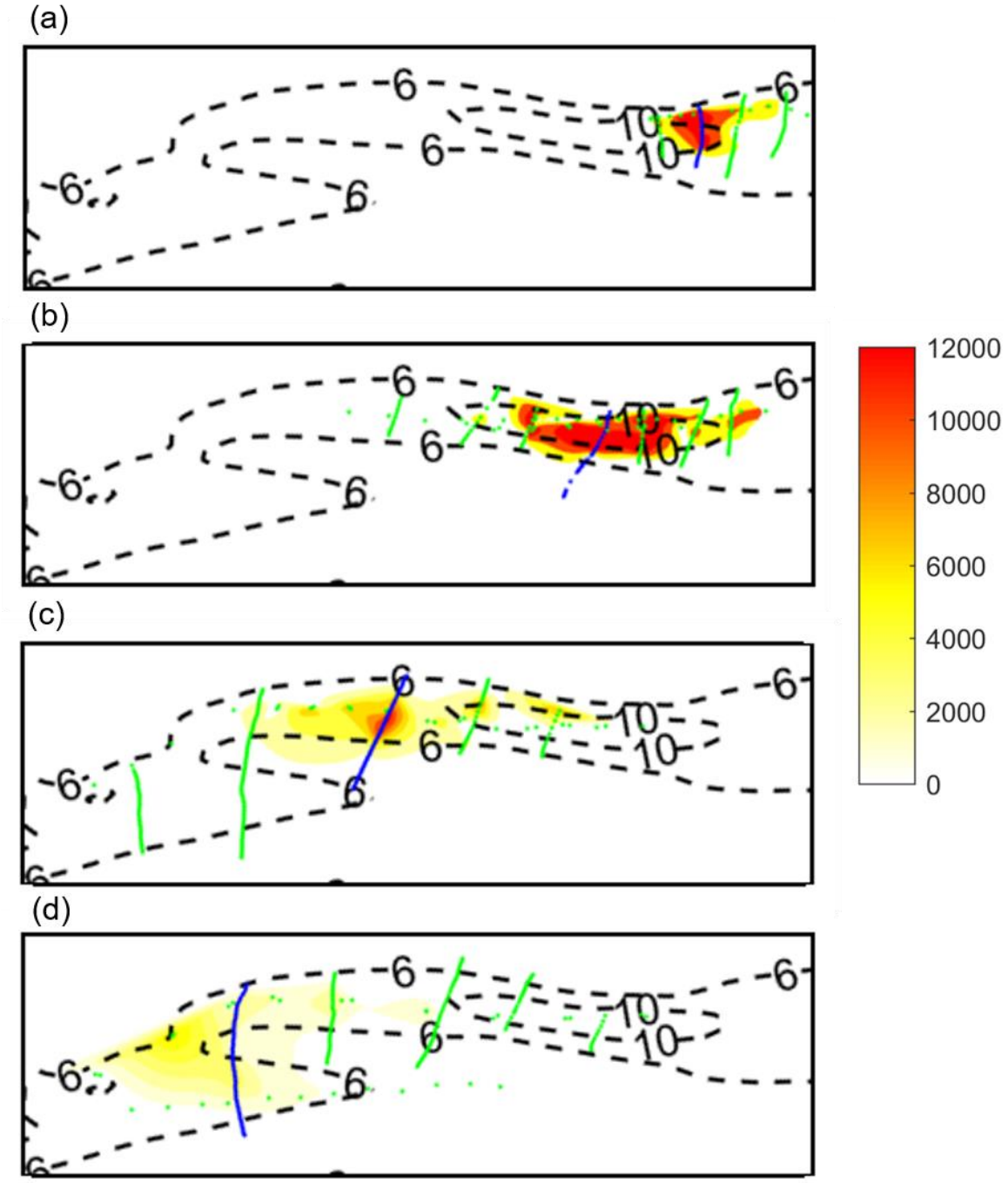

Figure A1. Plan view of the vertically integrated dye patch concentration (color) at (a) 3.8, (b) 4.5, (c) 7.3, (d) 9.1 hours after the dye release on May 5. The dashed lines show the bathymetry in meters. The dotted green and blue lines mark the cross-channel transects taken to sample the dye patch. The dotted blue lines mark the cross-channel transects plotted later.

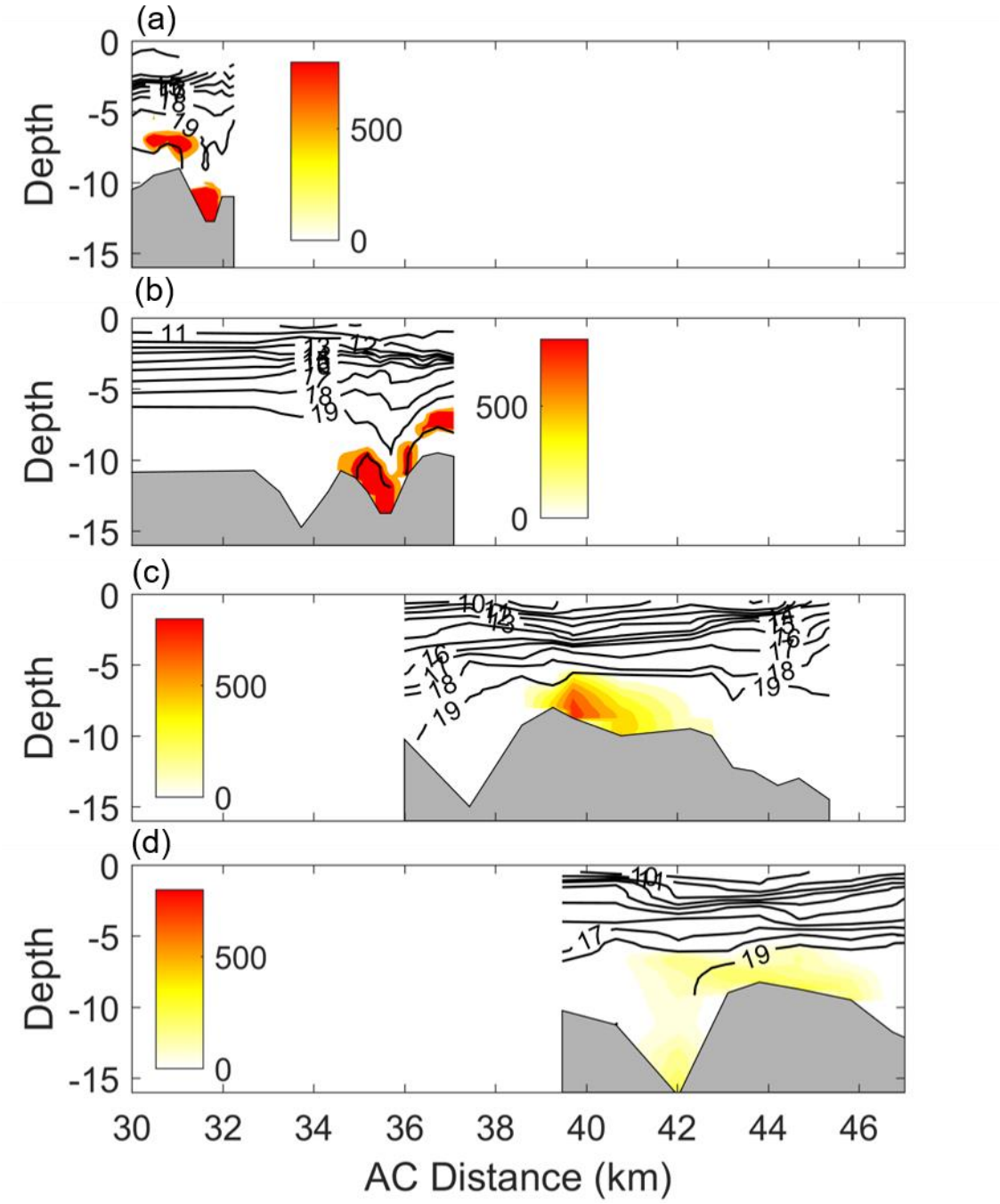

Figure A2. Along-channel distributions of dye concentration (color, 10^{-8} kg/m^3) and salinity (contour, psu) at (a) 3.9, (b) 4.5, (c) 8.3, (d) 9.2 hours after May 5 release. X-axis is the along-channel distance from estuarine mouth.

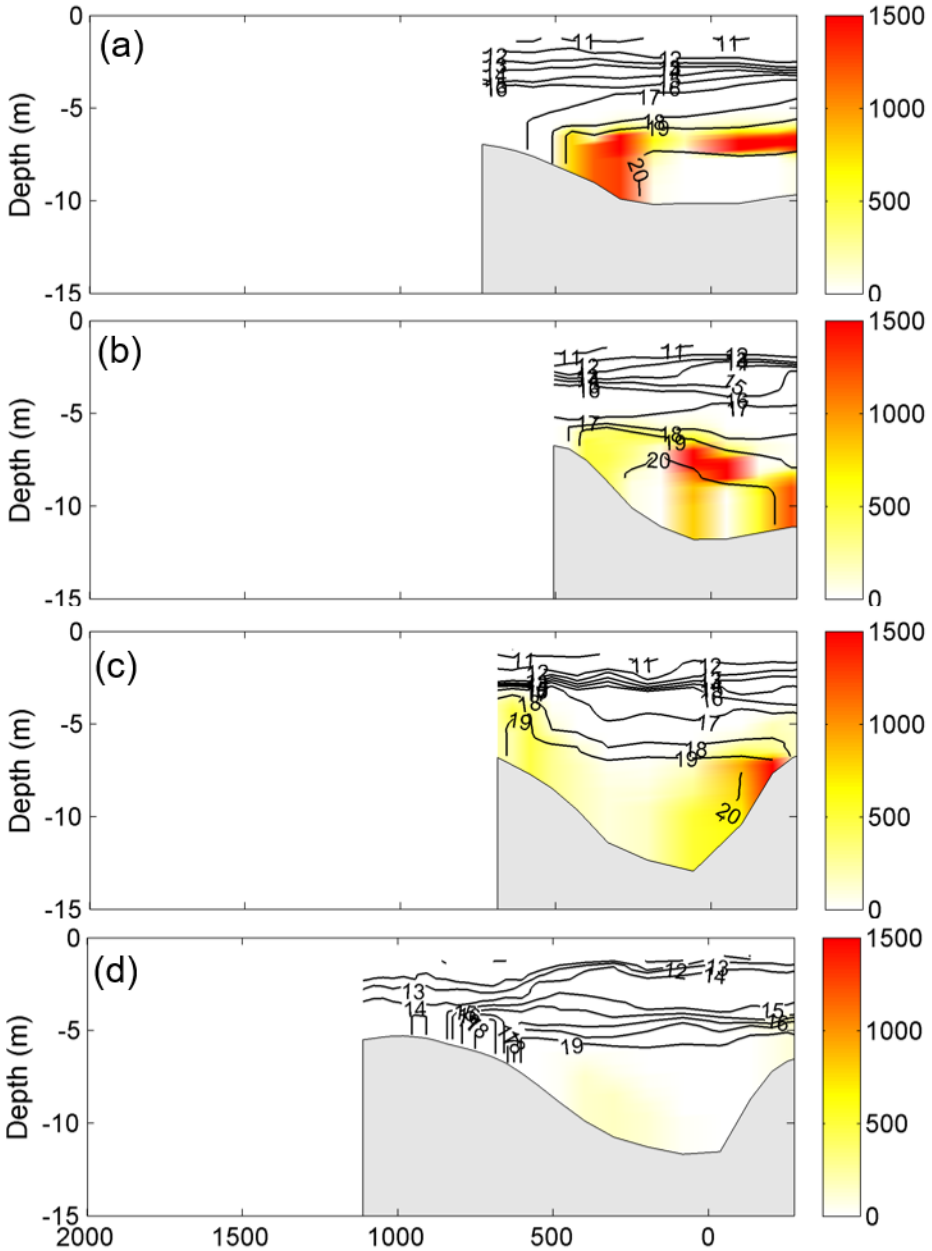

Figure A3. Cross channel distributions of dye concentration (color, 10^{-8} kg/m3) and salinity (contour, psu) at (a) 3.1, (b) 4.6, (c) 7.0 and (d) 8.5 hours after May 5 release. The transect locations are marked as dotted blue lines in plan-view figures.

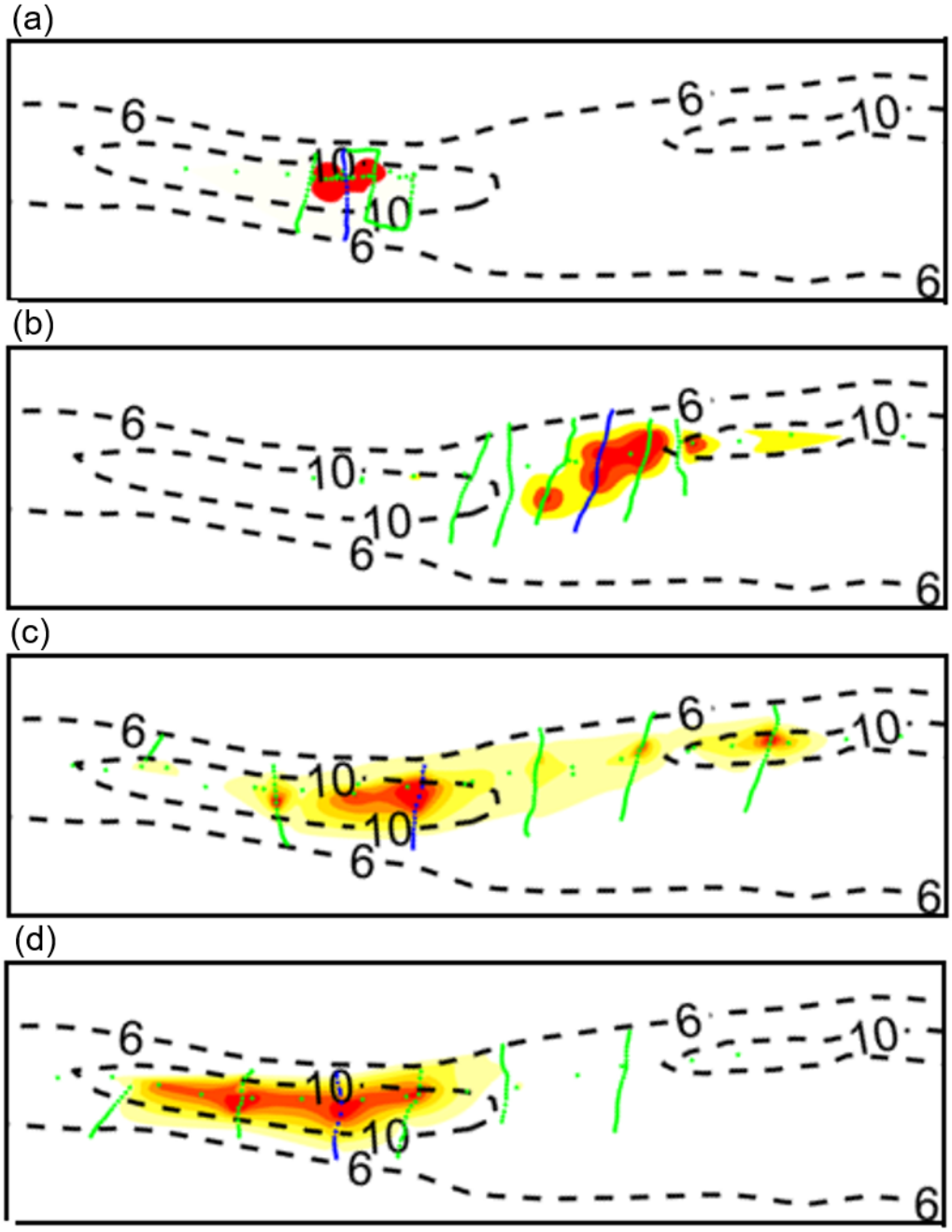

Figure A4. Plan view of the vertically integrated dye patch concentration (color) at (a) 2.78, (b) 5.15, (c) 8.11, (d) 9.65 hours after the dye release on May 7. The dashed lines show the bathymetry in meters. The dotted green and blue lines mark the cross-channel transects taken to sample the dye patch. The dotted blue lines mark the cross-channel transects plotted later.

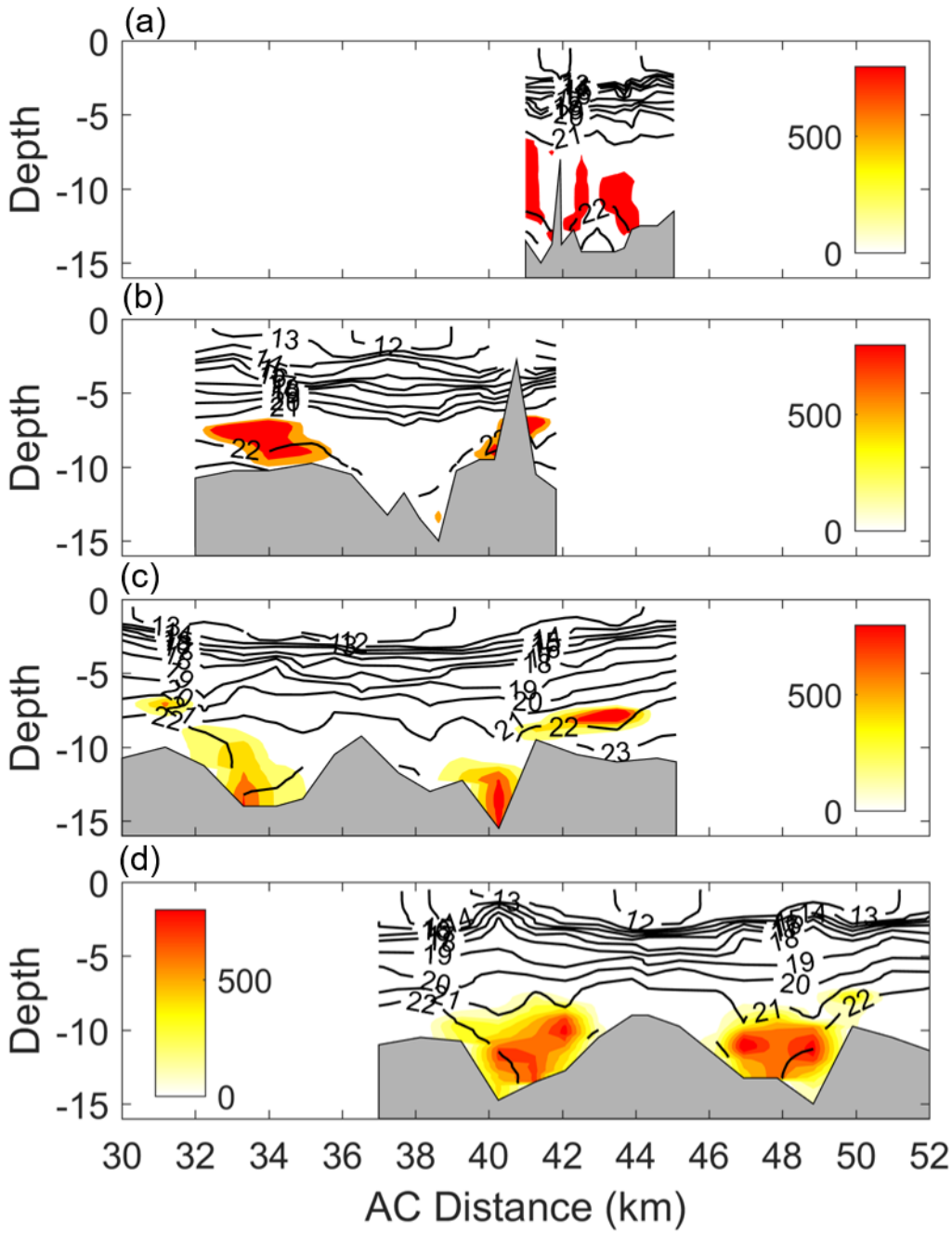

Figure A5. Along-channel distributions of dye concentration (color, 10^{-8} kg/m^3) and salinity (contour, psu) at (a) 2.8, (b) 5.2, (c) 8.1, (d) 9.7 hours after May 7 release. X-axis is the along-channel distance from estuarine mouth.

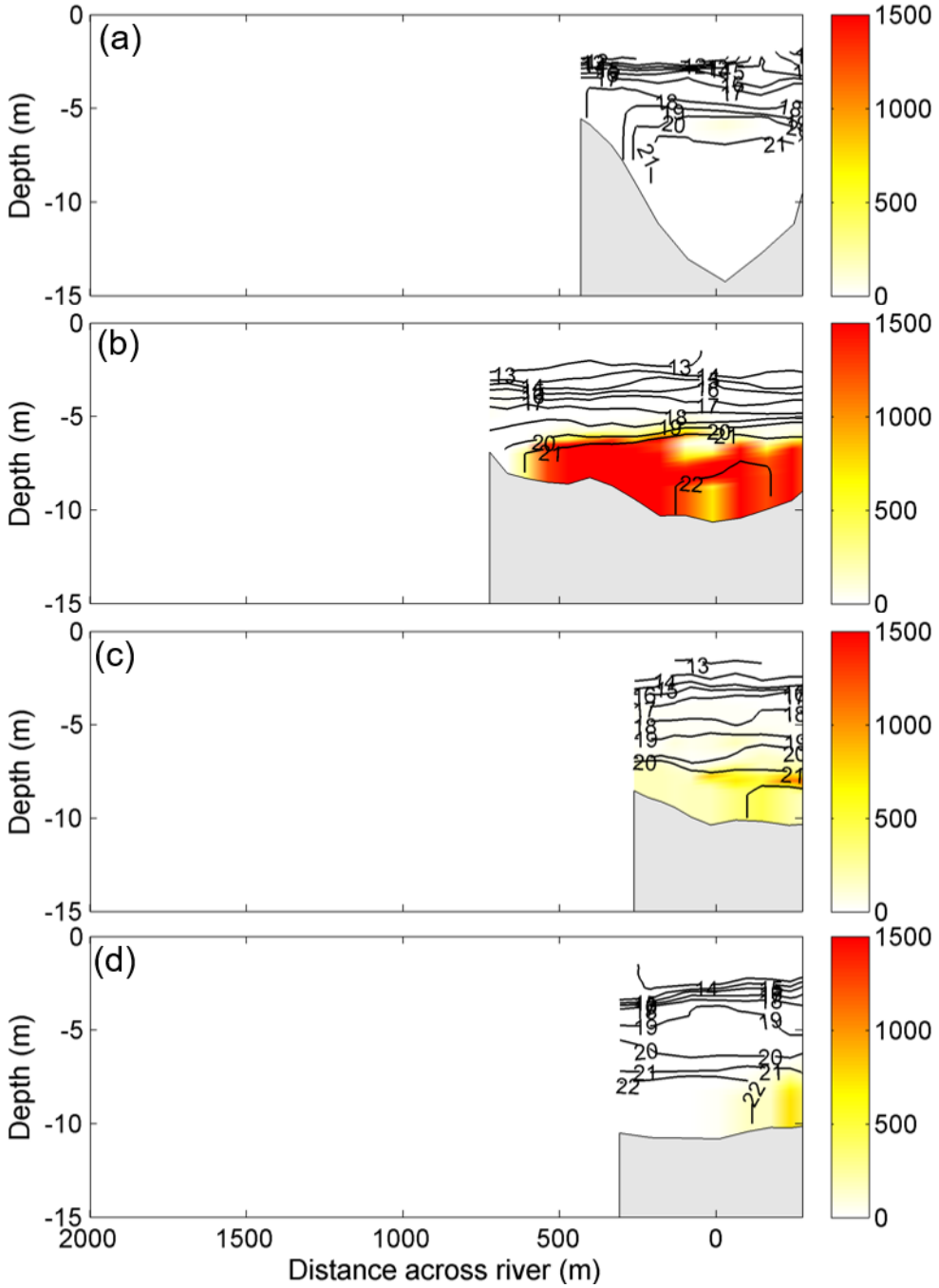

Figure A6. Cross channel distributions of dye concentration (color, 10^{-8} kg/m^3) and salinity (contour, psu) (a) 2.9, (b) 5.3, (c) 8.2, (d) 9.8 hours after May 7 release. The transect locations are marked as dotted blue lines in plan-view figures.

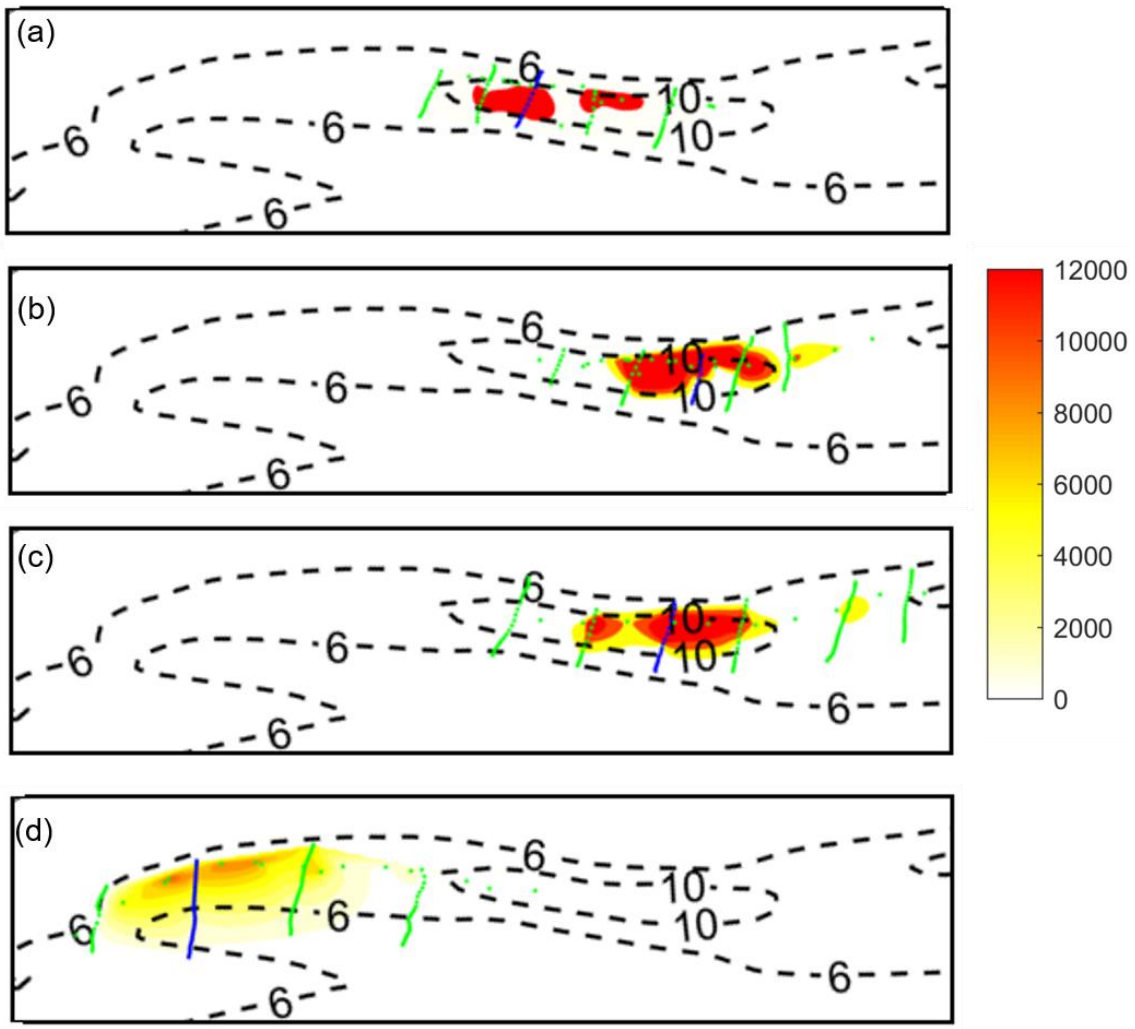

Figure A7. Plan view of the vertically integrated dye patch concentration (color) at (a) 2.8, (b) 4, (c) 6, (d) 9.6 hours after the dye release on May 25. The dashed lines show the bathymetry in meters; the dotted green and blue lines mark the cross-channel transects taken to sample the dye patch. The dotted blue lines mark the cross-channel transects plotted later.

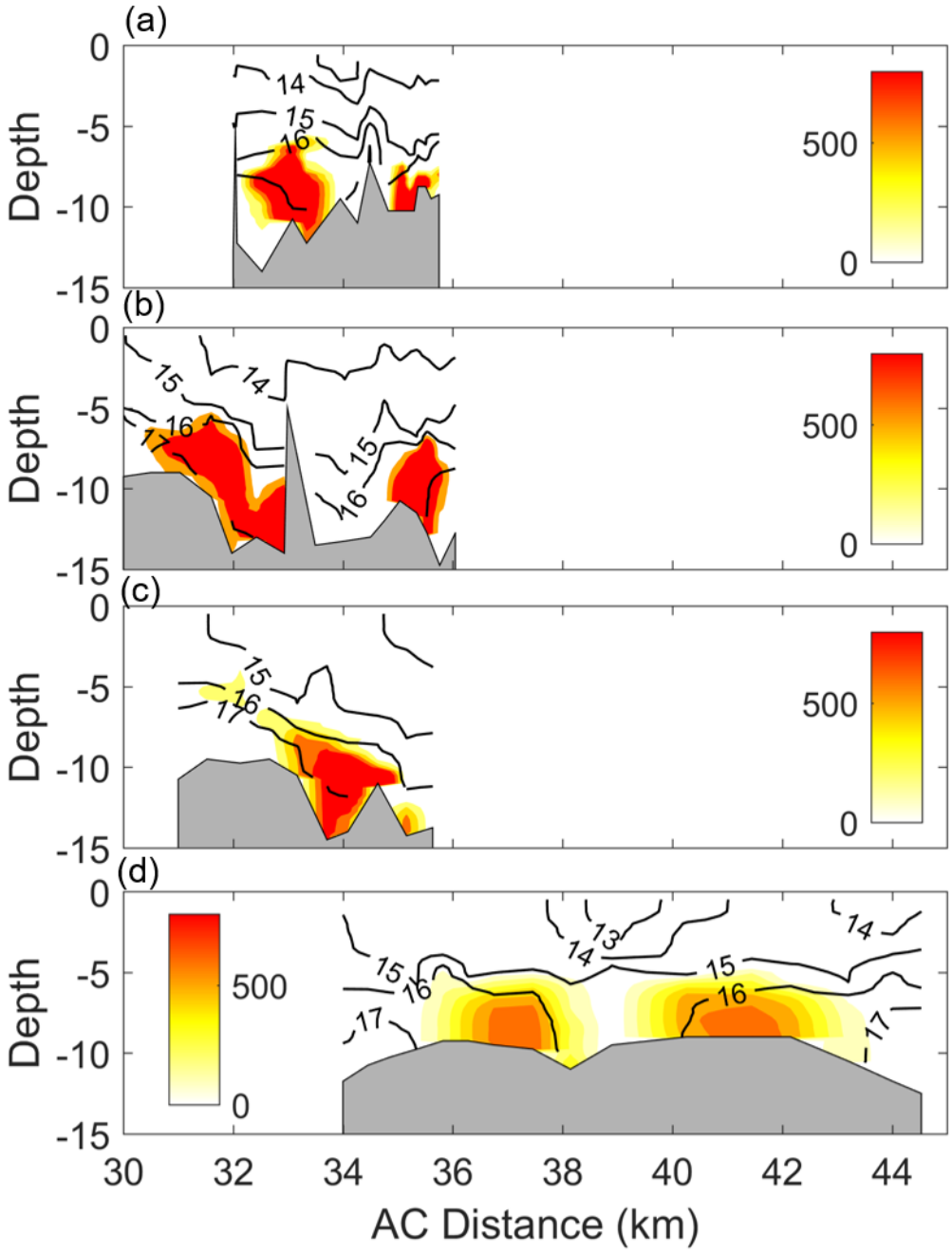

Figure A8. Along-channel distributions of dye concentration (color, 10^{-8} kg/m^3) and salinity (contour, psu) at (a) 2.83, (b) 3.95, (c) 6.05, (d) 9.61 hours after May 25 release. X-axis is the along-channel distance from estuarine mouth.

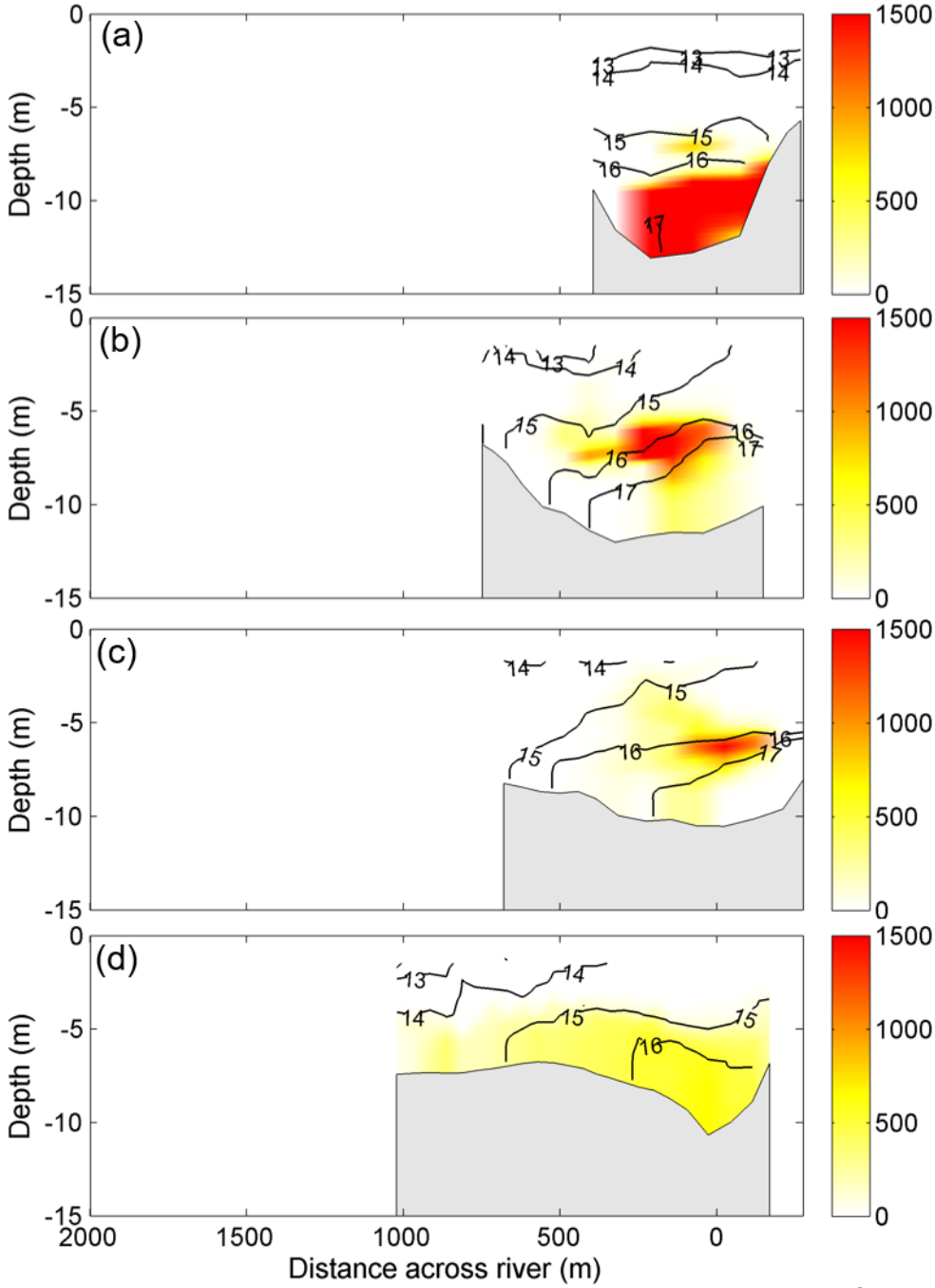

Figure A9. Cross channel distributions of dye concentration (color, 10^{-8} kg/m^3) and salinity (contour, psu) (a) 2.7, (b) 3.8, (c) 6, (d) 9.5 hours after May 25 release. The transect locations are marked as dotted blue lines in plan-view figures.

BIBLIOGRAPHY

Aristizabal, M. F., and R. J. Chant, 2014: Mechanisms driving stratification in Delaware Bay estuary. Ocean Dynamics, Volume 64, Number 11, Page 1615.

Aristizabal, M. F., and R. J. Chant, 2015: An observational study of salt fluxes in Delaware Bay, J. Geophys. Res. Oceans, 120, 2751–2768, doi:10.1002/2014JC010680.

Aristizabal, M. F., and R. J. Chant. 2013: A numerical study of salt fluxes in Delaware Bay estuary. J. Phys. Oceanogr. 43(8):1572–1588.

Batchelor, G.K., 1952: The effect of homogeneous turbulence on material lines and surfaces, Proc. Roy. Soc., A 213, 349-366.

Bowden, K. F., 1965: Horizontal mixing in the sea due to a shearing current, J. Fluid Mech., 21, 83– 95.

Bowden, K. F., 1965: Horizontal mixing in the sea due to a shearing current, J. Fluid Mech., 21, 83– 95.

Bowen, M. M., and W. R. Geyer, 2003: Salt transport and the time dependent salt balance of a partially stratified estuary, J. Geophys. Res., 108, 3158, doi:10.1029/2001JC001231.

Browne, D. R., and C. W. Fisher, 1988: Tide and tidal currents in the Chesapeake Bay, NOAA Technical Report NOS OMA 3, 84 pp.

Chatwin P. C., 1976: Some remarks on the maintenance of the salinity distribution in estuaries. Estuarine and Coastal Mar. Sci. 4:555-66.

Chatwin, P.C. and C.M. Allen, 1985b: Mathematical models of dispersion in rivers and estuaries. Ann. Rev. FluidMech. 17, 119-149.

Chen, C., Q. Xu, R. Houghton, & R. C. Beardsley, 2008: A model-dye comparison experiment in the tidal mixing front zone on the southern flank of Georges Bank. Journal of Geophysical Research: Oceans, 113(C2).

Chen, S.-N., W. R. Geyer, D. K. Ralston, and J. A. Lerczak, 2012: Estuarine exchange flow quantified with isohaline coordinates: Contrasting long and short estuaries, J. Phys. Oceanogr., 42,748–763, doi:10.1175/JPO-D-11-086.1.

Crain, C. M., B. R. Silliman, S. L. Bertness, and M. D. Bertness, 2004: Physical and biotic drivers of plant distribution across estuarine salinity gradients, Ecology, 85(9), 2539-2549.

Cruzado, A., Velásquez, Z., del Carmen Pérez, M., Bahamón, N., Grimaldo, N. S., & Ridolfi, F., 2002: Nutrient fluxes from the Ebro River and subsequent across-shelf dispersion. Continental Shelf Research, 22(2), 349-360.

Fischer H.B., 1976: Mixing and dispersion in estuaries. Annual Review of Fluid Mechanics 8, 107-33.

Fischer, H. B., 1972: Mass transport mechanisms in partially stratified estuaries, J. Fluid Mech., 53, 671– 687.

Fischer, H. B., E. J. List, R. C. Y. Kho, J. Imberger, and N. H. Brooks, 1979: Mixing in Inland and Coastal Waters, 483 pp., Elsevier, New York.

Fong, D. A., and M. T. Stacey, 2003: Horizontal dispersion of a near-bed coastal plume, J. Fluid Mech., 489, 239–267.

Fortier, L., and W. C. Leggett, 1982: Fickian transport and the dispersal of fish larvae in estuaries, Canadian Journal of Fisheries and Aquatic Sciences, 39(8), 1150-1163.

Garrett, C., 2006: Turbulent dispersion in the ocean, Progress in Oceanography, 70(2), 113-125.

Garvine RW, R. K. McCarthy, K. C. Wong, 1992: The axial salinity distribution in the Delaware estuary and its weak response to river discharge, Estuar Coast Shelf Sci 35:157–165.

Geyer, W. R. and R. P. Signell, 1992: A reassessment of the role of tidal dispersion in estuaries and bays, Estuaries, 15: 97-108. 10.

Geyer, W. R., R. Chant, and R. Houghton, 2008: Tidal and spring-neap variations in horizontal dispersion in a partially mixed estuary, J. Geophys. Res., 113, C07023, doi:10.1029/2007JC004644.

Goldberg, E. D., Hodge, V., Koide, M., Griffin, J., Gamble, E., Bricker, O. P. & Braun, R., 1978: A pollution history of Chesapeake Bay, Geochimica et Cosmochimica Acta, 42(9), 1413-1425.

Hansen, D. V., and M. Rattray, 1965: Gravitational circulation in straits and estuaries. J. Mar. Res., 23, 104–122.

Holleman, R.C. and M.T. Stacey, 2013: Transient dispersion regimes, Journal of Fluid Mechanics, 736, 130–149.

Huang, H., Chen, C., Cowles, G., Winant, C.D., Beardsley, R.C., Hedstrom, K.S., Haidvogel, D.B., 2008: FVCOM validation experiments: comparisons with ROMS for three idealized barotropic test problems. J. Geophys. Res. 113, C07042. doi:10.1029/ 2007JC004557.

IPCC, 2013: Summary for Policymakers. In: Climate Change 2013: The Physical Science Basis. Contribution of Working Group I to the Fifth Assessment Report of the

Intergovernmental Panel on Climate Change, Stocker, T.F., D. Qin, G-K. Plattner, M. Tignor, S.K. Allen, J. Boschung, A. Nauels, Y. Xia, V. Bex and P.M. Midgley (eds.), Kennedy, V.S., Breitburg, D.L., Christman, M.C., Luckenbach, M.W., Paynter, K., Kramer, J., Sellner, K.G., Dew-Baxter, J., Keller, C., Mann, R, (2011: Lessons Learned From Efforts To Restore Oyster Populations In Maryland And Virginia, 1990 To 2007, Journal Of Shellfish Research 30(3), 719-731.

Jay, D. A., and J. D. Smith, 1990: Circulation, density distribution and neap-spring transitions in the Columbia River Estuary, Prog. Oceanogr., 28, 81– 112.

Jia, P., and M. Li, 2012: Circulation dynamics and salt balance in a lagoonal estuary, J. Geophys. Res., 117, C01003, doi:10.1029/2011JC007124.

Jones, N. L., R. J. Lowe, G. Pawlak, D. A. Fong, and S. G. Monismith, 2008: Plume dispersion on a fringing coral reef system. Limnol.Oceanogr., 53, 2273–2286.

Kadirvelu, K., K. Thamaraiselvi, and C. Namasivayam, 2001: Removal of heavy metals from industrial wastewaters by adsorption onto activated carbon prepared from an agricultural solid waste. Bioresource technology, 76(1), 63-65.

Kundzewicz, Z. W., Mata, L. J., Arnell, N. W., Doll, P., Kabat, P., Jimenez, B., and Shiklomanov, I., 2007: Freshwater resources and their management.

Ledwell, J. R., Watson, A. J., & Law, C. S., 1998: Mixing of a tracer in the pycnocline, Journal of Geophysical Research: Oceans, 103(C10), 21499-21529.

Lerczak, J. A., W. R. Geyer, and R. J. Chant, 2006: Mechanisms driving the time-dependent salt flux in a partially stratified estuary, J. Phys. Oceanogr., 36, 2296–2311, doi:10.1175/JPO2959.1.

Levin, L. A., 2006: Recent progress in understanding larval dispersal: new directions and digressions, Integrative and comparative biology, 46(3), 282-297.

Li M., W. Liu, R. Chant and A. Velle-Levinson, 2017: Flood-Ebb and Spring-Neap Variations of Lateral Circulation in the James River Estuary, Continental Shelf Research (under revision).

Li, M., and L. Zhong, 2009: Flood–ebb and spring–neap variations of mixing, stratification and circulation in Chesapeake Bay, Continental Shelf Research, 29(1), 4-14.

Li, M., L. Zhong, and W. C. Boicourt, 2005: Simulations of Chesapeake Bay estuary: Sensitivity to turbulence mixing parameterizations and comparison with observations, J. Geophys. Res.-Oceans 110(C12 AR C12004).

Li, Y. and M. Li, 2012: Wind-driven lateral circulation in a stratified estuary and its effects on the along-channel flow, J Geophys Res 117(C9):C09005.

MacCready, P., 2004: Toward a unified theory of tidally-averaged estuarine salinity structure. Estuaries, 27, 561–570, doi:10.1007/BF02907644.

MacCready, P., 2007: Estuarine adjustment, J. Phys. Oceanogr., 37, 2133–2144, doi:10.1175/JPO3082.1.

MacCready, P., 2011: Calculating estuarine exchange flow using isohaline coordinates, J. Phys. Oceanogr., 41, 1116–1124, doi:10.1175/2011JPO4517.1.

MacCready, P., and W. R.Geyer, 2010: Advances in estuarine physics, Annu. Rev. Mar. Sci., 2, 35–58, doi:10.1146/annurev-marine-120308-081015.

Mann, R., and Evans, D.A., 2004: Site selection for oyster habitat rehabilitation in the Virginia portion of the Chesapeake Bay: a commentary. Journal of Shellfish Research 23:41-49.

Marchesiello, P., J. C. McWilliams, and A. Shchepetkin, 2001: Open boundary conditions for long-term integration of regional oceanic models, Ocean Modell., 3, 1–20.

Martino, E. J., and K. W. Able, 2003: Fish assemblages across the marine to low salinity transition zone of a temperate estuary. Estuarine, Coastal and Shelf Science, 56(5), 969-987.

Meehl, G. A., C. Tebaldi, H. Teng, and T. C. Peterson, 2007: Current and future US weather extremes and El Niño. Geophysical Research Letters, 34(20).

Moniz, R. J., D. A. Fong, C. B. Woodson, S. K. Willis, M. T. Stacey, and S. G. Monismith, 2014: Scale-dependent dispersion within the stratified interior on the shelf of northern Monterey Bay, J. Phys. Oceanogr., 44, 1049–1064, doi:10.1175/JPO-D-12-0229.1.

Okubo A., 1971: Oceanic diffusion diagrams, Deep-Sea Res., 18, 789–802.

Okubo, A., 1973: Effects of shoreline irregularities on streamwise dispersion in estuaries and other embayments, Neth. J. Sea Res., 8, 213– 224.

Pierce, S. K., L. M. Rowland-Faux, and S. M. O'Brien, 1992: Different salinity tolerance mechanisms in Atlantic and Chesapeake Bay conspecific oysters: glycine betaine and amino acid pool variations, Marine Biology, 113(1), 107-115.

Pritchard, D. W., 1952: Estuarine hydrography, Adv. Geo- phys., 1, 243–280.

Pritchard, D. W., 1954: A study of the salt balance in a coastal plain estuary, J. Mar. Res., 13, 133–144.

Pritchard, D. W., 1956: The dynamic structure of a coastal plain estuary, J. Mar. Res., 15, 33–42.

Richardson, L.F., 1926: Atmospheric diffusion shown on a distance-neighbour graph, Proc. Roy. Soc. Lond., A 100, 709–737.

Riddle, A. M. & Lewis, R. E., 2000: Dispersion experiments in U.K. coastal water. Estuarine, Coastal and Shelf Science 51, 243–254.

Roman, M.R. and W.C. Boicourt, 1999: Dispersion and recruitment of crab larvae in the Chesapeake Bay plume: physical and biological controls, Estuaries 22: 563. doi:10.2307/1353044

Ross, A. C., R. G. Najjar, M. Li, S. B. Lee, F. Zhang and W. Liu, 2017: Fingerprints of sea-level rise on changing tides in the Chesapeake and Delaware Bays, Submitted to JGR-Oceans.

Shen, J., J. D. Boon, & A. Y. Kuo, 1999: A modeling study of a tidal intrusion front and its impact on larval dispersion in the James River estuary, Virginia. Estuaries and Coasts, 22(3), 681-692.

Simpson, J. H., J. Brown, J. Matthews, and G. Allen, 1990: Tidal straining, density currents, and stirring in the control of Estuarine stratification, Estuaries, 13, 125–132.

Smart, P. L., and I. M. S. Laidlaw, 1977: An evaluation of some fluorescent dyes for water tracing, Water Resour. Res., 13, 15– 33.

Smith, R., 1977: Long-term dispersion of contaminants in small estuaries, J. Fluid Mech., 82, 129–146.

Stacey, M. T., E. A. Cowen, T. M. Powell, E. Dobbins, S. G. Monismith, and J. R. Koseff, 2000: Plume dispersion in a stratified, near-coastal flow: Measurements and modeling, Cont. Shelf Res., 20, 637–663.

Stommel, H. M., and H. G. Former, 1952: On the nature of estuarine circulation. Part I, Woods Hole Oceanographic Institution Ref. 52–88, 172 pp.

Sumer, S. M., and H. B. Fischer, 1977: Transverse mixing in partially stratified flow, J. Hydraul. Eng., ASCE, 103, 587– 600.

Sutherland, D., P. MacCready, N. Banas, and L. Smedstad, 2011: A model study of the Salish Sea estuarine circulation, J. Phys. Oceanogr., 41, 1125–1143, doi:10.1175/2011JPO4540.1.

Taylor, G. I., 1953: Dispersion of soluble matter in solvent flowing slowly through a tube, Proc. R. Soc. Lond. A 219, 186.

Taylor, G. I., 1954: The dispersion of matter in turbulent flow through a pipe, J. Phys. A, J. Phys. B, J. Phys. C, 223, 446– 468.

Taylor, G.I., 1921: Diffusion by continuous movements, Proc. London Math. Soc., 20, 196-212.

Valle-Levinson, A., C. Li, K. Wong, and K.M.M. Lwiza, 2000b: Convergence of Lateral Flow Along a Coastal Plain Estuary, J. Geophys. Res., 105(C7), 17,045-17,061.

Valle-Levinson, A., K. Wong, and K. Bosley, 2001: Observations of the wind-induced exchange at the entrance to Chesapeake Bay, J. Mar. Res., 59(3), 391-416, 2001.

Valle-Levinson, A., K.C. Wong, and K.M.M. Lwiza, 2000a: Fortnightly variability in the transverse dynamics of a coastal plain estuary, J. Geophys. Res, 105(C2), 3413-3424.

Vasholz, D. P., and L. J. Crawford, 1985: Dye dispersion in the seasonal thermocline, J. Phys. Oceanogr., 15, 695–712.

Wang, T., W. Geyer, P. Engel, W. Jiang, and S. Feng, 2015: Mechanisms of tidal oscillatory salt transport in a partially stratified estuary. J. Phys. Oceanogr. doi:10.1175/JPO-D-15-0031.1.

Warner, J. C., C. R. Sherwood, H. G. Arango, and R. P. Signell, 2005b: Performance of four turbulence closure models implemented using a generic length scale method, Ocean Modelling, 8(1), 81-113.

Warner, J. C., C. R. Sherwood, H. G. Arango, and R. P. Signell, 2005b: Performance of four turbulence closure models implemented using a generic length scale method, Ocean Modelling, 8(1), 81-113.

Warner, J. C., W. R. Geyer, and J. A. Lerczak, 2005a: Numerical modeling of an estuary: A comprehensive skill assessment, J. Geophys. Res., 110, C05001, doi:10.1029/2004JC002691.

Wilson, R. E., and A. Okubo, 1978: Longitudinal dispersion in a partially mixed estuary, J. Mar. Res., 36(3), 427 – 447.

Wood, L. H., and W. J. Hargis, 1971: Transport of bivalve larvae in a tidal estuary (pp. 29-44), Cambridge University Press.

Young, W. R., and P. B. Rhines, 1982: Shear-flow dispersion, internal waves and horizontal mixing in the ocean, J. Phys. Oceanogr., 12, 515– 527.

Young, W. R., and S. Jones, 1991: Shear dispersion, Phys. Fluids A, 3, 1087.

Zhong, L. and M. Li, 2006: Tidal energy fluxes and dissipation in the Chesapeake Bay, Continental Shelf Research, 26, 752-770.

Zimmerman, J. T. F., 1979: On the Euler-Lagrange transformation and the Stokes' drift in the presence of oscillatory and residual currents, Deep-Sea Res., 26A, 505–520, doi:10.1016/0198-0149(79)90093-1.